

**Study on synthesis of  
carbon-nanomaterials  
in high-density media plasma processes**

**ANDO Atsushi**

**Study on synthesis of  
carbon-nanomaterials  
in high-density media plasma processes**

**ANDO Atsushi**

2018

Nagoya University

Department of Electrical Engineering and Computer Science

# Contents

## Chapter 1 Introduction

1.1 Carbon nanotubes (CNTs) .....	1
1.1.1 Structure of single-walled carbon nanotubes (SWNTs) .....	2
1.1.2 Electric state of SWNTs .....	8
1.2 Graphene .....	14
1.3 Synthesis techniques for carbon nanomaterials .....	15
1.3.1 Laser vaporization .....	15
1.3.2 Chemical vapor deposition (CVD) .....	17
1.3.3 Arc plasma vaporization .....	19
1.3.4 In-liquid plasma employing alcohol .....	22
1.4 Previous studies .....	25
1.4.1 Arc plasma for SWNTs synthesis .....	25
1.4.2 In-liquid plasma for graphene synthesis .....	26
1.5 Purpose and composition of this thesis .....	27
References .....	31

## Chapter 2. Measurement techniques of plasmas and evaluation methods of synthesized carbon nanomaterials and by-products

2.1 Experimental methods .....	44
2.1.1 Arc plasma for SWNTs synthesis .....	44
2.1.2 Characteristics of arc plasma for SWNTs synthesis .....	46
2.1.3 In-liquid plasma for nanographene synthesis .....	50
2.2 Optical emission spectroscopy (OES) .....	54
2.3 Raman scattering spectroscopy of carbon nanomaterials .....	59
2.4 Gas chromatography-mass spectrometry (GC-MS) .....	63
References .....	65

### **Chapter 3. Optical diagnostics and the synthesis mechanism on arc-plasma-synthesized SWNTs in the arc plasma**

3.1 Backgrounds of the SWNTs synthesis in arc plasma.....	67
3.2 Experimental setup .....	67
3.2.1 Arc plasma synthesis of SWNTs .....	67
3.2.2 Optical measurements of the arc plasma .....	70
3.2.3 Crystallographic analyses of the synthesized SWNTs .....	70
3.3 Experimental results and discussion.....	71
3.3.1 Dependence of the arc current on synthesized SWNTs crystallinity.....	71
3.3.2 Dependence of the He pressure on synthesized SWNTs crystallinity .....	77
3.3.3 Optical diagnostics of the arc plasma during SWNTs synthesis.....	80
3.3.4 Discussion: a relationship between SWNTs growth and optical emission intensities from species in arc plasmas .....	87
3.4 Conclusion of chapter 3 .....	90
References.....	93

### **Chapter 4. Nanographene synthesized by the in-liquid plasma employing various kinds of alcohols**

4.1 Backgrounds of this study .....	95
4.2 Experimental setup .....	95
4.2.1 Synthesis method of nanographene in the in-liquid plasma.....	95
4.2.2 Optical measurements.....	98
4.2.3 Crystallographic measurements.....	98
4.3 Results and discussion.....	98
4.3.1 Synthesis rates of nanographene.....	98
4.3.2 Dependence of types of alcohols on nanographene crystallinity .....	101
4.3.3 Optical diagnostics of the in-liquid plasma .....	105
4.3.4 Chemical components in the residual liquids .....	109
4.3.5 Discussion: Nanographene synthesis in the in-liquid plasma.....	112
4.4 Conclusion of chapter 4 .....	115
References.....	117

## **Chapter 5. Effects of carbon-sources on nanographene synthesis: A comparison between hydrocarbons and alcohols**

5.1 Backgrounds of this study .....	119
5.2 Experimental setup .....	119
5.2.1 In-liquid plasma synthesis of nanographene .....	119
5.2.2 Analysis of the synthesized nanographene .....	121
5.3 Results and discussion.....	121
5.3.1 Crystallographic analysis of nanographene synthesized by the in-liquid plasma.....	121
5.3.2 Optical diagnostics of the in-liquid plasma .....	126
5.3.3 Intermediates and by-products in the residual liquids after filtration of solid materials .....	130
5.3.4 Discussion: Nanographene synthesis reactions taken into accounts of alcohols and hydrocarbons employment results .....	134
5.4 Conclusion of chapter 5 .....	135
References.....	137

## **Chapter 6. Control of nanographene crystallinity in the in-liquid plasma processes using methanol mixture with the other alcohols**

6.1 Backgrounds of this study .....	139
6.2 Experimental setup .....	139
6.3 Results and discussion.....	142
6.3.1 Crystallographic analysis .....	142
6.3.2 Measurement of the in-liquid plasma employing mixture liquid.....	148
6.3.3 By-products and intermediates analysis in the filtered liquids.....	152
6.3.4 Discussion: Oxygen species effects .....	154
6.4 Conclusion of chapter 6 .....	158
References.....	160

## **Chapter 7. Conclusions and future works**

7.1 Summary of this thesis .....	161
7.2 Scopes for future works .....	164
<b>Acknowledgements</b> .....	167
<b>List of papers related to this thesis</b> .....	170

## Chapter 1. Introduction

### 1.1 Carbon nanotubes (CNTs)

Carbon nanomaterials such as carbon nanotubes (CNTs) [1], graphenes [2], fullerenes [3], and so on, have attracted great attentions due to their excellent properties. High performances of various kinds of the carbon nanomaterials are expected to replace existing materials. In 1991, Iijima found multi-walled carbon nanotubes (MWNTs) from cathode deposits during fullerene synthesis by the arc plasma [1]. 2 years later, single atomic layered shell carbon nanotubes, i.e., single-walled carbon nanotubes (SWNTs) were successfully synthesized using catalytic metals contained carbon rod evaporation [4,5].

MWNTs and SWNTs have unique and excellent properties about several points. CNTs are formed from rolled graphene sheets and end cap with a five-membered ring contained the half-sphere. MWNTs have 2 up to 50 layers nesting tubular carbon atomic layers structures. This unique structural nanomaterial has strong kinetic properties. Young's modulus of individual MWNTs was estimated  $\sim 4$  TPa [6] which did not depend on the diameter of MWNTs. Tensile breaking strength of MWNTs was reported  $\sim 63$  GPa [7]. In addition, MWNTs also have high thermal property. Thermal conductivity had been reported  $\sim 830 \text{ Wm}^{-1}\text{K}^{-1}$  [8,9]. Current carrying capacity is  $\sim 10^{10} \text{ Acm}^{-2}$  [10]. SWNTs also have excellent properties. Young's modulus of SWNTs indicates  $\sim 1$  TPa [11]. Tensile breaking strength is  $\sim 22$  GPa [12]. Thermal conductivity is  $\sim 3300 \text{ Wm}^{-1}\text{K}^{-1}$  [13,14]. Electron mobility reaches  $100\,000 \text{ cm}^2\text{V}^{-1}\text{s}^{-1}$  [15]. In addition, SWNTs indicate metal or semiconducting properties by winding direction of graphene sheet i.e. chirality [16]. From these properties, CNTs are expected to apply to composite materials [17-20],

transistor [21-23], trace of large-scale integration [24,25], electron field emission sources [26], battery electrodes [27-29] and so on.

### 1.1.1 Structure of single-walled carbon nanotubes (SWNTs)

SWNTs have unique properties originated in their structures which are formed from single carbon atomic layer. SWNTs are tubes which have nanometer-order diameter winded a graphene sheet. This winding determines properties of SWNTs. Most of important factors on SWNTs are decided by chirality and diameter of SWNTs. Chirality means the helical structural degree and it depends on the position cut and the connected graphene sheet. Chirality and diameter of SWNTs were unambiguously determined by the chiral vector (denoted  $\mathbf{C}_h$ ) [16,30,31]. The chiral vector circulates the cylindrical axis vertically, i.e. circumferential direction of SWNTs. This vector connects an equivalent point O and A which are overlapped when the graphene sheet is winded as shown in Fig. 1.1 [16]. The chiral vector is given by the following equation using the primitive translation vector of two dimensional hexagonal grids,

$$\mathbf{C}_h = n\mathbf{a}_1 + m\mathbf{a}_2 \equiv (n, m), \quad (1.1)$$

$n$  and  $m$  are integer ( $n \geq m$ ). The length of the chiral vector is the circumferential length of SWNTs.

$$C_h = \sqrt{3}a_{C-C} \sqrt{n^2 + nm + m^2}. \quad (1.2)$$

$a_{C-C}$  is the distance of closest approach on the carbon-carbon bond (0.144 nm). The diameter  $d_t$  and chiral angle  $\theta$  of SWNTs are calculated from the following equation.

$$d_t = \frac{\sqrt{3}a_{C-C}}{\pi} \sqrt{n^2 + nm + m^2}. \quad (1.3)$$

$$\theta = \tan^{-1}\left(\frac{\sqrt{3}m}{2n+m}\right) \quad \left(|\theta| \leq \frac{\pi}{6}\right). \quad (1.4)$$

In the case of  $n = m$  ( $\theta = \pi/6$ ), the helical structure is not formed and when it becomes the armchair type as shown in Fig. 1.2(a) or when  $m = 0$  ( $\theta = 0$ ), it takes the zigzag type structure as shown in Fig. 1.2(b) Other types take the helical structure, i.e. the chiral type as shown in Fig. 1.2(c)  $\mathbf{T}$  is primitive translational vector in the axial direction of tube.  $\mathbf{T}$  is given by the following equation.

$$\mathbf{T} = \frac{\{(2m+n)\mathbf{a}_1 - (2n+m)\mathbf{a}_2\}}{d_R}, \quad t_1 = \frac{2m+n}{d_R}, \quad t_2 = \frac{2n+m}{d_R}. \quad (1.5)$$

$\mathbf{a}_1$  and  $\mathbf{a}_2$  are primitive lattice vectors as shown in Fig. 1.3 [32].

$$\mathbf{a}_1 = \left(\frac{\sqrt{3}}{2}, \frac{1}{2}\right)\sqrt{3}a_{C-C}, \quad \mathbf{a}_2 = \left(\frac{\sqrt{3}}{2}, -\frac{1}{2}\right)\sqrt{3}a_{C-C}. \quad (1.6)$$

Reciprocal lattice vectors are following.

$$\mathbf{b}_1 = \left(\frac{1}{\sqrt{3}}, 1\right)\frac{2\pi}{\sqrt{3}a_{C-C}}, \quad \mathbf{b}_2 = \left(\frac{1}{\sqrt{3}}, -1\right)\frac{2\pi}{\sqrt{3}a_{C-C}}. \quad (1.7)$$

The length of  $\mathbf{T}$  is given by following using the length of chiral vector  $l$ .

$$|\mathbf{T}| = \frac{\sqrt{3}l}{d_R}. \quad (1.6)$$

$$l = |\mathbf{C}_h| = \sqrt{3}a_{C-C}\sqrt{n^2 + nm + m^2}. \quad (1.7)$$

$d_R$  is integer defined by following equation using the greatest common divisor of  $n$  and  $m$ .

$$d_R \begin{cases} d, & \text{if}(n-m) \text{ is not multiple of } 3d \\ 3d, & \text{if}(n-m) \text{ is multiple of } 3d \end{cases}. \quad (1.8)$$

The part surrounded by  $\mathbf{C}_h$  and  $\mathbf{T}$  is unit cell of SWNTs. The number of carbon hexagons included in unit cell  $N_u$  is given by following equation.

$$N_u = \frac{|\mathbf{C}_h \times \mathbf{T}|}{|\mathbf{a}_1 \times \mathbf{a}_2|}. \quad (1.9)$$

Chiral angle  $\theta$  between  $\mathbf{C}_h$  and  $\mathbf{a}_1$  is given by following equation.

$$\theta = \arccos\left(\frac{\mathbf{C}_h \cdot \mathbf{a}_1}{|\mathbf{C}_h| |\mathbf{a}_1|}\right) = \arccos\left(\frac{2n+m}{2\sqrt{n^2+nm+m^2}}\right). \quad (1.10)$$

$\theta$  has range at  $0^\circ \leq \theta \leq 30^\circ$ . Reciprocal lattice vectors  $\mathbf{K}_1$  (circumferential direction),  $\mathbf{K}_2$  (tube axis direction) are given by following equation.

$$\mathbf{K}_1 = \frac{1}{N_u}(-t_2 \mathbf{b}_1 + t_1 \mathbf{b}_2), \quad \mathbf{K}_2 = \frac{1}{N_u}(m \mathbf{b}_1 - n \mathbf{b}_2). \quad (1.11)$$

$\mathbf{K}_1$  returns to the initial state when  $\mathbf{K}_1$  is multiplied by  $N_u$ . Wave number vector  $\mathbf{K}$  is described by following equation.

$$\mathbf{K} = \mu \mathbf{K}_1 + k \mathbf{K}_2 \quad (1 - N_u/2 \leq \mu \leq N_u/2, -1/2 \leq k \leq 1/2). \quad (1.12)$$

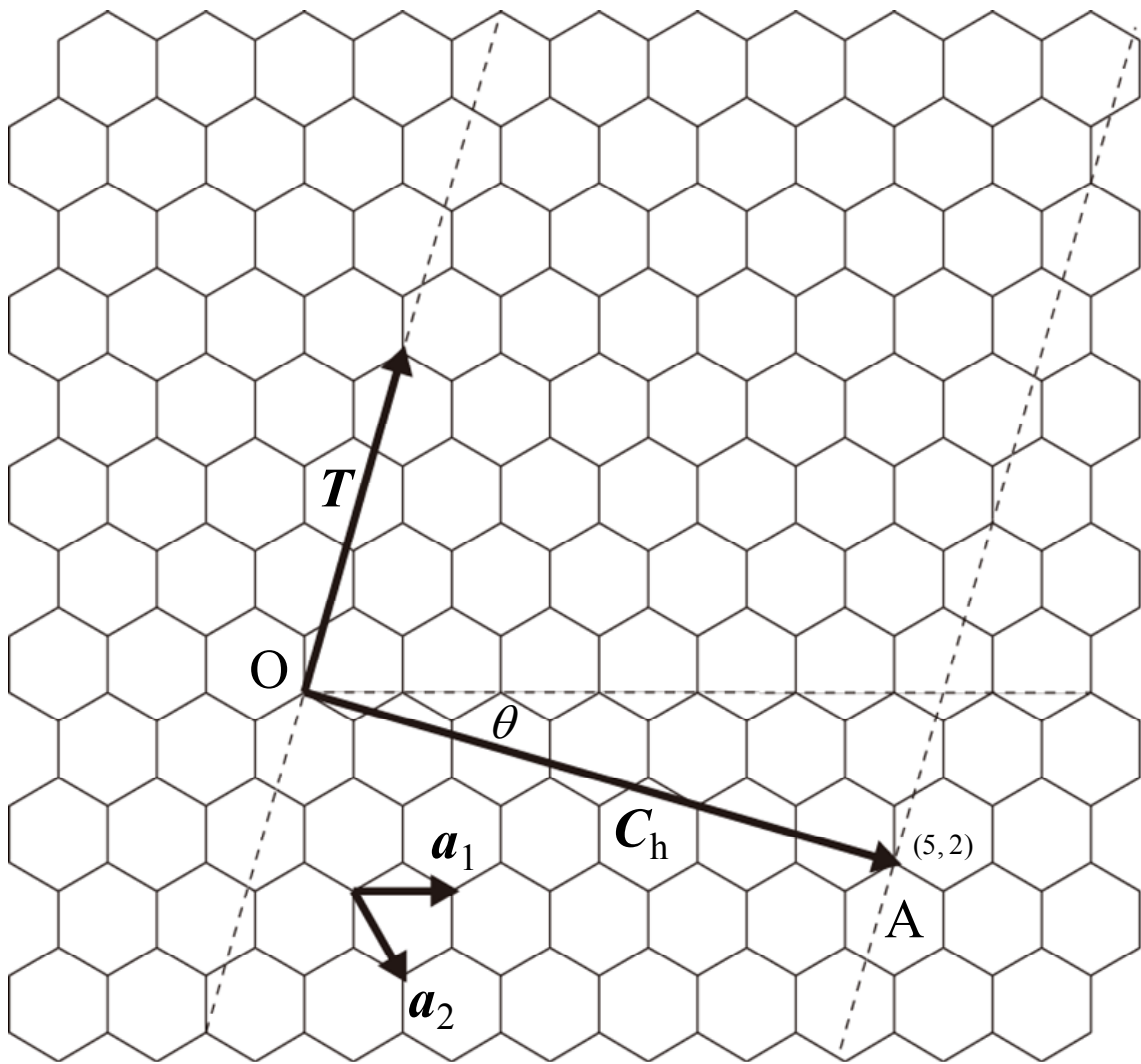
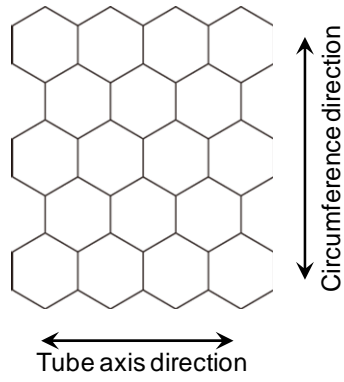
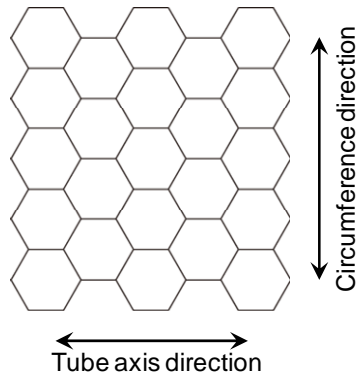


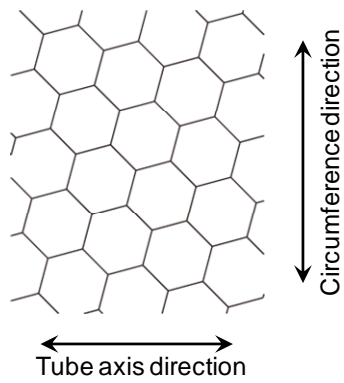
Figure 1.1. Geometry of CNTs [16].



(a) Armchair.

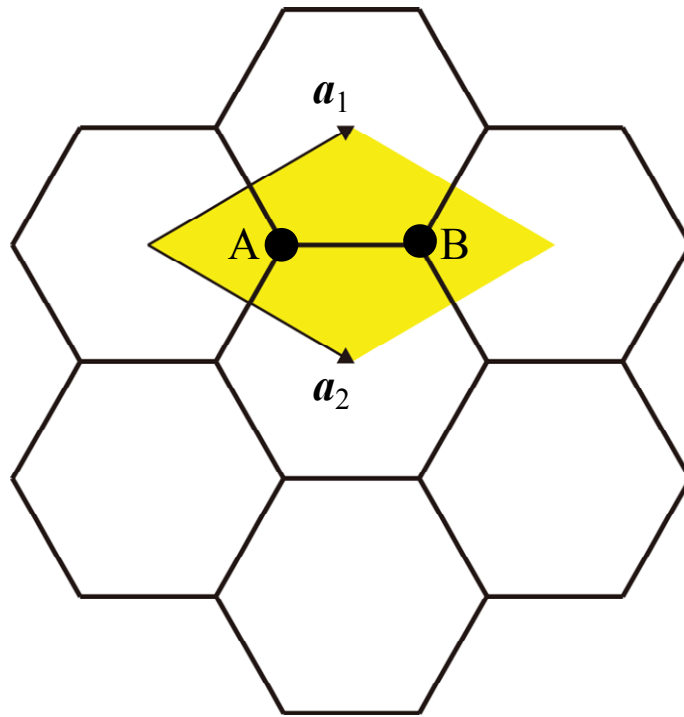


(b) Zigzag.

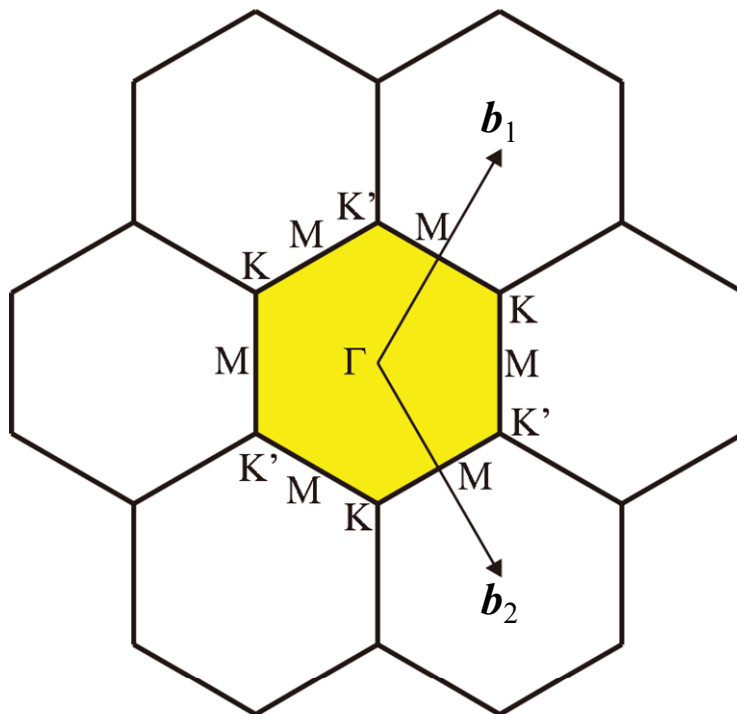


(c) Chiral.

Figure 1.2. The pattern of CNTs wall lattice direction.



(a) Real lattice (A and B are carbon atoms included unit cell).



(b) Reciprocal lattice

Figure 1.3. Primitive lattice of graphene sheet [32].

### 1.1.2 Electronic state of SWNTs

Carbon atom has 4 valence electrons whose electronic structure is  $(2s)^2(2p)^2$ . Carbon with  $sp^2$  hybrid orbital forms six-membered ring structure, 3 valence electrons occupy  $\sigma$  orbital, and the remaining 1 electron dominates electric properties as  $\pi$  electron. In the case of graphene, as shown in Fig. 1.4 [36], it becomes the zero-gap semiconductor due to no energy gap between the energy band on coupled band and the anti-coupled band [32]. In the case of SWNTs with winded graphene structure, the new periodic boundary condition appears in the circumferential direction of the tube, SWNTs become semiconductor with band gap at Fermi surface or metal with finite density of state. In the plane perpendicular to the tube axis, wave number  $\mathbf{k}$  is quantized by the periodic boundary condition specified by the chiral vector  $\mathbf{C}_h$  of the Eq. (1.1).

$$\mathbf{C}_h \cdot \mathbf{k} = 2\pi q \quad (q \text{ is integer}). \quad (1.13)$$

In the axial direction of the tube, it becomes one-dimensional material with translation symmetry represented by a lattice vector  $\mathbf{T}$ . Therefore, SWNTs indicate electronic structure in which electronic structure of graphene is modulated by these periodicities. In addition, coupled  $\pi$  bond, which is valence band, forms hybrid with  $\sigma$  orbital due to curvature of tube, but its effect is small. Therefore, on the basis of the energy dispersion  $E(k_x, k_y)$  of  $\pi$  band on graphene, the electronic structure of SWNTs is discretized due to quantization of  $\mathbf{k}$  in the direction perpendicular to the tube axis, and it is described as group of one-dimensional bands with continuous dispersion in the tube axis direction.

The energy band calculation of SWNTs using periodic boundary condition Eq. (1.9) has been done by N. Hamada et al. [33]. First Brillouin zone (FBZ) is shown in Fig. 1.5. The FBZ is expressed in the region surrounded with perpendicular bisector of straight lines connecting the original point and each reciprocal lattice point. The original

point of wave number space, the hexagon vertexes, and the midpoints of each side of hexagon is  $\Gamma$ , K or K', and M, respectively. Although, the K and K' point represent different states because they are not connected with each other by reciprocal lattice vector, they usually have the same dispersion relation because they are connected with symmetry with time reversal. 3 of 4 valance electrons in carbon atom occupy  $\sigma$  band and 1 of 4 occupies  $\pi$  band. The  $\pi$  band indicates dispersion which is proportional to wave number first order at near K and K' point and intersect at one point as shown in Fig. 1.4. In the case of SWNTs, only the wave function of the limited wave number vector within the Brillouin zone (BZ) of graphene is permitted due to the periodic boundary condition due to graphene sheet being wound in cylindrical shape. Figure 1.6 shows the example of available wave number vector of SWNTs. The wave number vector of the wave function is different for each chirality  $(n,m)$ . The cutting lines of this wave number vector which are parallel to vector  $\mathbf{K}_2$  determine the electronic state of each SWNT with  $(nm)$ . Connecting points of  $\pi$  band and anti-bonding  $\pi$  band are only K and K' point  $((\mathbf{b}_1 - \mathbf{b}_2)/3$ , where  $\mathbf{b}_1$  and  $\mathbf{b}_2$  are reciprocal lattice vectors, and  $\mathbf{b}_1 = 2\pi/\mathbf{a}_1$ ,  $\mathbf{b}_2 = 2\pi/\mathbf{a}_2$ ). Therefore, if available line passes through K or K' point, SWNTs become metal and if does not pass, SWNTs become semiconductor. As a result, whether the SWNTs state is metal or semiconductor is determined by the chirality. The SWNTs state becomes metal when  $n - m$  is multiple of 3, and it becomes semiconductor if it is not. Electron density of state (eDOS) of SWNTs becomes integration of energy dispersions along the lines with the cutting lines as shown in Fig. 1.6. The eDOS of SWNTs is given by following equation [16],

$$E = \pm\gamma_0 \sqrt{1 + 4 \cos\left(\frac{\sqrt{3}k_x a}{2}\right) \cos\left(\frac{k_y a}{2}\right) + 4 \cos^2\left(\frac{k_y a}{2}\right)}, \quad (1.14)$$

where  $\gamma_0$  is nearest neighbor overlap integral,  $k_x$  and  $k_y$  are x and y axis components of wave number vector. One-dimensional energy dispersion relationships at chiral index of (9,0) and (6,2) are shown in Fig. 1.7. Each curve described in Fig. 1.7 homologizes part of dotted line segments described in Fig. 1.6. (9,0) nanotube shown in Fig. 1.7(a) has a contact point on Fermi level and becomes metal. On the other hand, (6,2) nanotube, shown in Fig. 1.7(b) doesn't contact and becomes semiconductor. Based on the above, properties of SWNTs with  $(n,m)$  are shown in Fig. 1.8 [16].

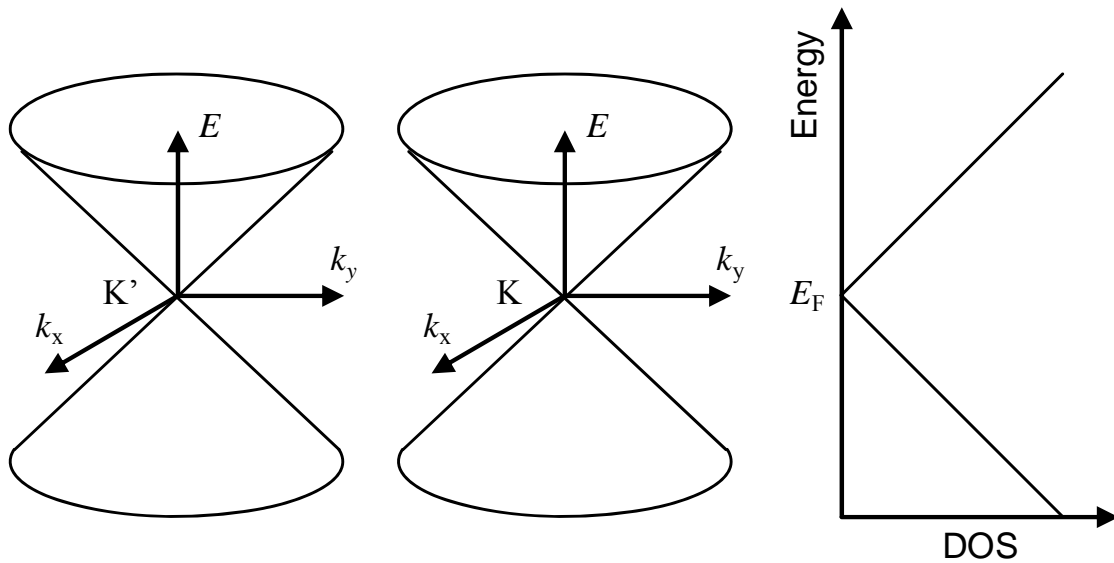


Figure 1.4. Schematic diagrams of  $\pi$  band near K and  $K'$  points, and density of state [36].

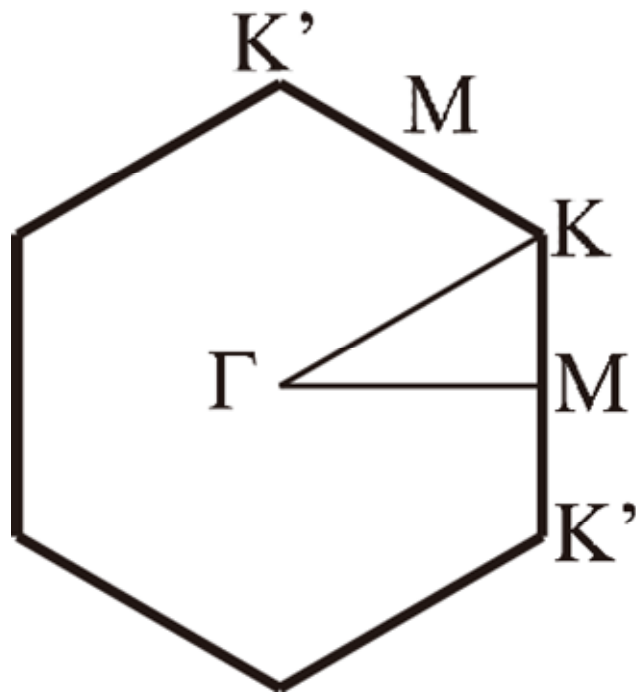


Figure 1.5. First Brillouin zone [33].

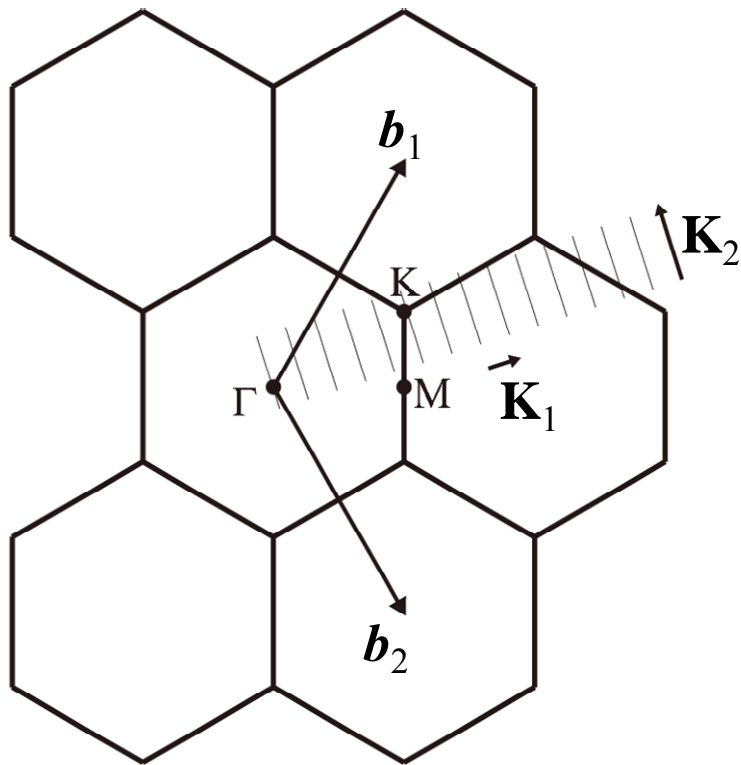


Figure 1.6. Wave number vector of CNTs.

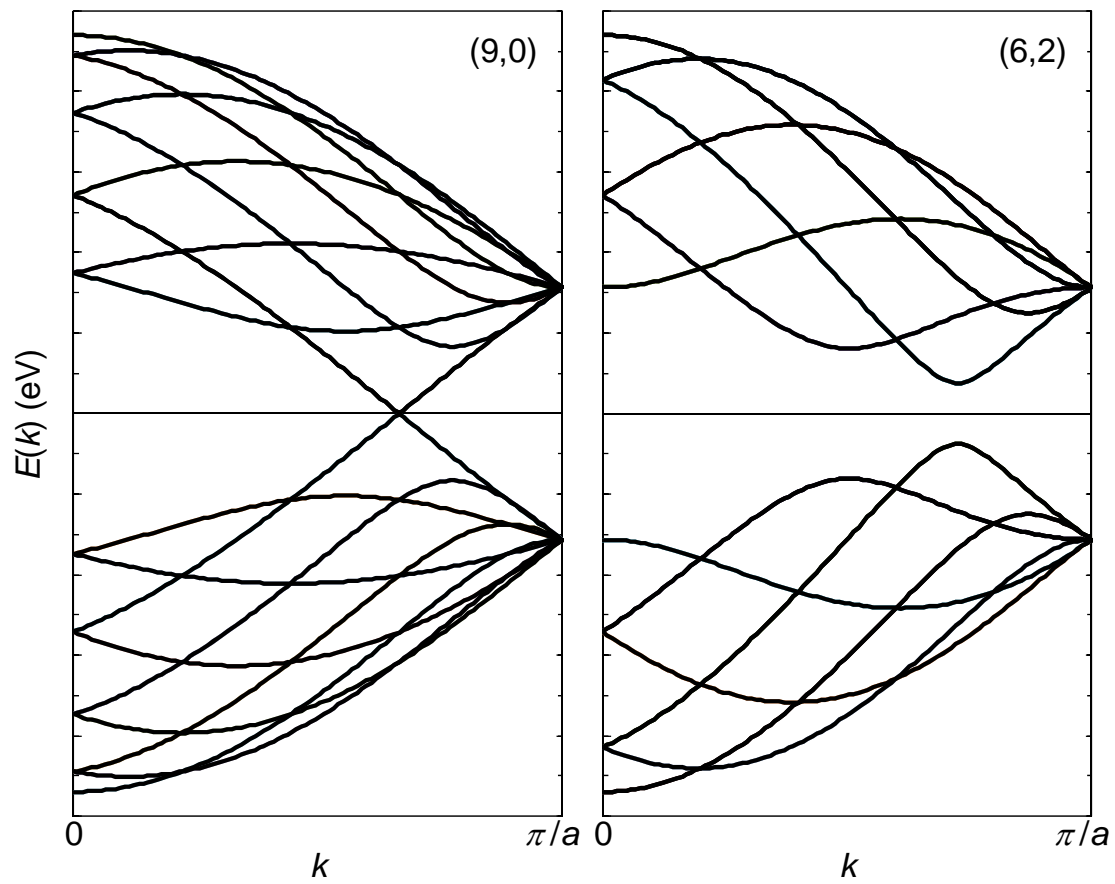


Figure 1.7. One-dimensional energy dispersion relationships of SWNTs with (9,0) and (6,2).

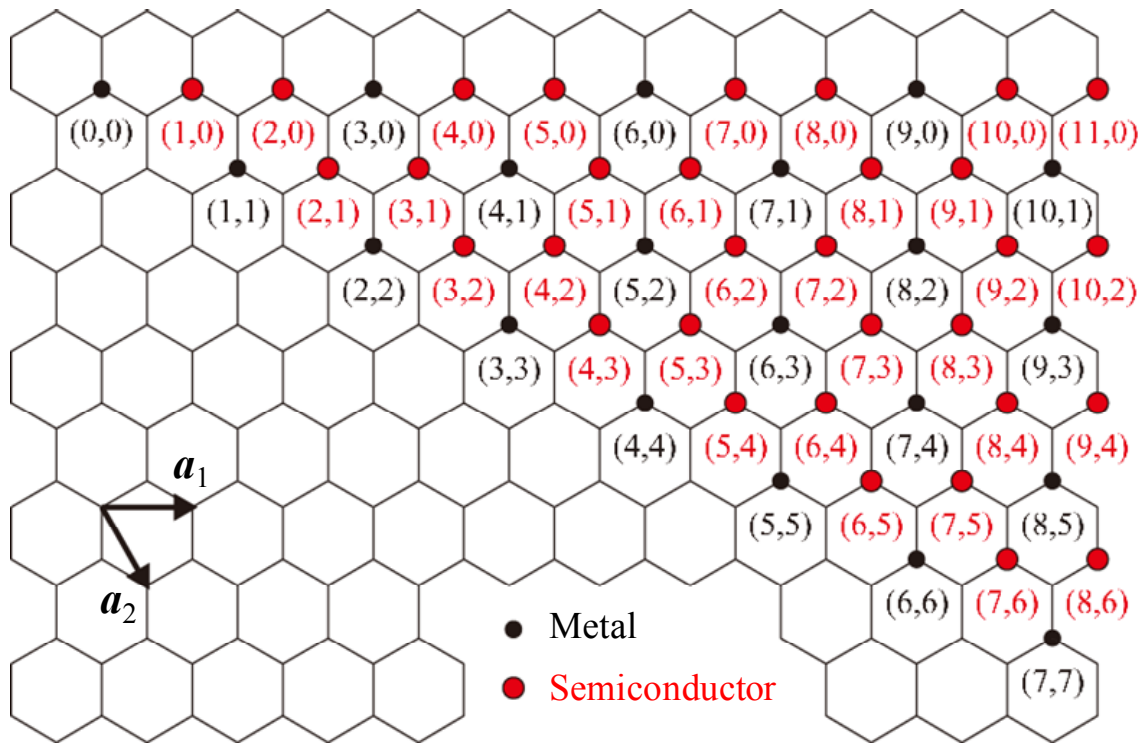


Figure 1.8. Relationship between chiral index and electrical property [16].

## 1.2 Graphene

Single atomic thick film configured in carbon atoms six-membered ring structures, i.e., graphene, have been successfully made by K. S. Novoselov et al. using mechanical exfoliation technique [2]. As for the physical properties of graphene, as mentioned in the CNTs section, this section describes it briefly. Graphene has highly electrical properties. Graphene has unique band structures near K and K' point in BZ shown in Fig. 1.4. Electrons dispersions around K and K' points are linear with respect to wave number and are equivalent to massless relativistic particles (Dirac fermion) [34-36]. 2s, 2p<sub>x</sub>, and 2p<sub>y</sub> orbitals form sp<sup>2</sup> hybrid orbital and σ band. On the other hand, p<sub>z</sub> orbital forms π band. Most of electronic properties of graphene originate from this π band. The band structure of graphene is described by Eq. (1.14). Carriers move at a constant speed ( $v_F = c/300$ , c is velocity of light) according to relativistic Dirac equation around K and K' point. Carrier mobility of graphene reaches several ten thousand cm<sup>2</sup>V<sup>-1</sup>s<sup>-1</sup> [37]. Electron mobility of graphene on SiO<sub>2</sub> substrate under room temperature has been reported that the value was 40,000 cm<sup>2</sup>V<sup>-1</sup>s<sup>-1</sup>. In addition, suspended graphene had 200,000 cm<sup>2</sup>V<sup>-1</sup>s<sup>-1</sup>.

Graphene has potentials for wide-range applications such as solar cells [38], transistor [39-42], transparent conducting electrodes [43-46], fuel cells [47], and so on. The electronic property of graphene changes by chemical modification. Graphene becomes an insulator due to hydration [48]. On the other hand, when graphene is fluorinated, graphene becomes a wide-gap semiconductor [49]. In addition, since these substances retain the structure of graphene, hydrogen and fluorine can be removed and returned to graphene. It is possible to synthesize two-dimensional substances having various physical properties by bonding various atoms or molecules.

### 1.3 Synthesis techniques for carbon nanomaterials

Synthesis techniques of carbon nanomaterials have been studied for many years. CNTs were discovered incidentally when fullerene was synthesized using carbon vaporization by the arc plasma [1]. SWNTs were also synthesized incidentally [4,5] at synthesizing metal particle inclusion carbon nanocapsule [50,51]. Graphene was first accomplished to manufacture by the elegant technique, i.e., mechanical exfoliation [2]. After this report, various techniques have been reported to try in the carbon nanomaterials syntheses. This section describes synthesis techniques and methods, which were employed in this study.

#### 1.3.1 Laser vaporization

Laser employing graphite vaporization was carried out originally in fullerene synthesis [3]. Kroto et al. synthesized fullerene using second harmonic Nd<sup>3+</sup>:YAG laser (532 nm) irradiating disk-shaped graphite at room temperature He (helium) ambient. Laser vaporization can synthesize SWNTs by using graphite mixed with catalysts as target [52-57]. Figure 1.9 shows an example of laser vaporization system. Graphite target is set at the center of the quartz tube inserted in the electric furnace and heated in to 1200 °C and Ar (argon) gas flow is induced to the quartz tube. When Nd<sup>3+</sup>:YAG laser is irradiated to graphite target from upstream side of the Ar flow to evaporate the graphite, Fullerene contained soot such as C<sub>60</sub> and C<sub>70</sub> is deposited on the inner wall of the quartz tube and the cooling section. In the case of using catalysts contained graphite, SWNTs can be synthesized. The material for synthesizing SWNTs is graphite with a few at.% of metal elements. Thess et al. used graphite containing 0.6 at.% Co (cobalt) and Ni (nickel) as target vaporized using 10 Hz repetition Nd<sup>3+</sup>:YAG with electric furnace at 1200 °C

and slow Ar flow (50 sccm) at 66.6 kPa to vaporize carbon and catalyst metal instantaneously. They succeeded in obtaining SWNTs with high yield of more than 70 % [53]. This high yield was achieved due to high temperature growth region and uniform evaporation of carbon. In particular, fundamental wave (1064 nm) irradiation with 50 ns delay from second harmonic wave (532 nm) irradiation generated uniform carbon and catalytic metal vapor. SWNTs were obtained with yield more than 70%, which exceeded 40-50% yield of 532 nm single-pulse laser. Instantaneously evaporated carbon grew to SWNTs by interaction of the catalytic metal evaporated at the same time. SWNTs were carried away from the growth region by Ar flow and adhere to cooling section. Laser vaporization can synthesize extremely high-crystallinity SWNTs. The signal ratio of the carbon six-membered ring structure and the lattice defects (G/D ratio, details are described in Chapter 2) which is a measure of crystallinity reaches approximately 50 [52]. However, the synthesis rate is small, and only 0.14 mg/min can be synthesized. In addition, it is difficult to scale up the synthesis amount. Although it is not problem at laboratory level, it is not suitable for the mass-production.

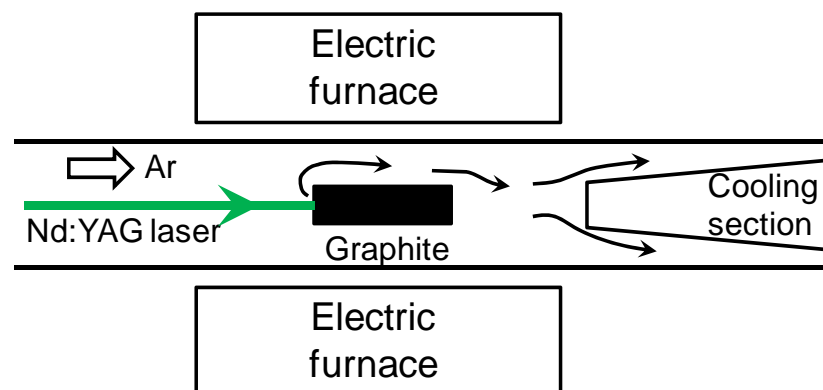
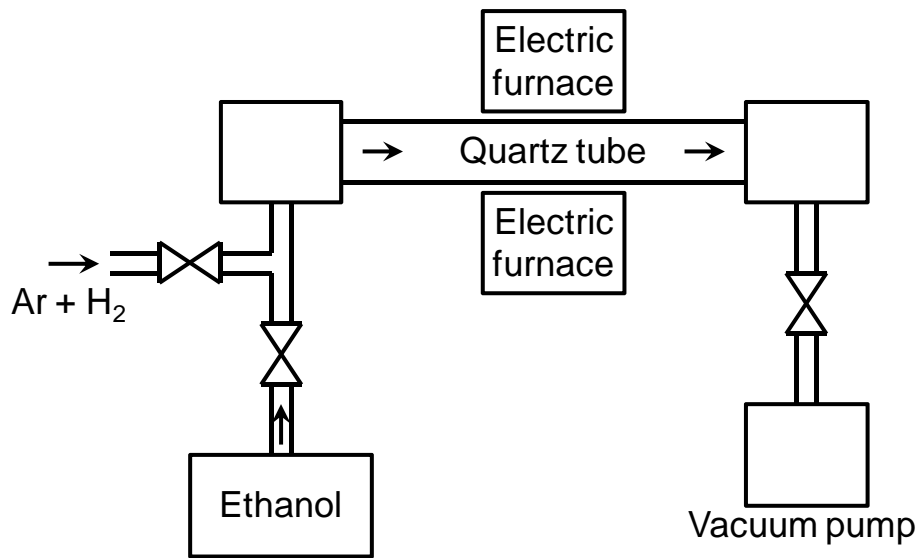


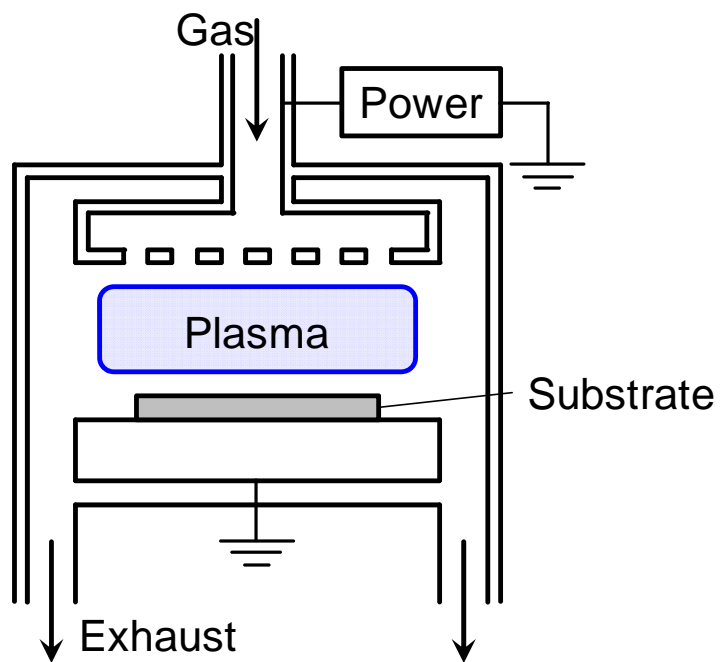
Figure 1.9. High temperature gas ambient laser vaporization apparatus for carbon nanomaterials synthesis.

### 1.3.2 Chemical vapor deposition (CVD)

Chemical vapor deposition (CVD) is a synthesis technique for SWNTs by the decomposition of alcohol vapor or the carbon atoms contained gas added energy by the heat [58-62] or the plasma [63,64]. Even with this method, the catalyst is necessary to synthesize SWNTs by CVD (catalytic CVD: CCVD), and the case of graphene synthesis is the same [65-67]. Figure 1.10 shows the thermal CCVD and plasma-enhanced CVD (PECVD) setup for carbon nanomaterials synthesis. In the thermal CCVD system shown in Fig. 1.10(a), the laser introduction part of laser vaporization technique is replaced with the alcohol vapor introduction part. Catalyst is dispersed in alcohols or applied on substrates and placed in the electric furnace. While Ar or Ar containing several percents of hydrogen ( $H_2$ ) is flowing in a quartz tube, the temperature raised to approximately  $800^\circ C$  by the electric furnace. After the temperature reached at  $800^\circ C$ , the gas flow was stopped and the inside of the quartz tube is evacuated. Alcohol vapor is flown into quartz tube in this state. The synthesis of SWNTs by CVD employing alcohol can be realized with a simple apparatus and its synthesis rate is high (8.3 g/min), the purity is high [59]. In addition, the water-assisted CVD, “supergrowth” greatly increases the synthesis amount of SWNTs [68,69]. However, synthesized SWNTs have many lattice defects (G/D: 10-20) [58,61]. In the case of synthesizing graphene, metal catalysts such as Ni [70-72], Cu (copper) [73,74], Ru (ruthenium) [75,76], and so on, were employed as the growth support base. Carbon sources are supplied from gases such as acetylene [71] and methane [77]. Carbon atoms generated from decomposed gases melting into metal and precipitated as a graphene on metal substrate surface. The CVD technique can synthesize CNTs or graphenes on the target location. Therefore, the CVD is an effective technique in the application for semiconductors.



(a) Thermal CCVD.



(b) PECVD

Figure 1.10. CVD system for carbon nanomaterials synthesis.

### 1.3.3 Arc plasma vaporization

In the plasma vaporization method for MWNTs synthesis, the arc plasma is generated between carbon electrodes and evaporating anode carbon electrode to synthesize CNTs. This method was used when MWNTs were discovered by Iijima [1]. Since the arc plasma vaporization was originally developed as a method during for the mass-production of fullerene, the fullerene is also synthesized at the same time when synthesizing MWNTs [78]. Synthesized MWNTs by the arc plasma were included in deposits on the top edge of cathode. The catalytic metal is necessary to synthesize SWNTs. The schematic diagram of arc plasma vaporization apparatus is shown in Fig. 1.11. Arc plasma for synthesizing CNTs is typically generated by applying direct current (DC) between carbon electrodes in several ten kPa processing gas. Alternate current (AC) and pulsed current also have been challenged but they are crushingly minority. When SWNTs were found for the first time, the catalytic metal was limited to Fe (iron) [4] or Co [5] to grow SWNTs. Shortly afterwards, SWNTs synthesized using Ni catalyst were reported by Saito et al. [79]. The reason why researchers were unable to find SWNTs or able to find SWNTs even though Fe, Co, and Ni of the same iron group element were used is that the synthesis conditions and the growth region were slightly different between these catalysts. In the case of using Fe as a catalyst, SWNTs cannot be synthesized unless the ambient gas is made to be a mixed gas of Ar and H<sub>2</sub> or Ar and CH<sub>4</sub> (methane). On the other hand, SWNTs cannot be synthesized under the same conditions for Co or Ni catalyst. In this condition, SWNTs were synthesized in the pure He gas. In addition, the locations of growth regions were different for these catalysts. In the case of Co, SWNTs were synthesized in soot deposited on chamber wall. On the other hand, in Ni, soot was adhering to the periphery of the cathode. Catalytic metals for synthesizing

SWNTs are generally contained in the carbon electrode on the anode side. There are several ways to make anode carbon electrode containing catalytic metals. The easiest method is to pierce a graphite rod of high purity (approximately 99.99%) and pack a mixture of metal powder and graphite powder into the hole. However, this method cannot uniformly mix the catalytic metal and graphite in the electrode. The yield, growth morphology, and so on, of SWNTs obtained by the arc plasma vaporization are investigated for various catalytic metals. Table 1.1 shows the metal elements which have been shown to have the catalytic ability for SWNTs synthesis. The effect of increasing yield by mixing the two kinds of metals appears most remarkably in Fe-Ni [84, 85] and Ni-Y (yttrium) [92-99]. The production rate of SWNTs can be markedly improved using mixing these catalytic metals at appropriate ratio. SWNTs which are synthesized by the arc plasma vaporization have high-crystallinity (G/D ratio: 15-35) [100-102]. Synthesis rate of SWNTs in the arc plasma vaporization reaches gram-per-minute order (~1.48 g/min) [93,96]. In addition, the preheating is unnecessary in the arc plasma vaporization because the arc plasma itself maintains high temperatures for reactions (more than 4000 K) [103]. The arc plasma vaporization technique is expected to be a method for synthesizing SWNTs with high-crystallinity in the short-time.

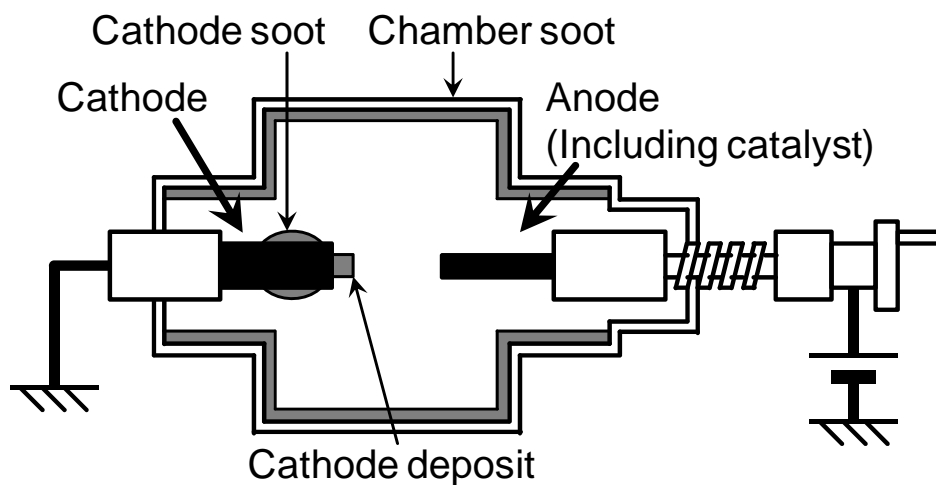


Figure 1.11. Arc plasma vaporization system for SWNTs synthesis.

Table 1.1. Catalytic metals used for SWNTs synthesis.

Metal	Catalytic ability	References
Iron group	Fe	Very weak
	Co	Middle
	Ni	Weak
	Fe-Ni	Strong
	Co-Ni	Very strong
Platinum group	Rh	Middle
	Rh-Pt	Strong
Rare earth	Y	Middle
	La	Middle
Iron-Rare earth mixture	Ni-Y	Very strong

#### 1.3.4 In-liquid plasma employing alcohol

Novel carbon nanomaterials synthesis methods have been widely studied. The plasma is generally generated in the gas phase. Plasma generated from the liquid region generates new-reactions due to plasma-liquid interactions. Various types of plasma-liquid reactions equipments have been developed. The plasma is generated with two electrodes immersed into the liquid or electrodes faced each other across liquid surface, which are called in-liquid plasma. In-liquid plasma treatment techniques are expected to apply water purifications [104-108], materials syntheses [109-130,132], and so on.

Figure 1.12 shows various types of in-liquid plasma configurations. Plasma was generated by various types of power supply such as AC [105,106,117,120,131], DC [110,116,118,119,121,123,124,126,127,129], and pulse [107-109,111,112,114,115,122,125,128,130,132]. In-liquid plasma system can be categorized into two types. One is both electrodes submerged in the liquid and the plasma as shown in Fig. 1.12(a) [104-107,109-114,121-129,132]. This type typically needs bubbles near gap between electrodes to generate the plasma or the streamer corona is generated. It is thought that discharge forms are affected by kinds of liquids, shape of electrodes, electrodes arrangement, and types of power supplies. In the case of micro-gap in-liquid plasma, bubbles are generated at the plasma ignition by joule heating [105,109,111,112,114,122,132], ultrasonic cavitation [110], gas introducing [104,129], and so on. On the other hand, the streamer corona is generated using high energy inputs [104-107].

Another type of in-liquid plasma is electrodes placed facing across liquid surface [108,115-120,130]. In this case, discharge configurations are categorized into two types. In the case of using electrically conductive liquids, liquid acts as electrode shown

in Fig. 1.12(b). Therefore, the plasma is generated between electrode placed at the gas phase and the liquid surface [104,118-120]. In the case of using low-electrical conductivity liquids, the plasma is generated at the gas phase and the plasma contacts the liquid surface. The liquid is evaporated by the plasma contact and the liquid components were dissociated to molecules by electron-collision-induced reactions. The plasma is generated also inside the liquid and the discharge connects from the electrode placed at the gaseous phase to the electrode placed at the liquid phase as, shown in Fig. 1.12(c) [115-117].

In-liquid plasmas are applied to carbon nanomaterials. Carbon sources for carbon nanomaterials syntheses are supplied as electrodes [126-129], liquid [109-117,122,123,125], or both [121,124]. The in-liquid plasma can synthesize carbon nanomaterials with a high synthesis rate due to the carbon source supplied at the high density comparing with gas phase. The in-liquid plasma produces unprecedented reactions at the plasma-gas interface and the plasma-liquid interface. It is expected to be applied to material processings, material syntheses, and so on; however, the elucidation of reaction mechanisms between the plasma and the liquid are one of important issues.

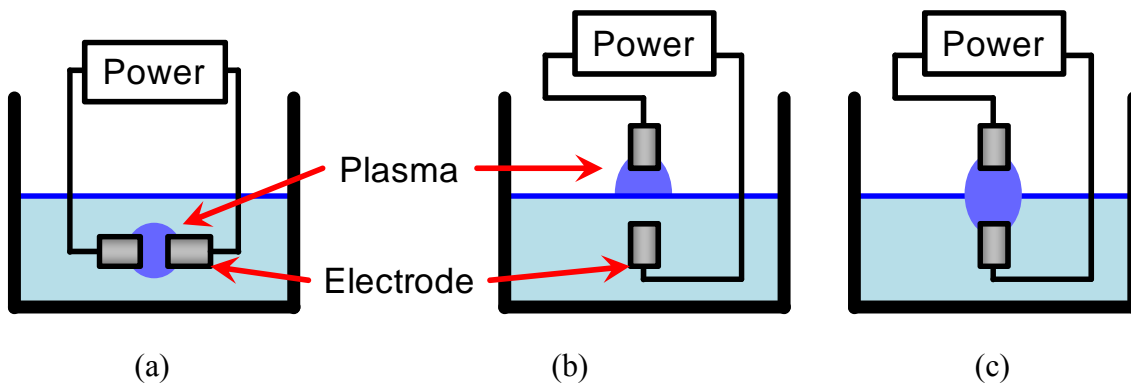


Figure 1.12. In-liquid plasma configurations. (a) Plasma was generated between submerged two electrodes. (b) Facing each other across liquid surface, liquid behaves as electrode due to its conductivity. (c) Plasma penetrates liquid and reaches liquid side electrode.

## 1.4 Previous studies

### 1.4.1 Arc plasma for SWNTs synthesis

Studies about SWNTs synthesis using the arc plasma have been carried out. Synthesis mechanism of SWNTs by the arc plasma is one of important themes because the control of SWNTs quality is necessary for applications. The arc plasma has very high temperature (approximately 4000~ K) and too intense emission light. The plasma diagnostics using probes are impossible due to its high temperature. The active measurement of plasma, such as laser-induced fluorescence spectroscopy, enables us to measure chemical species densities and temperatures but too strong emission light from arc plasmas becomes strong noise. On the other hand, this high intensity emission light includes the information of active species in the arc plasma. Therefore, measuring optical emission of arc plasma during the SWNTs synthesis using spectrometer, i.e., optical emission spectroscopy (OES) has been applied to diagnose the arc plasma [81,99].

Guo et al. reported the relationship between ambient gas conditions and emission spectra in use of Fe as a catalyst and H<sub>2</sub>, Ar, or Ar-H<sub>2</sub> mixture gases [81]. They changed the ambient gas and measured Fe and carbon diatomic (C<sub>2</sub>) emissions at Swan band system ( $\Delta v = -1$ ). In the case of using the Ar, the amount of anode evaporation was very small and Fe atom emissions were detected and C<sub>2</sub> emissions were hardly observed. In the case of using H<sub>2</sub>, Fe atom emissions were very weak and C<sub>2</sub> emissions were stronger than those in the case of using the Ar and the amount of anode evaporation was very high; however SWNTs productivity was low. In the case of using H<sub>2</sub>-Ar, C<sub>2</sub> and Fe emissions were observed and their intensities were strong. In addition, SWNTs synthesis amount was the highest in these three conditions.

Li et al. reported under the magnetic field SWNTs synthesis using arc plasma

employing the Ni-Y catalyst [99]. Magnetic field behaves as the Ni attractor. They found that Ni intensities compared with C<sub>2</sub> intensities were changed between with and without magnetic field condition. In addition, G/D ratios were also different.

These two results suggested that carbon active species and excited catalytic metals interactions have played important roles to grow SWNTs. In the laser vaporization, OES was also done and C<sub>2</sub> and catalytic metals were also detected [54,55,133,134]. Therefore, it is thought that main carbon source of SWNTs growth will be C<sub>2</sub>.

Various SWNTs with different crystallinities were synthesized. The measurement using OES has been carried out but it is not said that sufficient researches have been done on the view point of SWNTs growths with different crystallinities when synthesis conditions are changed. It is necessary to clarify reactions between catalytic metals and C<sub>2</sub> and synthesized SWNTs on the basis of measurement of arc plasma between different conditions.

#### 1.4.2 In-liquid plasma for graphene synthesis

The nano-meter-order domain size graphene, i.e., nanographene, synthesized using the in-liquid plasma employing various types of liquids was reported and this technique could synthesize nanographenes with different crystallinities employing different types of liquids [109,117]. In the gas-liquid phase electrodes configuration, ethanol or 1-butanol as for a feed material in-liquid plasma was used for synthesizing nanographene [117]. Synthesis rates and crystallinity of synthesized nanographene were different between ethanol and 1-butanol. Ethanol employed for the in-liquid plasma had the synthesis rate of 0.61 mg/min and the crystallinity which evaluated from Raman scattering spectroscopy was high. On the other hand, 1-butanol employed for the

in-liquid plasma synthesized nanographene on 1.72 mg/min but crystallinity was lower than ethanol. It is thought that there are a trade-off relationship between the synthesis rate and the crystallinity. These differences were thought to be due to differences in alcohols structures, but the mechanism was unclear.

Carbon nanomaterials synthesis using plasma processes enhance efficiency of synthesis. Control of quality of synthesized materials is one of problems for applications. Clarification of synthesis mechanisms provides solutions of quality control. Clarification of interaction between carbons, catalytic materials, and other chemical species during synthesis is contributory to identify the condition for highly crystalline carbon nanomaterials.

### 1.5 Purpose and composition of this thesis

Reactions in plasmas have played important roles for the synthesis of carbon nanomaterials. Arc plasma for SWNTs synthesis and in-liquid plasma are generated under high-density media. These plasmas differ in properties from plasma used in semiconductor manufacturing process and atmospheric pressure plasma generated in gas phase. Plasma conditions for the synthesis affect the characterization of properties of synthesized carbon nanomaterials. Plasma diagnostics enables us to estimate properties of chemical species.

In SWNTs synthesis by the arc plasma, carbon species and catalytic metals interaction and their state are important factors [81,99]. However, the relationship between these species and crystallinity has not been clarified. This is because reports are limited to the synthesis results in which the conditions were changed and the plasma diagnostics results in one condition, and the verification is not performed sufficiently. It

is thought that effects of chemical species and plasma on synthesized SWNTs are changed by different conditions. For the diagnostics of plasma during synthesis process, non-contact measurement techniques are desirable because the plasma is not disturbed. OES enables us to estimate present excited chemical species in the plasma and states of them. Measurements were carried out at different conditions, and these results were compared them with those of crystallographic evaluations of synthesized SWNTs. The relationship between active species in the plasma and the characteristics of crystallinities were clarified, and the conditions under which SWNTs with the high crystallinity were synthesized were also clarified. Crystallinity is one of important factors to characterize property of carbon nanomaterials. It is an advantage of arc plasma method that SWNTs with high crystallinity can be synthesized, but SWNTs has low purity and it is necessary to remove impurities in order to extract SWNTs. Crystallinity is concerned with whether or not the performance of SWNTs is exhibited at a value close to the theoretical value. In order to make use of the high crystallinity of SWNTs synthesized by arc plasma method, it is conceivable to apply it while leaving the catalytic metals at the base of SWNTs, for example, to apply SWNTs to resin for application to transparent conducting films [135,136].

Researches on synthesis of nanographene using the in-liquid plasma have become active in recent years, but reports on plasma measurements are few. Various types of liquids have been employed as raw materials for the synthesis of nanographene. In-liquid plasmas employing various types of alcohols could synthesize nanographenes with different synthesis rates and crystallinities. Reactions between in-liquid plasmas and alcohols are one of notable point to clarify the synthesis mechanism. Plasma parameters may be changed depending on alcohols types. Measurement of the in-liquid plasma is

effective approaches to investigate synthesis reactions. In addition, as the in-liquid plasma treatment alcohols immediately changed to other substances. Residual liquids after the filtration to collect nanographene include intermediate and by-products. Therefore, the analysis of residual liquids also enables us to support the clarification of synthesis mechanism.

In this study, these synthesis techniques were investigated to clarify the synthesis mechanisms of highly crystalline carbon nanomaterials using optical diagnostics of plasma and analysis of synthesized materials.

In the first chapter, SWNTs and graphene physical properties, their synthesis methods, and previous studies are explained.

In chapter 2, the experimental apparatuses of SWNTs synthesis using arc plasma and nanographene synthesis using the in-liquid plasma are described. The principles of the measurement technique of plasma and evaluation techniques for carbon nanomaterials are explained together with apparatuses used this study.

In chapter 3, Ni-Y catalysts employed for the arc plasma for synthesizing SWNTs is measured by OES to clarify relationships between active species in the arc plasma and synthesized SWNTs. For the growth of SWNTs, catalytic metals are necessary. Therefore, catalytic metals states in the arc plasma have given effects on the growth of SWNTs. OES results are compared with those of crystallographic evaluations of SWNTs.

In chapter 4, the in-liquid plasma employing various types of alcohols is measured using OES and detected active species information are compared with synthesized nanographene properties to clarify nanographene synthesis reactions in the in-liquid plasma. The by-products and intermediates in residual liquids are also analyzed

to clarify reactions pathways.

In chapter 5, nanographene is synthesized using liquids other than alcohols as raw materials, and the differences in reactions in various liquids are investigated based on the differences. Comparing alcohols, *n*-hexane, and benzene were employed. In particular, the presence or absence of hydroxyl group is noted, and the roles of oxygen species in nanographene synthesis by in-liquid plasma are discussed.

In chapter 6, the crystallinity control of in-liquid plasma synthesizing nanographene is attempted using methanol as added agent based on results of chapters 4 and 5. Oxygen species in the in-liquid plasma originated from raw materials have given the effective roles to formation of crystal structures. The results show a high potential to control the crystallinity of synthesized nanographene using oxygen species.

Finally, relationships between chemical species in the plasma and carbon nanomaterials synthesized with high crystallinity are discussed and the present study is summarized in chapter 7.

## References

- [1] S. Iijima, "Helical microtubules of graphitic carbon", *Nature* **354**, pp.56-58 (1991).
- [2] K. S. Novoselov, A. K. Geim, S. V. Morozov, D. Jiang, Y. Zhang, S. V. Dubonos, I. V. Grigorieva, and A. A. Firsov, "Electric Field Effect in Atomically Thin Carbon Films", *Science* **306**, pp.666-669 (2004)
- [3] H. W. Kroto, J. R. Heath, S. C. O'Brien, R. F. Crul, and R. E. Smalley, "C<sub>60</sub>: Buckminsterfullerene", *Nature* **318**, pp.162-163 (1985).
- [4] S. Iijima and T. Ichihashi, "Single-shell carbon nanotubes of 1-nm diameter", *Nature* **363**, pp.603-605 (1993).
- [5] D. S. Bethune, C. H. Klang, M. S. de Vries, G. Gorman, R. Savoy, J. Vazquez, and R. Beyers, "Cobalt-catalysed growth of carbon nanotubes with single-atomic-layer walls", *Nature* **363**, pp.605-607 (1993).
- [6] M. M. J. Treacy, T. W. Ebbesen, and J. M. Gibson, "Exceptionally high Young's modulus observed for individual carbon nanotubes", *Nature* **381**, pp.678-680 (1996).
- [7] M. Yu, O. Lourie, M. J. Dyer, K. Moloni, T. F. Kelly, and R. S. Ruoff, "Strength and Breaking Mechanism of Multiwalled Carbon Nanotubes Under Tensile Load", *Science* **287**, pp.637-640 (2000).
- [8] T. Choi, D. Poulidakos, J. Tharian, and U. Sennhauser, "Measurement of thermal conductivity of individual multiwalled carbon nanotubes by the 3- $\omega$  method", *Appl. Phys. Lett.* **87**, 013108 (2005).
- [9] T. Choi, D. Poulidakos, J. Tharian, and U. Sennhauser, "Measurement of the Thermal Conductivity of Individual Carbon Nanotubes by the Four-Point Three- $\omega$  Method", *Nano Lett.* **6**, pp.1589-1593 (2006).
- [10] B. Q. Wei, R. Vajtai, and P. M. Ajayan, "Reliability and current carrying capacity of carbon nanotubes", *Appl. Phys. Lett.* **79**, pp.1172-1174 (2001).
- [11] N. Yao and V. Lordi, "Young's modulus of single-walled carbon nanotubes", *J. Appl. Phys.* **84**, pp.1939-1943 (1998).
- [12] F. Li, H. M. Cheng, S. Bai, G. Su, and M. S. Dresselhaus, "Tensile strength of single-walled carbon nanotubes directly measured from their macroscopic ropes",

- Appl. Phys. Lett. **77**, pp.3161-3163 (2000).
- [13] E. Pop, D. Mann, Q. Wang, K. Goodson, and H. Dai, “Thermal Conductance of an Individual Single-Wall Carbon Nanotubes above Room Temperature”, Nano Lett. **6**, pp.96-100 (2006).
- [14] J. Hone, M. C. Llaguno, N.M. Nemes, A.T. Johnson, J. E. Fischer, D. A. Walters, M. J. Casavant, J. Schmidt, and R. E. Smalley, “Electrical and thermal transport properties of magnetically aligned single wall carbon nanotube films”, Appl. Phys. Lett. **77**, pp.666-668 (2000).
- [15] X. Zhou, J. Y. Park, S. Huang, J. Liu, and P. L. McEuen, “Band Structure Phonon Scattering, and the Performance Limit of Single-Walled Carbon Nanotube Transistors”, Phys. Rev. Lett. **95**, 146805 (2005).
- [16] R. Saito, M. Fujita, G. Dresselhaus, and M. S. Dresselhaus, “Electronic structure of chiral graphene tubes”, Appl. Phys. Lett. **60**, pp.2204-2206 (1992).
- [17] J. Chen, M. A. Hamon, H. Hu, Y. Chen, A. M. Rao, P. C. Eklund, and R. C. Haddon, “Solution Properties of Single-Walled Carbon Nanotubes”, Science **282**, pp.95-98 (1998).
- [18] M. A. Correa-Duarte, N. Sobal, L. M. Liz-Marzán, and M. Giersig, “Linear Assemblies of Silica-Coated Gold Nanoparticles Using Carbon Nanotubes as Templates”, Adv. Mater. **16**, pp.2179-2184 (2004).
- [19] M. Estili, H. Kwon, A. Kawasaki, S. Cho, K. Takagi, K. Kikuchi, and M. Kawai, “Multiwalled carbon nanotube-reinforced ceramic matrix composites as a promising structural material” J. Nucl. Mater. **398**, pp.244-245 (2010).
- [20] E. T. Thostenson and T. Chou, “On the elastic properties of carbon nanotube-based composites: modelling and characterization”, J. Phys. D: Appl. Phys. **36**, pp.573-582 (2003).
- [21] Y. Li, D. Mann, M. Rolandi, W. Kim, A. Ural, S. Hung, A. Javey, J. Cao, D. Wang, E. Yenilmez, Q. Wang, J. F. Gibbons, Y. Nishi, and H. Dai, “Preferential Growth of Semiconducting Single-Walled Carbon Nanotubes by a Plasma Enhanced CVD Method” Nano Lett. **4**, pp.317-321 (2004).
- [22] H. Ohnaka Y. Kojima, S. Kishimoto, Y. Ohno, and T. Mizutani, “Fabrication of Carbon Nanotube Field Effect Transistors Using Plasma-Enhanced Chemical

- Vapor Deposition Grown Nanotubes” Jpn. J. Appl. Phys. **45**, pp.5485-5489 (2006).
- [23] A. Javey, J. Guo, Q. Wang, M. Lundstrom, and H. Dai, “Ballistic carbon nanotube field-effect transistors” Nature **424**, pp.654-657 (2003).
- [24] J. Dijon, A. Fournier, P. D. Szkutnik, H. Okuno, C. Jayet, and M. Fayolle, “Carbon nanotubes for interconnects in future integrated circuits: The challenge of the density” Diamond Relat. Mater. **19**, pp.382-388 (2010).
- [25] M. Sato, T. Hyakushima, A. Kawabata, T. Nozue, S. Sato, M. Nihei, and Y. Awano, “High-Current Reliability of Carbon Nanotube Via Interconnects” Jpn. J. Appl. Phys. **49**, 105102 (2010).
- [26] Y. Saito and S. Uemura, “Field emission from carbon nanotubes and its application to electron sources” Carbon **38**, pp.169-182 (2000).
- [27] B. Gao, A. Kleinhammes, X. P. Tang, C. Bower, L. Fleming, Y. Wu, and O. Zhou, “Electrochemical intercalation of single-walled carbon nanotubes with lithium” Chem. Phys. Lett. **307**, pp.153-157 (1999).
- [28] J. Ma, J. Tang, H. Zhang, N. Shinya, and L. Qin, “Ultrathin Carbon Nanotube Fibrils of High Electrochemical Capacitance” ACS Nano **3**, pp.3679-3683 (2009).
- [29] P. W. Ruch, R. Kötz, and A. Wokaun “Electrochemical characterization of single-walled carbon nanotubes for electrochemical double layer capacitors using non-aqueous electrolyte” Electrochim. Acta **54**, pp.4451-4458 (2009).
- [30] R. A. Jishi, L. Venkataraman, M. S. Dresselhaus, and G. Dresselhaus, “Symmetry properties of chiral carbon nanotubes” Phys. Rev. B **51**, pp.11176-11179 (1995).
- [31] M. S. Dresselhaus, G. Dresselhaus, and R. Saito, “Carbon fiber based on C<sub>60</sub> and their symmetry” Phys. Rev. B **45**, pp.6234-6242 (1992).
- [32] P. R. Wallace, “The Band Theory of Graphite” Phys. Rev. **71**, pp.622-634 (1947).
- [33] N. Hamada, S. Sawada, and A. Oshiyama, “New One-Dimensional Conductors: Graphitic Microtubules” Phys. Rev. Lett. **68**, pp.1579-1581 (1992).
- [34] J. W. McClure “Diamagnetism of Graphite” Phys. Rev. **104**, pp.666-671 (1956).
- [35] J. C. Slonczewski and P. R. Weiss “Band Structure of Graphite” Phys. Rev. **109**, pp.272-279 (1958).
- [36] T. Ando “Theory of Electronic States and Transport in Carbon Nanotubes” J.

- Phys. Soc. Jpn. **74**, pp.777-817 (2005).
- [37] J. Chen, C. Jang, S. Xiao, M. Ishigami, and M. S. Fuhrer, "Intrinsic and extrinsic performance limits of graphene devices on SiO<sub>2</sub>" Nat. Nanotechnol. **3**, pp.206-209 (2008).
- [38] M. Zhong, D. Xu, X. Yu, K. Huang, X. Liu, Y. Qu, Y. Xu, and D. Yang, "Interface coupling in graphene/fluorographene heterostructure for high-performance graphene/silicon solar cells" Nano Energy **28**, pp.12-18 (2016).
- [39] T. J. Echtermeyer, M. C. Lemme, M. Baus, B. N. Szafrank, A. K. Geim, and H. Kurz, "Nonvolatile Switching in Graphene Field-Effect Devices" IEEE Electron Device Lett. **29**, pp.952-954 (2008).
- [40] Y.-M. Lin, C. Dimitrakopoulos, K. A. Jenkins, D. B. Farmer, H.-Y. Chiu, A. Grill, and Ph. Avouris, "100-GHz Transistors from Wafer-Scale Epitaxial Graphene" Science **327**, p.662 (2010).
- [41] F. Torrisi, T. Hasan, W. Wu, Z. Sun, A. Lombardo, T. S. Kulmala, G. Hsieh, S. Jung, F. Bonaccorso, P. J. Paul, D. Chu, and A. C. Ferrari, "Inkjet-Printed Graphene Electronics" ACS Nano **6**, pp.2992-3006 (2012).
- [42] G. Liu, S. Ahsan, A. G. Khitun, R. K. Lake, and A. A. Balandin, "Graphene-based non-Boolean logic circuits" J. Appl. Phys. **114**, 154310 (2013).
- [43] X. Li, W. Chen, S. Zhang, Z. Wu, P. Wang, Z. Xu, H. Chen, W. Yin, H. Zhong, and S. Lin, "18.5% efficient graphene/GaAs van der Waals heterostructure solar cell" Nano Energy **16**, pp.310-319 (2015).
- [44] X. Wang, L. Zhi, and K. Müllen, "Transparent, Conductive Graphene Electrodes for Dye-Sensitized Solar Cells" Nano Lett. **8**, pp.323-327 (2008).
- [45] J. Wu, M. Agrawal, H. A. Becerril, Z. Bao, Z. Liu, Y. Chen, and P. Peumans "Organic Light-Emitting Diodes on Solution-Processed Graphene Transparent Electrodes" ACS Nano **4**, pp.43-48 (2010).
- [46] P. Matyba, H. Yamaguchi, G. Eda, M. Chhowalla, L. Edman, and N. D. Robinson, "Graphene and Mobile Ions: The Key to All-Plastic, Solution-Processed Light-Emitting Devices" ACS Nano **4**, pp.637-642 (2010).
- [47] S. Hu, M. Lozada-Hidalgo, F. G. Wang, A. Mishchenko, F. Schedin, R. R. Nair, E. W. Hill, D. W. Boukhvalov, M. I. Katsnelson, R. A. W. Dryfe, I. V. Grigorieva, H.

- A. Wu, and A. K. Geim, "Proton transport through one-atom-thick crystals" *Nature* **516**, pp.227-230 (2014).
- [48] D. C. Elias, R. R. Nair, T. M. G. Mohiuddin, S. V. Morozov, P. Blake, M. P. Halsall, A. C. Ferrari, D. W. Boukhvalov, M. I. Katsnelson, A. K. Geim, and K. S. Novoselov, "Control of Graphene's Properties by Reversible Hydrogenation: Evidence for Graphane" *Science* **323**, pp.610-613 (2009).
- [49] S.-H. Cheng, K. Zou, F. Okino, H. R. Gutierrez, A. Gupta, N. Shen, P. C. Eklund, J. O. Sofo, and J. Zhu, "Reversible fluorination of graphene: Evidence of a two-dimensional wide bandgap semiconductor" *Phys. Rev. B* **81**, 205435 (2010).
- [50] R. S. Ruoff, D. C. Lorents, B. Chan, R. Malhotra, and S. Subramoney, "Single Crystal Metals Encapsulated in Carbon Nanoparticles" *Science* **259**, pp.346-348 (1993).
- [51] M. Tomita, Y. Saito, and T. Hayashi, "LaC<sub>2</sub> Encapsulated in Graphite Nano-Particle" *Jpn. J. Appl. Phys.* **32**, L280 (1993).
- [52] M. Yudasaka, R. Yamada, N. Sensui, T. Wilkins, T. Ichihashi, and S. Iijima, "Mechanism of the Effect of NiCo, Ni and Co Catalysts on the Yield of Single-Wall Carbon Nanotubes Formed by Pulsed Nd:YAG Laser Ablation" *J. Phys. Chem. B* **103**, pp.6224-6229 (1999).
- [53] A. Thess, R. Lee, P. Nikolaev, H. Dai, P. Petit, J. Robert, C. Xu, Y. H. Lee, S. G. Kim, A. G. Rinzler, D. T. Colbert, G. E. Scuseria, D. Tománek, J. E. Fischer, and R. E. Smalley, "Crystalline Ropes of Metallic Carbon Nanotubes" *Science* **273**, pp.483-487 (1996).
- [54] A. A. Puretzky, D. B. Geohegan, X. Fan, and S. J. Pennycook, "Dynamics of single-wall carbon nanotubes synthesis by laser vaporization" *Appl. Phys. A* **70**, pp.153-160 (2000).
- [55] A. A. Puretzky, D. B. Geohegan, X. Fan, and S. J. Pennycook, "In situ imaging and spectroscopy of single-wall carbon naotube synthesis by laser vaporization" *Appl. Phys. Lett.* **76**, pp.182-184 (2000).
- [56] A. A. Puretzky, H. Schittenhelm, X. Fan, M. J. Lance, L F. Allard Jr., and D. B. Geohegan, "Investigations of single-wall carbon nanotube growth by time-restricted laser vaporization" *Phys. Rev. B* **65**, 245425 (2002).

- [57] D. B. Geohegan, H. Schittenhelm, X. Fan, S. J. Pennycook, A. A. Puzos, M. A. Guillorn, D. A. Blom, and D. C. Joy, "Condensed phase growth of single-wall carbon nanotubes from laser annealed nanoparticles" *Appl. Phys. Lett.* **78**, pp.3307-3309 (2001).
- [58] H. Yan, Q. Li, J. Zhang, and Z. Liu, "Possible tactics to improve the growth of single-walled carbon nanotubes by chemical vapor deposition" *Carbon* **40**, pp.2693-2698 (2002).
- [59] Y. Li, L. Zhang, X. Zhong, and A. H. Windle, "Synthesis of high purity single-walled carbon nanotubes from ethanol by catalytic gas flow CVD reactions" *Nanotechnol.* **18**, 225604 (2007).
- [60] S. Maruyama, R. Kojima, Y. Miyauchi, S. Chiashi, and M. Kohno, "Low-temperature synthesis of high-purity single-walled carbon nanotubes from alcohol" *Chem. Phys. Lett.* **360**, pp.229-234 (2002).
- [61] C. Seah, S. Chai, S. Ichikawa, and A. R. Mohamed, "Parametric Study of Methane Catalytic CVD into Single-walled Nanotubes Using Spin-coated Iron Nanoparticles" *Chem. Vapor Deposition* **19**, pp.53-60 (2013).
- [62] J. Qiu, Y. Au, Z. Zhao, Y. Li, and Y. Zhou, "Catalytic synthesis of single-walled carbon nanotubes from coal gas by chemical vapor deposition method" *Fuel Proc. Technol.* **85**, pp.913-920 (2004).
- [63] R. K. Garg, T. N. Anderson, R. P. Lucht, T. S. Fisher, and J. P. Gore, "Gas temperature measurements in a microwave plasma by optical emission spectroscopy under single-wall carbon nanotube growth conditions" *J. Phys. D: Appl. Phys.* **41**, 095206 (2008).
- [64] M. Hiramatsu, T. Deguchi, H. Nagao, and M. Hori, "Aligned Growth of Single-Walled and Double-Walled Nanotube Films by Control of Catalyst Preparation" *Jpn. J. Appl. Phys.* **46**, pp.L303-L306 (2007).
- [65] A. Reina, X. Jia, J. Ho, D. Nezich, H. Son, V. Bulovic, M. S. Dresselhaus, and J. Kong, "Large Area, Few-Layer Graphene Films on Arbitrary Substrates by Chemical Vapor deposition" *Nano. Lett.* **9**, pp.30-35 (2009).
- [66] P. Zhao, S. Kim, X. Chen, E. Einarsson, M. Wang, Y. Song, H. Wang, S. Chiashi, R. Xiang, and S. Maruyama, "Equilibrium Chemical Vapor Deposition Growth of

- Bernal-Stacked Bilayer Graphene\_ ACS Nano **8**, pp.11631-11638 (2014).
- [67] M. E. Schmidt, C. Xu, M. Cooke, H. Mizuta, and H. M. H. Chong, “Metal-free plasma-enhanced chemical vapor deposition of large area nanocrystalline graphene” Mater. Res. Express **1**, 025031 (2014).
- [68] K. Hata, D. N. Futaba, K. Mizuno, T. Namai, N. Yumura, and S. Iijima, “Water-Assisted Highly Efficient Synthesis of Impurity-Free Single-Walled Carbon Nanotubes” Science **306**, pp.1362-1364 (2004).
- [69] S. Yasuda, D. N. Futaba, M. Yumura, S. Iijima, and K. Hata, “Diagnostics and growth control of single-walled carbon nanotube forests using a telecentric optical system for in situ height monitoring” Appl. Phys. Lett. **93**, 143115 (2008).
- [70] R. S. Weatherup, B. C. Bayer, R. Blume, C. Ducati, C. Baetz, R. Schlögl, and S. Hofmann, ”In Situ Characterization of Alloy Catalysts for Low-Temperature Graphene Growth” Nano Lett. **11**, pp.4154-4160 (2011).
- [71] Q. Yu, J. Lian, S. Siriponglert, H. Li, Y. P. Chen, and S. Pei, “Graphene segregated on Ni surfaces and transferred to insulators” Appl. Phys. Lett. **93**, 113103 (2008).
- [72] A. Reina, S. Thiele, X. Jia, S. Bhaviripudi, M. S. Dresselhaus, J. A. Schaefer, and J. Kong, “Growth of large-area single- and Bi-layer graphene by controlled carbon precipitation on polycrystalline Ni surfaces” Nano Res. **2**, pp.509-516 (2009).
- [73] X. Li, W. Cai, J. An, S. Kim, J. Nah, D. Yang, R. Piner, A. Velamakanni, I. Jung, E. Tutuc, S. K. Banerjee, L. Colombo, and R. S. Ruoff, “Large-Area Synthesis of High-Quality and Uniform Graphene Films on Copper Foils” Science **324**, pp.1312-1314 (2009).
- [74] P. R. Kidambi, B. C. Bayer, R. Blume, Z. Wang, C. Baetz, R. S. Weatherup, M. Willinger, R. Schloegl, and S. Hofmann, “Observing Graphene Grow: Catalyst-Graphene Interactions during Scalable Graphene Growth on Polycrystalline Copper” Nano Lett. **13**, pp.4769-4778 (2013).
- [75] E. Sutter, P. Albrecht, and P. Sutter “Graphene growth on polycrystalline Ru thin films” Appl. Phys. Lett. **95**, 133109 (2009).
- [76] P. W. Sutter, J. Flege, and E. A. Sutter “Epitaxial graphene on ruthenium” Nature

- Mater. **7**, pp.406-411 (2008).
- [77] K. S. Kim, Y. Zhao, H. Jang, S. Y. Lee, J. M. Kim, K. S. Kim, J. Ahn, P. Kim, J. Choi, and B. H. Hong, “Large-scale pattern growth of graphene films for stretchable transparent electrodes, Nature **457**, pp.706-710 (2009).
- [78] W. Krätschmer, L. D. Lamb, K. Fostiropoulos, and D. R. Huffman, “Solid C<sub>60</sub>: a new form of carbon” Nature **347**, pp.354-358 (1990).
- [79] Y. Saito, T. Yoshikawa, M. Okuda, N. Fujimoto, K. Sumiyama, K. Suzuki, A. Kasuya, and Y. Nishina. “Carbon nanocapsules encaging metals and carbides” J. Phys. Chem. Solid **54**, pp.1849-1860 (1993).
- [80] X. Zhao, T. Kadoya, T. Ikeda, T. Suzuki, S. Inoue, M. Ohkochi, Y. Takimoto, and Y. Ando, “Development of Fe-doped carbon electrode for mass-producing high-yield single-wall carbon nanotubes” Diamond Relat. Mater. **16**, pp.1101-1105 (2007).
- [81] Y. Guo, T. Okazaki, T. Kadoya, T. Suzuki, and Y. Ando, “Spectroscopic study during single-wall carbon nanotubes production by Ar, H<sub>2</sub>, and H<sub>2</sub>-Ar DC arc discharge” Diamond Relat. Mater. **14**, pp.887-890 (2005).
- [82] C. Kiang, W. A. Goddard III, R. Beyers, J. R. Salem, and D. S. Bethune, “Catalytic Synthesis of Single-Layer Carbon Nanotubes with Wide Range Diameter” J. Phys. Chem. **98**, pp.6612-6618 (1994).
- [83] Y. Saito M. Okuda, N. Fujimoto, T. Yoshikawa, M. Tomita, and T. Hayashi, “Single-Wall Carbon Nanotubes Growing Radially from Ni Fine Particles Formed by Arc Evaporation” Jpn. J. Appl. Phys. **33**, pp.L526-L529 (1994).
- [84] S. Seraphin and D. Zhou, “Single-walled carbon nanotubes produced at high yield by mixed catalysts” Appl. Phys. Lett. **64**, pp.2087-2089 (1994).
- [85] A. Kasuya, Y. Sasaki, Y. Saito, K. Tohji, and Y. Nishina, “Evidence for Size-Dependent Discrete Dispersions in Single-Wall Nanotubes” Phys. Rev. Lett. **78**, pp.4434-4437 (1997).
- [86] A. Huczko, H. Lange, and T. Sogabe, “Influence of Fe and Co-Ni on Carbon Arc Plasma and formation of Fullerenes and Nanotubes” J. Phys. Chem. A **104**, pp.10708-10712 (2000).
- [87] Y. Makita, S. Suzuki, H. Kataura, and Y. Achiba, “Synthesis of single wall carbon

- nanotubes by using arc discharge technique in nitrogen atmosphere” *Eur. Phys. J. D* **34**, pp.287-289 (2005).
- [88] Y. Saito, K. Nishikubo, K. Kawabata, and T. Matsumoto, “Carbon nanocapsules and single-layered nanotubes produced with platinum-group metals (Ru, Rh, Pd, Os, Ir, Pt) by arc discharge” *J. Appl. Phys.* **80**, pp.3062-3067 (1996).
- [89] Y. Saito, Y. Tani, and A. Kasuya, “Diameters of Single-Wall Carbon Nanotubes Depending on Helium Gas Pressure in an Arc Discharge” *J. Phys. Chem. B* **104**, pp.2495-2499 (2000).
- [90] D. Zhou, S. Seraphin, and S. Wang, “Single-walled carbon nanotubes growing radially from  $YC_2$  particles” *Appl. Phys. Lett.* **65**, pp.1593-1595 (1994).
- [91] Y. Saito, M. Okuda, M. Tomita, and T. Hayashi, “Extrusion of single-wall carbon nanotubes via formation of small particles condensed near an arc evaporation source” *Chem. Phys. Lett.* **236**, pp.419-426 (1995).
- [92] C. Journet, W. Maser, P. Bernier, A. Loiseau, M. L. Chapelle, S. Lefrant, P. Deniard, R. Lee, and J. E. Fischer, “Large-scale production of single-walled carbon nanotubes by the electric-arc technique” *Nature* **388**, pp.756-758 (1997).
- [93] Y. Ando, X. Zhao, K. Hirahara, K. Suenaga, S. Bandow, and S. Iijima, “Mass-production of single wall-carbon nanotubes by the arc plasma jet method” *Chem. Phys. Lett.* **323**, pp.580-585 (2000).
- [94] M. I. Mohammad, A. A. Moosa, J. H. Potgieter, and M. K. Ismael, “Carbon Nanotubes Synthesis via Arc Discharge with a Yttria Catalyst” *ISRN Nanomater.* **2013**, 785160 (2013).
- [95] J. C. Bae, Y. J. Yoon, S. Lee, K. M. Song, and H. K. Baik, “Diameter control of single-walled carbon nanotubes by plasma rotating electrode process” *Carbon* **40**, pp.2905-2911 (2002).
- [96] Y. Ando, X. Zhao, K. Hirahara, K. Suenaga, S. Bandow, and S. Iijima, “Arc plasma jet method producing single-wall carbon nanotubes” *Diamond Relat. Mater.* **10**, pp.1185-1189 (2001).
- [97] T. Suzuki, K. Suhama, X. Zhao, S. Inoue, N. Nishikawa, and Y. Ando, “Purification of single-wall carbon nanotubes produced by arc plasma jet method” *Diamond Relat. Mater.* **16**, pp.1116-1120 (2007).

- [98] M. Kanai, A. Koshio, H. Shinohara, T. Mieno, A. Kasuya, Y. Ando, and X. Zhao, “High-yield synthesis of single-walled carbon nanotubes by gravity-free arc discharge” *Appl. Phys. Lett.* **79**, pp.2967-2969 (2001).
- [99] J. Li, M. Kundrapu, A. Shashurin, and M. Keidar, “Emission spectra analysis of arc plasma for synthesis of carbon nanostructures in various magnetic conditions” *J. Appl. Phys.* **112**, 024329 (2012).
- [100] H. Li, L. Guan Z. Shi, and Z. Gu, “Direct Synthesis of High Purity Single-Walled Carbon Nanotube Fibers by Arc Plasma” *J. Phys. Chem. B* **108**, pp.4573-4575 (2004).
- [101] O. Łabędź, H. Lange, A. Huczko, J. Borysiuk, M. Szybowski, and M. Bystrzejewski, “Influence of carbon structure of the anode on the synthesis of single-walled carbon nanotubes in a carbon arc plasma” *Carbon* **47**, pp.2847-2854 (2009).
- [102] M. J. Rahman and T. Mieno, “Production of Single-Walled Carbon Nanotubes by Modified Arc Discharge Method” *Jpn. J. Appl. Phys.* **52**, 056201 (2013).
- [103] E. G. Gamaly and T. W. Ebbesen, “Mechanism of carbon nanotube formation in the arc discharge” *Phys. Rev. B* **52**, pp.2083-2089 (1995).
- [104] J. E. Foster, “Plasma-based water purification: Challenges and prospects for the future” *Phys. Plasmas* **24**, 055501 (2017).
- [105] S. N. Gucker, J. E. Foster, and M. C. Garcia, “An investigation of an underwater steam plasma discharge as alternative to air plasma for water purification” *Plasma Sources Sci. Technol.* **24**, 055005 (2015).
- [106] M. A. Malik, A. Ghaffar, and S. A. Malik, “Water purification by electrical discharges” *Plasma Source Sci. Technol.* **10**, pp.82-91 (2001).
- [107] T. Miyahara, M. Oizumi, T. Nakatani, and T. Sato, “Effect of voltage polarity on oxidation-reduction potential by plasma in water” *AIP Adv.* **4**, 047115 (2014).
- [108] G. R. Stratton, C. L. Bellona, F. Dai, T. M. Holsen, and S. M. Thagard, “Plasma-based water treatment: Conception and application of a new general principle for reactor design” *Chem. Eng. J.* **273**, pp.543-550 (2015).
- [109] T. Morishita, T. Ueno, G. Panomsuwan, J. Hieda, A. Yoshida, M. A. Bratescu, and N. Saito, “Fastest Formation Routes of Nanocarbons in Solution Plasma

- Processes” *Sci. Rep.* **6**, 36880 (2016).
- [110] S. Kim, R. Sergiienko, E. Shibata, Y. Hayasaka, and T. Nakamura, “Production of Graphite Nanosheets by Low-Current Plasma Discharge in Liquid Ethanol” *Mater. Trans.* **51**, pp.1455-1459 (2010).
- [111] J. Kang, O. L. Li, and N. Saito, “Synthesis of structure-controlled carbon nano spheres by solution plasma process” *Carbon* **60**, pp.292-298 (2013).
- [112] O. L. Li, H. Hayashi, T. Ishizaki, and N. Saito, “Enhancement of conductivity in nano carbon balls by the addition of carbon tetrachloride via room temperature solution plasma process” *RSC Adv.* **6**, pp.51864-51870 (2016).
- [113] H. Toyota, S. Nomura, Y. Takahashi, and S. Mukasa, “Submerged synthesis of diamond in liquid alcohol plasma” *Diamond Relat. Mater.* **17**, pp.1902-1904 (2008).
- [114] D. Kim, O. L. Li, and N. Saito, “Enhancement of ORR catalytic activity by multiple heteroatom-doped carbon materials” *Phys. Chem. Chem. Phys.* **17**, pp.407-413 (2015).
- [115] M. Matsushima, M. Noda, T. Yoshida, H. Kato, G. Kalita, T. Kizuki, H. Uchida, M. Umeno, and K. Wakita, “Formation of graphene nano-particle by means of pulsed discharge to ethanol” *J. Appl. Phys.* **113**, 114304 (2013).
- [116] D. Kozak, E. Shibata, A. Iizuka, and T. Nakamura, “Growth of carbon dendrites on cathod above liquid ethanol using surface plasma” *Carbon* **70**, pp.87-94 (2014).
- [117] T. Hagino, H. Kondo, K. Ishikawa, H. Kano, M. Sekine, and M. Hori, “Ultrahigh-Speed Synthesis of Nanographene Using Alcohol In-Liquid Plasma” *Appl. Phys. Express* **5**, 035101 (2012).
- [118] M. Tokushige, A. Matsuura, T. Nishikiori, and Y. Ito, “Formation of Co-Pt Intermetallic Compound Nanoparticles by Plasma-Induced Cathodic Discharge Electrolysis in a Chloride Melt” *J. Electrochem. Soc.* **158**, pp.E21-E26 (2011).
- [119] M. Tokushige, T. Nishikiori, and Y. Ito “Plasma-Induced Cathodic Discharge Electrolysis to Form Various Metal/Alloy Nanoparticles” *Rus. J. Electrochem.* **46**, pp.619-626 (2010).
- [120] M. Ito, M. Hayakawa, S Takashima, E. Asami, T. Aoki, M. Oka, H. Asano, M.

- Kitahara, S. Nakata, K. Yamaguchi, and Y. Murase, "Preparation of Aqueous Dispersion of Titanium Dioxide Nanoparticles using Plasma on Liquid Surface" *Jpn. J. Appl. Phys.* **51**, 116201 (2012).
- [121] P. Muthakarn, N. Sano, T. Charinpanitkul, W. Tanthapanichakoon, and T. Kanki, "Characteristics of Carbon Nanoparticles Synthesized by a Submerged Arc in Alcohols, Alkanes, and Aromatics" *J. Phys. Chem. B* **110**, pp.18299-18306 (2006).
- [122] O. L. Li, J. Kang, K. Urashima, and N. Saito, "Solution Plasma Synthesis Process of Carbon Nano Particles in Organic Solutions" *Int. J. Plasma Environmental Sci. Technol.* **7**, pp.31-36 (2013).
- [123] S. Akiyama, T. Kizu, K. Kamei, and E. Nishikawa, "Molar Concentration Dependence of Sucrose Solution in Carbon Nanotube Synthesis by Liquid-Phase Arc Discharge" *e-J. Surf. Sci. Nanotechnol.* **9**, pp.215-218 (2011).
- [124] T. Charinpanitkul, N. Sano, P. Muthakarn, and W. Tanthapanichakoon, "Enhancing effect of monoolein surfactant on carbon nanoparticles synthesis by arc discharge in liquid" *Mater. Research Bulletin* **44**, pp.324-327 (2009).
- [125] T. Kizu, S. Aikawa, K. Takekoshi, and E. Nishikawa, "Effect of Inrush Current on Carbon Nanotube Synthesis from Xylene by Liquid-Phase Pulsed Arc Method Using Copper Electrodes" *e-J. Surf. Sci. Nanotechnol.* **11**, pp.8-12 (2013).
- [126] N. Sano, O. Kawanami, T. Charinpanitkul, and W. Tanthapanichakoon, "Study on reaction field in arc-in-water to produce carbon nano-materials" *Thin Solid Films* **516**, pp.6694-6698 (2008).
- [127] N. Sano, T. Charinpanitkul, T. Kanki, and W. Tanthapanichakoon, "Controlled synthesis of carbon nanoparticles by arc in water method with forced convective jet" *J. Appl. Phys.* **96**, pp.645-649 (2004).
- [128] J. Suehiro, K. Imasaka, Y. Ohshiro, G. Zhou, M. Hara, and N. Sano "Production of Carbon Nanoparticles Using Pulsed Arc Discharge Triggered by Dielectric Breakdown in Water" *Jpn. J. Appl. Phys.* **42**, pp.L1483-L1485 (2003).
- [129] C. Poonjarernsilp, N. Sano, H. Tamon, and T. Charinpanitkul, "A model of reaction field in gas-injected arc-in-water method to synthesize single-walled carbon nanohorns: Influence of water temperature" *J. Appl. Phys.* **106**, 104315

(2009).

- [130] M. R. Shabgard and A. F. Najafabadi, "The influence of dielectric media on nano-structured tungsten carbide (WC) powder synthesized by electro-discharge process" *Adv. Powder Technol.* **25**, pp.937-945 (2014).
- [131] P. Bruggeman, E. Ribižl, J. Degroote, J. Vierendeels, and C. Leys, "Plasma characteristics and electrical breakdown between metal and water electrodes" *J. Optoelectronics Adv. Mater.* **10**, pp.1964-1967 (2008).
- [132] H. Lee, M. A. Bratescu, T. Ueno, and N. Saito, "Solution plasma exfoliation of graphene flakes from graphite electrodes" *Royal Soc. Chem. Adv.* **4**, pp.51758-51765 (2014).
- [133] S. S. Harilal, A. Hassanein, and M. Polek, "Late-time particle emission from laser produced graphite plasma" *J. Appl. Phys.* **100**, 053301 (2011).
- [134] T. Ikegami, F. Nakanishi, M. Uchiyama, and K. Ebihara, "Optical measurement in CNTs formation by pulsed laser ablation" *Thin Solid Films*, **457**, pp.7-11 (2004).
- [135] H. Geng, K. Kim, K. So, Y. Lee, Y. Chang, and Y. Lee, "Effect of Scid Treatment on Carbon Nanotube-Based Flexible Transparent Conducting Films" *J. Am. Chem. Soc.* **129**, pp.7758-7759 (2007).
- [136] J. Lagemaat, T. M. Barnes, G. Rumbles, S. E. Shaheen, and T. J. Coutts, "Organic solar cells with CNTs replacing  $\text{In}_2\text{O}_3:\text{Sn}$  as the transparent electrode" *Appl. Phys. Lett.* **88**, 233503 (2006).

## **Chapter 2. Measurement techniques of plasmas and evaluation methods of synthesized carbon nanomaterials and by-products**

### 2.1 Experimental methods

#### 2.1.1 Arc plasma for SWNTs synthesis

The arc plasma setup in this study used was typical horizontally opposed configuration. Figure 2.1 shows the experimental setup and conditions for SWNTs synthesis by the arc plasma with optical diagnostics. The chamber was made of stainless steel (SUS) with 200 mm diameter and 400 mm height. The quartz windows for optical measurement were installed to the chamber. The anode electrode was configured of carbon (C), nickel (Ni), and yttrium (Y) with 6 mm diameter and 100 mm length. The composition ratio of anode was C:94.8 %, Ni:4.2 %, and Y:1.0 %. This composition ratio was reported as the ratio which caused a drastic increase in the yield of SWNTs [1]. These substances were dispersed uniformly in the anode. The anode was produced by Toyo Tanso Co.,Ltd. The cathode was 99.99 % carbon rod with 10 mm diameter and 100 mm length (Nilaco C-072651). The electrodes were fixed by dedicated holders made of SUS and the anode side could be move to adjust position of the anode. The chamber was evacuated below 5 Pa and then pure helium (He) gas was introduced. The arc plasma was ignited by applying a large DC current from a welding power source (Panasonic YC-300BZ3). Applied current had two steps. Firstly, the initial current was applied at 20 A. In this step, the electrodes gap distance was approximately 3 mm. This step was necessary to create the plasma seed fire. When the plasma was generated, the applied DC current increased. The electrode gap distance was increased by the electrode distance

adjuster on the anode side at this time. The electrode gap distance can be monitored as the potential between the anode and the cathode. In this study, a voltage was set at 24 V which was the gap distance at an approximately 20 mm.

The vaporized carbon electrode with Ni and Y spread into the chamber with heat convection and reached chamber wall (chamber soot) or top edge of the cathode (cathode deposit). The chamber soot includes SWNTs and the cathode deposit includes MWNTs. Chamber soot was collected and analyzed by Raman scattering spectroscopy (Kaiser Raman RXN Systems) and transmission electron microscope (TEM) (Hitachi H-7000).

OES was carried out by a multichannel spectrometer (Ocean Optics HR-4000). The emitted light from arc plasma was collected by lenses and introduced to spectrometer using optical fiber. The focus point of objective lens was set at 50 mm above of the gap of the electrodes. The arc plasma is extended to upward by thermal convection and generated chemical species are also moved by this stream.

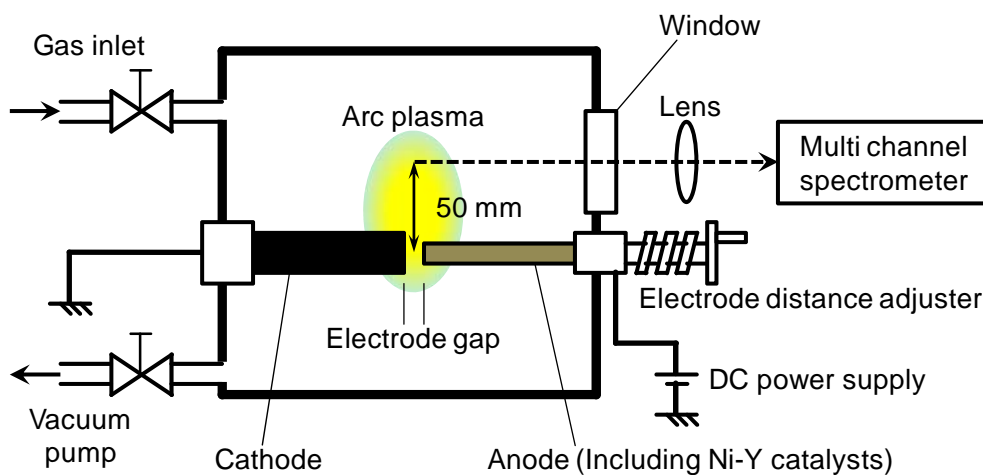


Figure 2.1. Experimental setup for measurements and SWNTs synthesis by arc plasma.

### 2.1.2 Characteristics of arc plasma for SWNTs synthesis

DC arc discharge for SWNTs synthesis evaporates the anode electrode. The cathode electrode is not evaporated. The anode evaporation is induced by electrons collisions. The properties of arc plasma during SWNTs synthesis are described below.

The anode was evaporated during the discharge. This was caused by electron collisions. The physical characteristics of the arc plasma in synthesis of CNTs were discussed by Gamaly and Ebbesen [2]. The special distribution of space charge, electric field, and potential between electrodes of arc plasma is shown in Fig. 2.2. In the vicinity of the surface of the cathode, the positive space charge exists at the high density. Therefore, the potential drops sharply in the very thin region on the front face of the cathode. The thickness of this space charge layer (denoted  $\Delta$  in cm) is about the mean free path of ions and electrons.  $\Delta$  can be estimated from the Child-Langmuir equation for the ionic current density (denoted  $j_{\text{ion}}$  in A/cm<sup>2</sup>),

$$j_{\text{ion}} = \frac{4\varepsilon_0}{9} \sqrt{\frac{2e}{M_{\text{Ci}}}} \frac{V^{3/2}}{\Delta^2} = 5.46 \times 10^{-8} \frac{V^{3/2}}{\Delta^2 M_{\text{Ci}}^{1/2}} \quad [\text{A/cm}^2], \quad (2.1)$$

where  $e$  is elementary charge in C,  $M_{\text{Ci}}$  is mass number of carbon ion,  $V$  voltage drop of cathode in V,  $\varepsilon_0$  is permittivity of free space in F/m. At cathode layer, the  $j_{\text{ion}}$  has the following relation with the electron current density (denoted  $j_e$  in A/cm<sup>2</sup>),

$$j_{\text{ion}} = j_e \sqrt{\frac{m_e}{M_{\text{Ci}}}} = j_e \times 8.2 \times 10^{-3} \quad [\text{A/cm}^2], \quad (2.2)$$

where  $m_e$  is electron mass in kg. In the case of  $V = 20$  [V] and  $j_e = 240$  [A/cm<sup>2</sup>], thickness of the space charge layer is calculated as  $\Delta = 8.29 \times 10^{-4}$  [cm] from Eqs. (2.1) and (2.2). This space charge layer is also a region where a large part of the inter-electrode voltage is applied (10 V in about half). Therefore, the electric field

(denoted  $E$  in V/cm) in this cathode layer is  $1.21 \times 10^4$  V/cm on average. Outside of the cathode layer,  $E$  is several orders of magnitude smaller.

The gas between the electrodes is mixed gas configured from process gas, carbon ions, and neutral carbon species. When He is used as the process gas, He is not ionized because the first ionization energy of He is 24.87 eV, while the kinetic energy of electrons in the arc plasma is at most 20 eV.

Assuming that the ionic current plays a major part of the total current, it becomes an electrically neutral region away from the vicinity of the cathode surface, and the carbon ion density (denoted  $n_{\text{ion}}$  in  $\text{cm}^{-3}$ ) can be obtained using following equation,

$$j_e \approx j_{\text{ion}} = en_{\text{ion}}v_{\text{ion}} = en_{\text{ion}}v_{\text{th}} \quad [\text{A}/\text{cm}^2], \quad (2.3)$$

where  $v_{\text{ion}}$  is carbon ion diffusion velocity in cm/s and  $v_{\text{th}}$  thermal speed of carbon atoms in cm/s.

The anode is collided by electrons; on the other hand, the cathode ejects electrons and is collided by ions. Most of the impact energy of these charge particles turns into heat. From the Eq. (2.2), the ion current density near the cathode surface is two orders of magnitude smaller than the electron current density. That is, the energy injected into the anode surface, and the anode is heated to higher temperature compared with the cathode. Furthermore, if the field emission of electrons occurs at the surface of the cathode, a cooling effect due to the release of kinetic energy by emitted electrons may occur. As a result, the cathode becomes lower in temperature than the anode, and the carbon vapor diffuses from the anode to the cathode side.

The electrical power density (denoted  $Q$  in W) supplied to the arc plasma due to joule loss is given by following equation,

$$Q = jE \quad [\text{W}]. \quad (2.4)$$

The heat of the arc plasma is lost due to the thermal conduction to electrodes and He gas, thermal radiation loss, and evaporation of the anode. Therefore, in the steady state, the energy supplied to the arc plasma and the energy dissipating are balanced as following,

$$Q\pi r_0^2 d = 2\left(a_c \frac{dT}{dz}\right)\pi r_0^2 + \left(a_{\text{He}} \frac{dT}{dr}\right)2\pi r_0 d + Q_{\text{rad}} 2\pi r_0 d + Q_{\text{sub}} r_{\text{sub}}, \quad (2.5)$$

where  $r_0$  is diameter of the electrode in cm,  $a_c$  and  $a_{\text{He}}$  are thermal conductivity of the carbon electrode and the He gas in  $\text{W}/(\text{cm} \cdot \text{K})$ , respectively,  $Q_{\text{rad}}$  is thermal radiation intensity of Stefan-Boltzmann ( $\sigma T^4 = 5.67 \times 10^{-12} T^4$  [ $\text{J}/\text{cm}^2 \cdot \text{s} \cdot \text{K}^4$ ]),  $Q_{\text{sub}}$  is sublimation energy of carbon ( $7.4 \text{ eV} = 1.22 \times 10^{-18}$  [J]),  $r_{\text{rad}}$  is the number of evaporated carbon atoms from the anode in unit time.

The thermal conductivity of the carbon electrode differs depending on the material, but when a value for graphite is used, it is  $a_c \cong 2$  [ $\text{W}/(\text{cm} \cdot \text{K})$ ] at 2000 K and the temperature gradient of the electrode is  $dT/dz \cong 0.3 \times 10^3$  [ $\text{K}/\text{cm}$ ]. On the other hand, He gas is  $a_{\text{He}} = 1.06 \times 10^{-2}$  [ $\text{W}/(\text{cm} \cdot \text{K})$ ] at 4000 K and it is hardly dependent on pressure in the range of several hundred Pa to several MPa. The temperature gradient in the direction perpendicular to the arc plasma column is  $dT/dr \cong 2 \times 10^3$  [ $\text{K}/\text{cm}$ ]. The cross section through which heat is transmitted is  $2\pi r_0^2 \cong 1$  [ $\text{cm}^2$ ] in the electrode direction,  $2\pi r_0 d \cong 0.3$  [ $\text{cm}^2$ ] in the diameter direction. Therefore, in loss at the thermal conduction, the thermal conduction to He gas (approximately 6 W) is negligible compared to the conduction to the electrode (approximately 600 W). Thermal radiation is a loss as much as thermal conduction to the electrode. At 400 K,  $Q_{\text{rad}} = \sigma T^4 = 1.45 \times 10^3$  [ $\text{J}/(\text{cm}^2 \cdot \text{s})$ ], and if this is multiplied by the radiation area ( $2\pi r_0 d \cong 0.3$  [ $\text{cm}^2$ ]), the loss is approximately 400 W. The heat loss due to evaporation of carbon can be estimated to be approximately 70 W, assuming

$r_{\text{sub}} = 6.3 \times 10^{19}$  [carbon atoms/s], this is not too large. Therefore, most of the heat generated by the arc plasma is lost by thermal conduction to the electrode and thermal radiation.

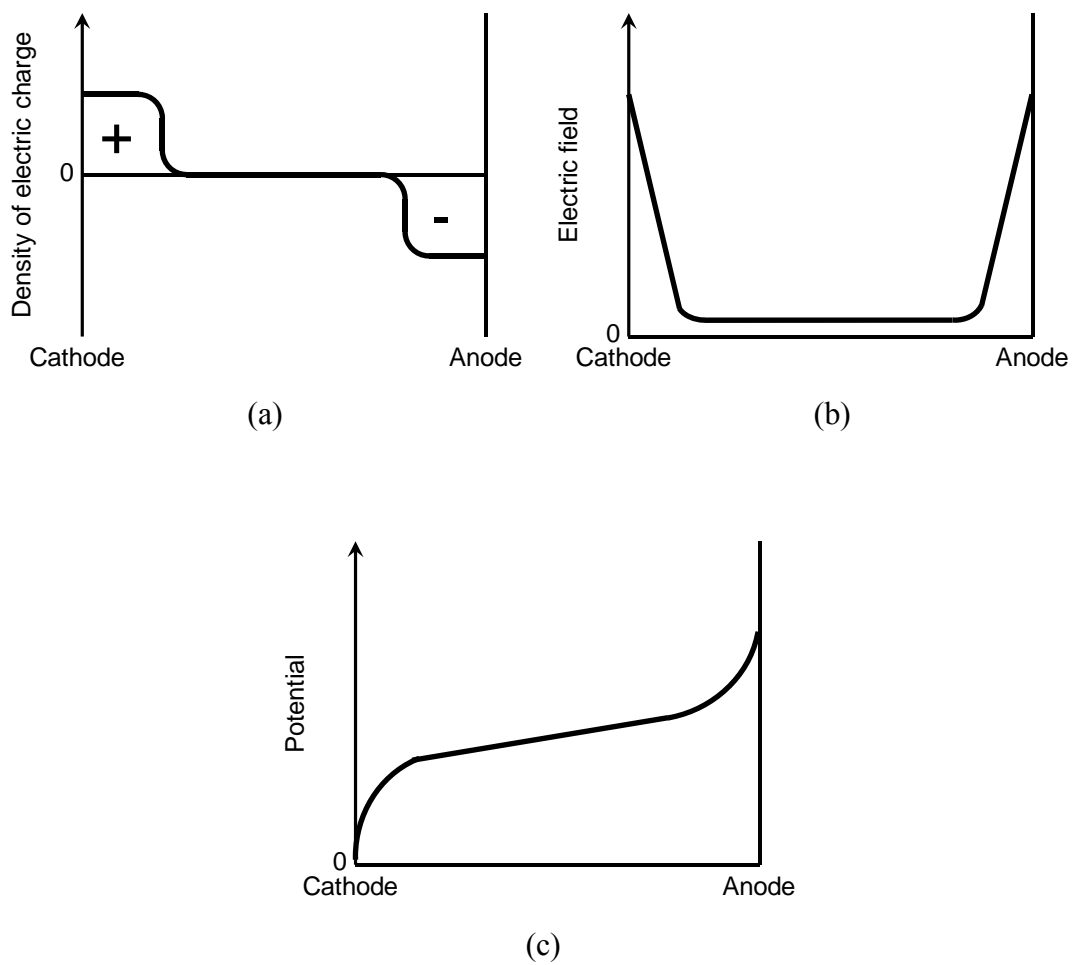


Figure 2.2. Schematic diagrams of (a) spatial charge, (b) electric field, and (c) potential of arc plasma.

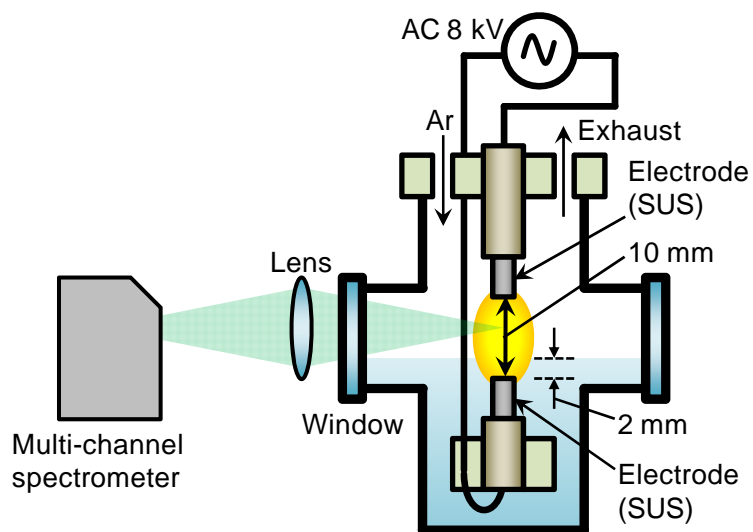
### 2.1.3 In-liquid plasma for nanographene synthesis

The in-liquid plasma experimental setup is shown in Fig. 2.3. The configuration was similar to the previous study of ref. [3] except for the submerged electrode. In this study, electrodes configuration was arranged to be employed perpendicular opposed electrodes. This electrodes configuration can relatively stabilize the plasma position. The chamber was made of glass with 30 mm depth and 80 mm width. The optical window ports were equipped at the side wall. The top of chamber was shielded by the cap made of polytetrafluoroethylene with electrodes holders, gas inlet, and outlet ports. The electrodes were made of SUS. This apparatus doesn't need any vacuum systems. The employed liquids were weighed on a scale using measuring cylinder at 150 ml and introduced to chamber. And then, the air inside the chamber was replaced by argon (Ar) flow at 3 slm. The in-liquid plasma was generated by applying boosted and modulated commercial power shown in Fig. 2.3(b). The Fig. 2.3(b) shows the waveform of the applied voltage at which discharge does not occur, and is applied up to  $V_{p-p} = 8$  [kV] at the discharge. The plasma was ignited when the applying voltage reached breakdown point. The waveform of voltage and current are shown in Fig. 2.4(c). The waveforms were measured at the ethanol used. The ignition points and durations of plasma varied every time due to liquid condition (liquid surface waves, bubbles in liquids). The plasma duration times were almost 4 to 5 ms in 8.3 ms of single cycle. For OES, acquire point and time length is important. The state of the actual in-plasma is shown in Fig. 2.4.

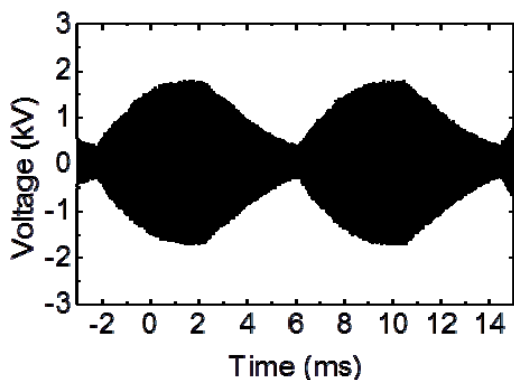
After the synthesis, the samples were filtered using 1- $\mu$ m-pore-size filters (Merck Omnipore JAWP04700) to be divided into solid products and residual liquids. The obtained solid products were treated by 30 %  $H_2O_2$  water at 120°C on 120 min to defecate non-crystalline structures. The  $H_2O_2$  has a function to remove amorphous

carbons. Synthesized and defecated samples were analyzed by TEM (JEOL JEM2010) and Raman scattering spectroscopy (Renishaw inVia Reflex 532 nm of excitation). The residual liquids were analyzed by gas chromatography-mass spectrometry (GC-MS) (Hewlett-Packard HP6870 Series GC System with Agilent Technology J&W GC column - DB-WAX 122-7032 0.25 mm diameter connected to 5973 Mass Selective Detector).

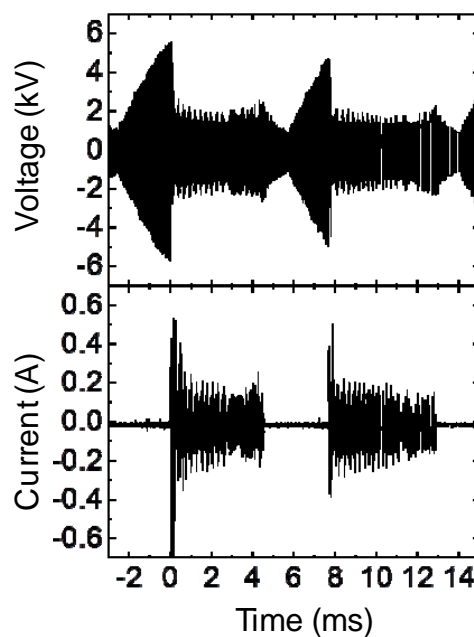
The OES was carried out using a multichannel spectrometer (Ocean Optics HR-4000) and a high-resolution spectrometer (Andor Shamrock 500) with a fast-gated intensified charge-coupled device image sensor (Andor iStar 334T). The plasma emission light at the gas phase was collected using lenses and introduced to the spectrometer by an optical fiber.



(a)



(b)



(c)

Figure 2.3. Experimental setup for nanographene synthesis by in-liquid plasma and measurements. (a) Synthesis chamber and OES setup. (b) Applied voltage. (c) Discharge waveform of voltage and current.

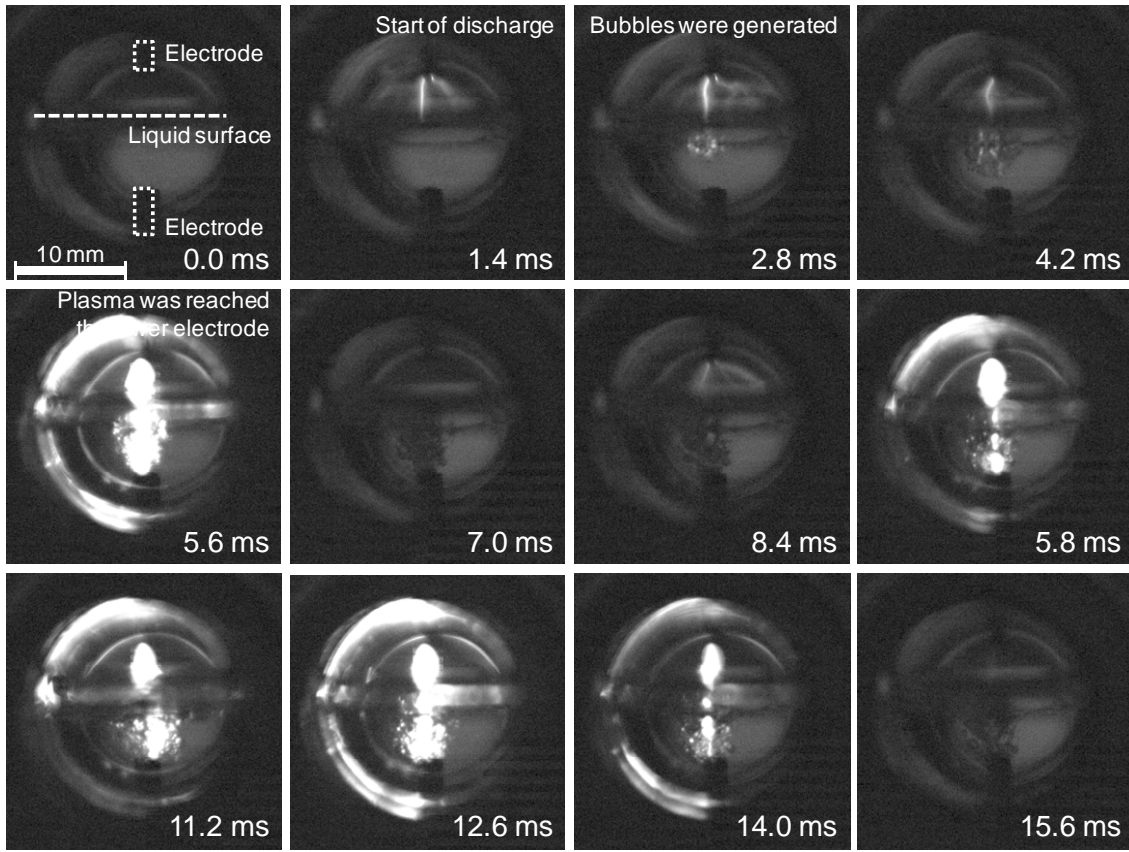


Figure 2.4. Examples of in-liquid plasma formation observed by high-speed camera.

## 2.2 Optical emission spectroscopy (OES)

The emissions from plasma have much information about the active species. These energies can be observed as line spectra having spreads corresponding to the resolution of the detector by spectroscopic analysis. The emission line is unique to each atomic or molecule, and it is possible to identify the luminescent species. The molecular emission lines reflect electron energy, vibrational energy, and rotational energy of the molecule. The state of molecule can be estimated from emission lines. Emission of the molecule and spectrometer are described below.

When the energy is externally applied to atoms or molecules, electrons may transition from a normal energy level to a higher energy level. Although this is a phenomenon generally called excitation, since the excited state is in an unstable state, it releases energy in order to return to a stable state. The energy at this time is emitted as light energy, which is spectrally separated by a diffraction grating and detected by light sensor. Since the emitted light shows wavelengths inherent to atoms and molecules, substances can be identified by examining the line spectrum of the emitted light. The temperature and density of these chemical species can also be determined, but this is excited species of the upper level, not the species before the electron collision excitation. Generally, the line intensity of the radiation transition of a molecule is given by,

$$I(n', v', J' \rightarrow n'', v'', J'') = h\nu A(n', v', J' \rightarrow n'', v'', J'') N_{n', v', J'}, \quad (2.6)$$

where  $I(n', v', J' \rightarrow n'', v'', J'')$  is radiant flux accompanying the transition of inside the bracket,  $n, v, j$  in bracket are electronic state quantum number, vibrational quantum, rotational quantum number, respectively,  $h$  is Plank constant,  $\nu$  is emission line frequency,  $A$  is transition probability,  $N_{n', v', J'}$  is number density of upper state of transition. Assuming level density distribution of vibration and rotation follows the

Boltzmann distribution of vibrational temperature (denoted  $T_v$  in K) and rotational temperature (denoted  $T_r$  in K), it is possible to rewrite the upper level density of transition as,

$$N_{n',v',J'} = N_{n'} \exp\left(-\frac{E_{v'}}{k_B T_v}\right) (2J'+1) \exp\left(-\frac{E_{J'}}{k_B T_r}\right), \quad (2.7)$$

where  $N_{n'}$  is constant independent of  $v$  and  $J$ ,  $E_v$  and  $E_J$  are energy levels at the vibrational level  $v$  and rotational level  $J$  in  $\text{cm}^{-1}$ , and  $k_B$  is Boltzmann constant.  $A$  can be rewritten as,

$$A(n', v', J' \rightarrow n'', v'', J'') = \frac{64\pi^4 \nu_0^3}{3hc^3 g_{n'}} \cdot \frac{1}{2J'+1} |\bar{R}|^2 q_{v',v''} S_{J'J''}, \quad (2.8)$$

where  $\nu_0$  is center of frequency in Hz,  $|\bar{R}|^2$  is transition dipole moment,  $g_{n'}$  is statistical mass ratio of electronic state  $n'$ ,  $q_{v',v''}$  is Franck-Condon factor, and  $S_{J'J''}$  is Hönl-London factor. By substituting Eqs. (2.7) and (2.8) into Eq. (2.6) and rearranging it, the emission intensity  $I(n', v', J' \rightarrow n'', v'', J'')$  can be described as being proportional to product of vibrational intensity  $I_{v',v''}$  and rotational intensity  $I_{J'J''}$ .

$$I(n', v', J' \rightarrow n'', v'', J'') = K_n I_{v',v''} I_{J'J''}, \quad (2.9)$$

where  $K_n$  is constant independent of upper and lower state vibrational and rotational quantum numbers. The intensity terms of vibration and rotation are described as,

$$I_{v',v''} = q_{v',v''} \nu^4 \exp(-E_{v'}/k_B T_v). \quad (2.10)$$

$$I_{J'J''} = S_{J'J''} \exp(-E_{J'}/k_B T_r). \quad (2.11)$$

If the respective electronic, vibrational, and rotational frequencies of upper and lower levels are specified, the emission intensity emitted by transition is theoretically calculated as a function of  $T_v$  and  $T_r$ . However, actually radiated photons have spreading

distribution on wavelength, and those superimposed are observed as spectra. Wavelength of emission lines are calculated from energy differences between upper and lower levels related to transition. The energy level  $E(n, \nu, J)$  of molecule is expressed as the sum of the energies  $E_n$ ,  $E_\nu$ , and  $E_J$ , of the energy levels of the electronic state  $n$ , vibrational level  $\nu$ , and rotational level  $J$  as,

$$E(n, \nu, J) = E_n + E_\nu + E_J. \quad (2.12)$$

Using spectroscopically determined constant, vibrational energy and rotational energy can be obtained as,

$$E_\nu = \omega_e(\nu + 1/2) - x_e\omega_e(\nu + 1/2)^2 + \dots, \quad (2.13)$$

$$E_J = B_\nu J(J + 1) - D_e J^2(J + 1)^2 + \dots, \quad (2.14)$$

where,  $\omega_e$  is vibrational energy in  $\text{cm}^{-1}$ ,  $x_e\omega_e$  is anharmonic term in  $\text{cm}^{-1}$ ,  $B_\nu$  is rotational constant at  $\nu$  level in  $\text{cm}^{-1}$ ,  $D_e$  is energy to dissociation limit in  $\text{cm}^{-1}$ .  $B_\nu$  is described as,

$$B_\nu = B_e - \alpha_e(\nu + 1/2) + \dots, \quad (2.15)$$

where  $B_e$  is rotational constant at equilibrium internuclear distance in  $\text{cm}^{-1}$  and  $\alpha_e$  is constant depending on anharmonicity of vibration in  $\text{cm}^{-1}$ . These constants are already required for several molecular gas excited states and can be used. By applying Eq. (2.12), the energies of the upper level and the lower level are obtained, and the center wavelength of the emission line is determined from the difference. Therefore, the emission appears with spread defined by the device function for the wavelength with the intensity calculated by equation as,

$$I(n', \nu', J' \rightarrow n'', \nu'', J'') = K_n q_{\nu'\nu''} S_{J'J''} V_0^4 \exp\left(-\frac{E_{\nu'}}{k_B T_\nu}\right) \exp\left(-\frac{E_{J'}}{k_B T_r}\right). \quad (2.16)$$

It is possible to theoretically obtain the band spectrum that can actually be measured if this is properly summed with respect to excited vibrational and rotational state.

Spectrometer is constructed from entrance slit, focus elements, grating, and detector. Figure 2.5 shows schematic diagram of Czerny-Turner type multichannel spectrometer. The light passing through the entrance slit is made parallel by parabolic mirror, separated by a diffraction grating, and focused on image intensified charge-coupled device (ICCD). The grating is provided with sawtooth-like grooves as shown in Fig 2.6, and diffraction efficiency in a specific direction is increased. When light enters grating with incident angle  $\alpha$ , the diffraction occurs in the direction of angle  $\beta$  as,

$$\sin \beta = -\sin \alpha + \frac{m\lambda}{d}, \quad (2.17)$$

where  $m$  is degree ( $= 0, \pm 1, \pm 2, \dots$ ),  $\lambda$  is wavelength, and  $d$  is groove pitch. Zero-order diffracted light ( $m = 0$ ) propagates in  $\beta = \alpha$  direction and there is no disperse. The higher order diffracted light differs in diffraction direction by  $\lambda$ . Dispersion performance is obtained by differentiating Eq. (2.17) as,

$$D_\lambda = \frac{\partial \beta}{\partial \lambda} = \frac{m}{d \cos \beta}. \quad (2.18)$$

Therefore, dispersion increases as  $d$  decrease,  $m$  increase. An ordinary grating for spectroscopy is composed of several hundreds to several thousands of grooves per mm.

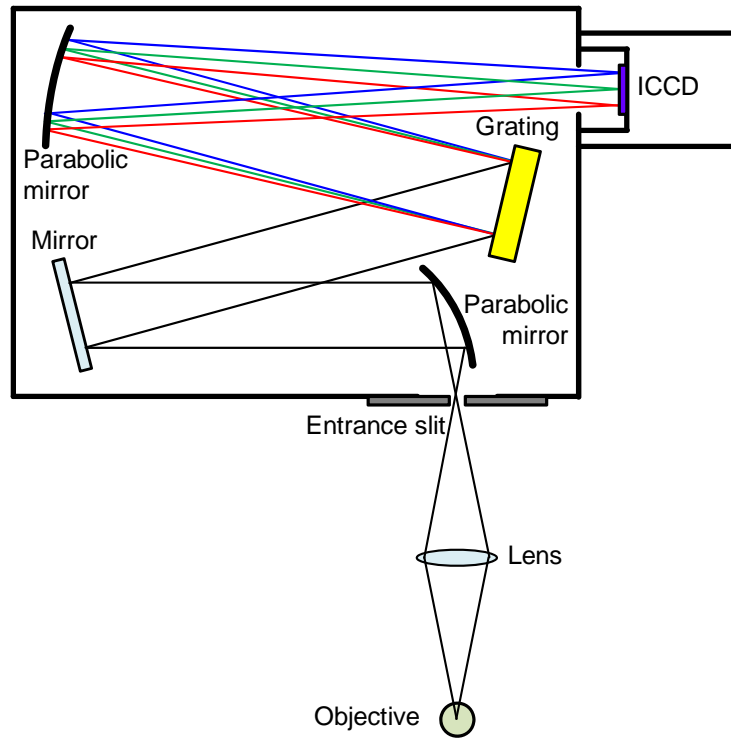


Figure 2.5. Schematic of Czerny-Turner multichannel spectrometer.

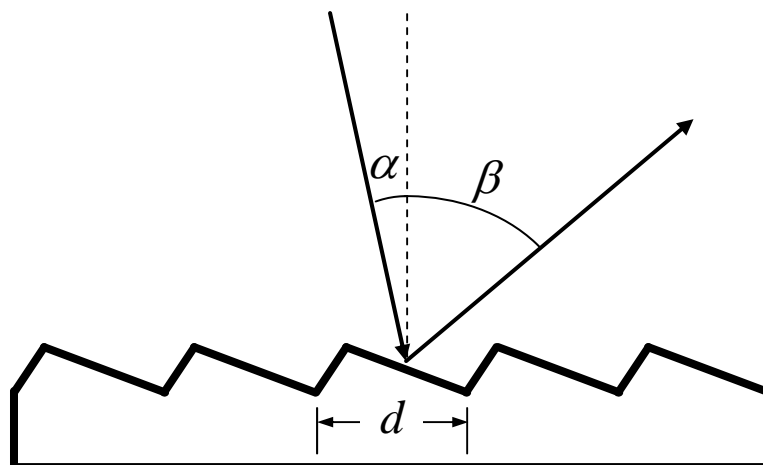


Figure 2.6. Diffraction on grating.

### 2.3 Raman scattering spectroscopy of carbon nanomaterials

Raman scattering is a phenomenon that occurs by vibrating motion of molecules, crystal and light. When the incident light is irradiated on a substance, the molecule obtains the energy by the energy of incident light. The molecule is excited from the initial state to the virtual level, and immediately releases energy as light and returns to the lower level. In many cases, this initial state and the final state are at the same level, and the light emitted at that time is called Rayleigh light. On the other hand, the final state may be higher or lower in energy level than the initial state, and light scattered at this time is called Stokes light, Anti-Stokes light, respectively. The intensity of scattered light is proportional to the number of starting states that exchange energy with incident light. Since the probability that a molecule takes a state of a certain energy level follows the Boltzmann distribution, it is more likely to take a lower energy level. Therefore, the probability of occurrence of Stokes scattering that transitions from a low energy state to a high energy state is higher than that of Anti-Stokes scattering that transitions from a high energy state to a low energy state, and hence the scattering intensity becomes stronger. In the measurement of Raman scattering, usually Stokes scattered light is measured.

Characteristic peaks derived from lattice vibrations appear in the Raman scattering spectra of graphene and SWNTs. There are two carbon atoms in the first Brillouin zone (FBZ) of graphene and there are six degrees of freedom of oscillation. Given the translational symmetry of graphene, there is a dispersion relation of energy of six phonons corresponding to the degree of freedom of vibration. 3 of 6 phonon dispersion relationships are acoustic mode (A) and 3 are optical mode (O). The acoustic mode is a mode in which 2 carbon atoms in the unit cell oscillate in the same direction, and the acoustic mode oscillates in the opposite direction. For each mode, 1 is

longitudinal wave (L) and 2 are transverse waves (T). The longitudinal wave is a wave oscillating at right angles to the vibrational direction (wave vector  $q$ ) and the transverse wave is a wave oscillating in parallel. Therefore, there are LA, LO, two TA, two TO modes. Furthermore, there are two kinds of vibrational directions parallel to the atomic layer (in-plane: i) and vertical (out-of-plane: o). Since the direction in which the vibration of graphene proceeds is limited to the layer direction, the LA and LO modes are in-plane vibrations (in this case, not iLA, iLO). TA and TO modes have an in-plane and an out-of-plane, denoted iTA, oTA, iTA, oTA. The vibrational modes of graphene are summarized in Table 2.1. The iTA mode of graphene is  $1585 \text{ cm}^{-1}$ . The oTA mode is  $850 \text{ cm}^{-1}$ . The 2D-band appearing around  $2700 \text{ cm}^{-1}$  is a double resonance Raman scattering spectroscopic signal of two K point phonons. The number of layers of graphene can be evaluated from the intensity ratio of G-band and 2D-band. In the case of monolayer graphene, the intensity of the 2D-band is larger than that of the G-band. As the number of layers increase, the full width-half maximum of 2D-band ( $\text{FWHM}_{2D}$ ) expands and the relative intensity decreases.

In the case of SWNTs, the lattice vibration is given as a function of one-dimensional wave number by circumferential periodic boundary condition. The one-dimensional wave number  $k = 2\pi/\lambda$  is quantized to an integral multiple of  $2/d_t$  since the wave number of the circumferential direction waves becomes  $1/n$  ( $0 \leq n \leq N - 1$ ) of  $\pi d_t$ . Here  $N = 2(n^2 + nm + m^2)/d_r$  ( $d_r$  is the greatest common divisor between  $(2n + m)$  and  $(2m + n)$ ). If the cycle in the axial direction of the CNTs is  $T$ , the wave number is a line segment of  $-\pi/T < k < \pi/T$  (cutting line, see section 1.1.2). Therefore, in the phonon modes of CNTs,  $3N$  one-dimensional phonon dispersion relation is obtained for  $k$  obtained by cutting the two-dimensional wave number space

of graphene on the cutting line.  $3N - 4$  are optical phonon modes and 4 are acoustic phonon modes.

Radial breathing mode (RBM) corresponds to vibration in the diameter direction of the SWNTs. This mode corresponds to the out-of-plane vibration of graphene. When the diameter gets larger by rolling the graphene sheet into a cylindrical shape, the tension is generated between the C-C bonds, and the restoring force works to enter the optical mode. The wave number of RBM is inversely proportional to the SWNTs diameter. There are several equations to calculate diameter [4-7]. In this study, the equation that takes into consideration that the synthesized SWNTs are bundled was used [7],

$$d_t = \frac{232}{\omega - 6.5} \quad [\text{nm}], \quad (2.19)$$

where  $\omega$  is the RBM Raman shift in  $\text{cm}^{-1}$ .

The energy of iTO and LO modes of graphene degenerate. Degenerate iTO and LO modes give a signal due to six-membered ring structure of graphene called G-band ( $1590 \text{ cm}^{-1}$ ). In the case of CNTs, the degeneracy is broken down and G-band splits into  $G^+$  and  $G^-$ -band [8,9]. Since the LO mode propagates as a wave oscillating in the tube axial direction, there is no frequency dependence on the tube diameter. On the other hand, it is shifted to the low energy region in inverse proportion to the square of the tube diameter because the iTO mode vibrates diametrically. This is because the CNTs has a cylindrical shape and has a curvature, so the spring constant between C-C bonds becomes smaller as the curvature increase. A. Kasuya et al. analyzed the SWNTs with different diameters synthesized using different catalysts by Raman scattering spectroscopy and showed that the Raman shifts of  $G^+$ - and  $G^-$ -bands follow phonon dispersion relation [10].

There are D-band ( $1350 \text{ cm}^{-1}$ ) and D'-band ( $1610 \text{ cm}^{-1}$ ) due to structural defects

of CNTs. D-band appears by double resonance effect with inelastic scattering due to defect structure [11].

The ratio between G-band and D-band (G/D ratio or D/G ratio) is widely used as an index showing the crystallinity of carbon nanomaterials. In the case of nanographene, domain size (denoted  $L_a$  in nm) can be calculated from peak intensity area ratio as,

$$L_a = \frac{560}{E_1^4} \left( \frac{I_D}{I_G} \right)^{-1} \quad [\text{nm}], \quad (2.20)$$

where  $E_1$  is laser energy using excitation in eV unit,  $I_D$  and  $I_G$  are integrated intensities of D- and G-band [12].

Table 2.1. Vibrational modes of graphene.

Vibrational mode	Longitudinal wave	Transverse wave	
Vibrational direction	in-plane		out-of-plane
Acoustic mode	LA	iTA	oTA
Optical mode	LO	iTO	oTO

## 2.4 Gas chromatography-mass spectrometry (GC-MS)

The residual liquid after filtration included by-products and intermediates. These substances were generated from the employed liquid by in-liquid plasma. These substances provide important information to follow the reaction process in the in-liquid plasma.

The gas chromatography-mass spectrometry (GC-MS) system enables us to evaluate molecules. Figure 2.7 shows the schematic diagram of GC-MS. The GC is configured from the sample injection part and column part. Injected sample is gasified and introduced column. Gasified sample is separated into molecules by differences of interactions between molecules and column materials. Therefore, the time it takes to pass through a column varies from molecules to molecules. A chromatograph is obtained with this time as a retention time. MS part is configured from ionization part, magnet, and detector. The molecules passed through the GC are ionized. Ionized molecules are accelerated and enter the magnet. At the magnet section, ions are separated into mass to charge ratio ( $m/z$ ) dependent on magnetic interference and detected. Based on the obtained retention time and  $m/z$ , the mass spectrum is searched from database to identify the substance.

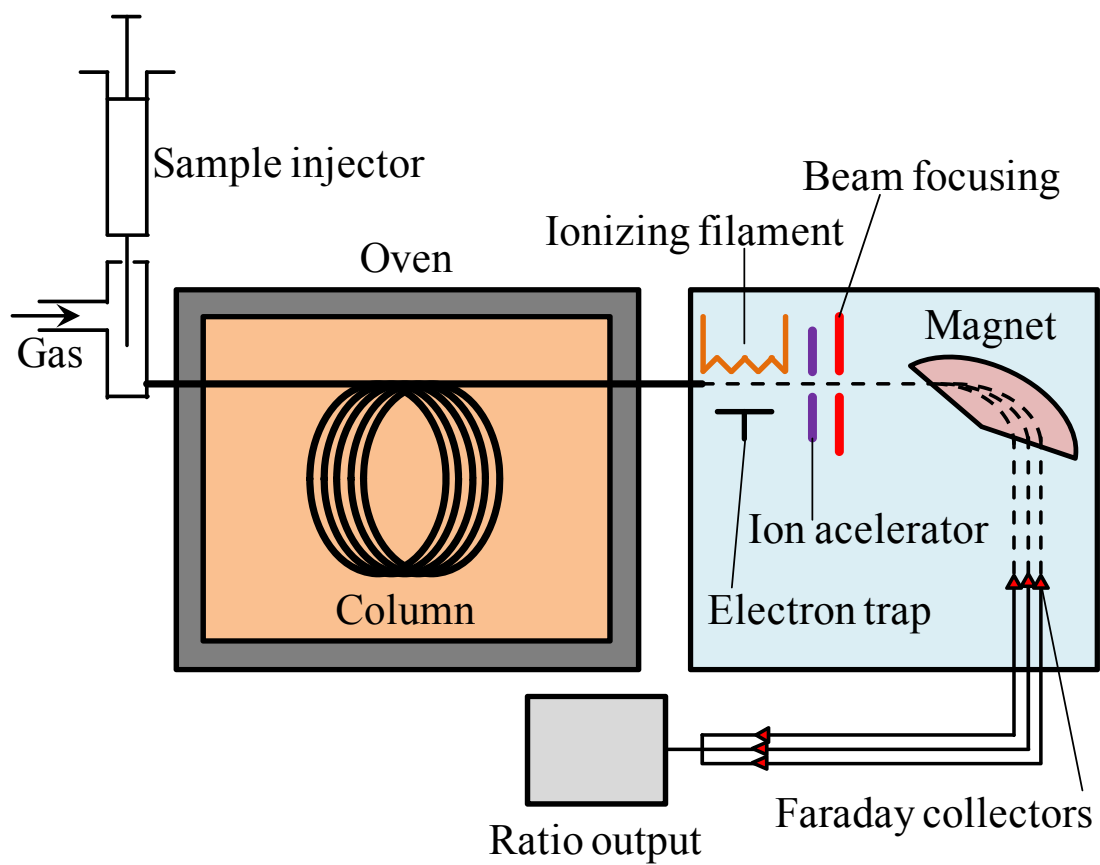


Figure 2.7. Schematic diagram of GC-MS.

## References

- [1] C. Journet, W. Maser, P. Bernier, A. Loiseau, M. L. Chapelle, S. Lefrant, P. Deniard, R. Lee, and J. E. Fischer, "Large-scale production of single-walled carbon nanotubes by the electric-arc technique" *Nature* **388**, pp.756-758 (1997).
- [2] E. G. Gamaly and T. W. Ebbesen, "Mechanism of carbon nanotube formation in the arc discharge" *Phys. Rev. B* **52**, pp.2083-2089 (1995).
- [3] T. Hagino, H. Kondo, K. Ishikawa, H. Kano, M. Sekine, and M. Hori, "Ultrahigh-Speed Synthesis of Nanographene Using Alcohol In-Liquid Plasma" *Appl. Phys. Express* **5**, 035101 (2012).
- [4] A. Jorio, R. Saito, J. H. Hafner, C. M. Lieber, M. Hunter, T. McClure, G. Dresselhaus, and M. S. Dresselhaus, "Structural ( $n,m$ ) Determination of Isolated Single-Wall carbon Nanotubes by Resonant Raman Scattering" *Phys. Rev. Lett.* **86**, pp.1118-1121 (2001).
- [5] S. Bandow, S. Asaka, Y. Saito, A. M. Rao, L. Grigorian, E. Richter, and P. C. Eklund "Effect of Growth Temperature on the Diameter Distribution and Chirality of Single-Wall Carbon Nanotubes" *Phys. Rev. Lett.* **80**, pp.3779-3782 (1998).
- [6] S. M. Bachilo, M. S. Strano, C. Kittrell, R. H. Hauge, R. E. Smalley, and R. B. Weisman, "Structure-Assigned Optical Spectra of Single-Walled Carbon Nanotubes" *Science* **298**, pp.2361-2366 (2002).
- [7] L. Alvarez, A. Righi, T. Guillard, S. Rols, E. Anglaret, D. Laplaze, and J. Sauvajol, "Resonant Raman study of the structure and electronic properties of single-wall carbon nanotubes" *Chem. Phys. Lett.* **316**, pp.186-190 (2000).
- [8] M. S. Dresselhaus, G. Dresselhaus, R. Saito, and A. Jorio, "Raman spectroscopy of carbon nanotubes" *Phys. Rep.* **409**, pp.47-99 (2005).
- [9] A. Jorio, M. A. Pimenta, A. G. Souza-Filho, R. Saito, G. Dresselhaus, and M. S. Dresselhaus, "Characterizing carbon nanotube samples with resonance Raman scattering" *New J. Phys.* **5**, pp.139.1-139.17 (2003).
- [10] A. Kasuya, Y. Sasaki, Y. Saito, K. Tohji, and Y. Nishima, "Evidence for Size-Dependent Discrete Dispersions in Single-Wall Nanotubes" *Phys. Rev. Lett.* **78**, pp.4434-4437 (1997).

- [11] L. G. Cançado, M. A. Pimenta, R. Saito, A. Jorio, L. O. Ladeira, A. Grueneis, A. G. Souza-Filho, G. Dresselhaus, and M. S. Dresselhaus, “Stokes and anti-Stokes double resonance Raman scattering in two-dimensional graphite” *Phys. Rev. B* **66**, 035415 (2002).
- [12] L. G. Cançado, K. Takai, T. Enoki, M. Endo, Y. A. Kim, H. Mizusaki, A. Jorio, L. N. Coelho, R. Magalhães-Paniago, and M. A. Pimenta, “General equation for the determination of the crystallite size  $L_a$  of nanographite by Raman spectroscopy” *Appl. Phys. Lett.* **88**, 163106 (2006).

## **Chapter 3. Optical diagnostics and the synthesis mechanism on arc-plasma-synthesized SWNTs in the arc plasma**

### **3.1 Backgrounds of the SWNTs synthesis in arc plasmas**

The anode electrode with catalytic metals evaporated by the arc plasma can synthesize highly crystalline SWNTs. However, the synthesis mechanism of SWNTs with the high crystallinity has not been clarified. Controlling quality of synthesized SWNTs is one of important factors for applications. Catalytic metals are necessary to synthesize SWNTs in the arc plasma method. Interaction between carbon species and catalytic metals is one of key reactions of SWNTs growth. Investigation of chemical species behaviors in the arc plasma can be obtained from OES. The arc plasma has the intense emitting light. This emission includes the information of active species in the arc plasma as shown in chapter 2. In this study, evaporated carbons and catalytic metals were focused. Comparing the results of OES and Raman scattering spectroscopy, relationships between the plasma state for each condition and the crystallinity of synthesized SWNTs were investigated.

### **3.2 Experimental setup**

#### **3.2.1 Arc plasma synthesis of SWNTs**

Experimental setup used in this study was schematically shown in Figure 3.1. The arc plasma chamber for SWNTs synthesis had windows for OES system. The chamber dimension was 300 mm inner diameter and 400 mm height made by stainless steel (SUS). At the center of the chamber, two electrodes with an arc discharge gap were introduced. The electrode position adjuster was installed to the chamber. The anode

electrode was set at the position adjuster side holder and the cathode was set at opposite of the anode. The anode electrode was made of carbon and catalytic metals. The composition ratio of the anode was C:Ni:Y=94.8:4.2:1.0% [1]. The diameter of the anode electrode was 6 mm. The anode electrode was manufactured by Toyo Tanso Co.,Ltd. The cathode electrode was made of 99.99% carbon. Diameter of the cathode electrode was 10 mm. The cathode electrode was the marketed production by The Nilaco Corporation C-072651.

The chamber was evacuated by a rotary pump to pressures below 5 Pa. After the evacuation, the pure He was introduced to the chamber. The arc plasma was generated by applying a constant current from the welding power source (Panasonic YC-300BZ3). When the arc plasma was ignited, electrodes distance was as close as 3 mm. The discharge voltage was maintained at an approximately 24 V by adjusting electrodes gaps. In this study, a dependence on two parameters such as current or pressure was focused on the clarification. In the case of changing current, the applying constant current was set at 70, 90, or 110 A with He pressure at 13.3 kPa. In the case of changing pressure, the He pressure was set at 13.3, 26.6, or 39.9 kPa. Table 3.1 shows the summary of experimental conditions. All discharges were sustained for 90 s. The anode was evaporated and the soot was generated. The soot deposited on the chamber wall and periphery of cathode. The samples were collected from the axis of the electrodes and the horizontal lateral chamber wall at the same height as the area between electrodes. The collected soot was analyzed by electron microscopy and Raman scattering spectroscopy.

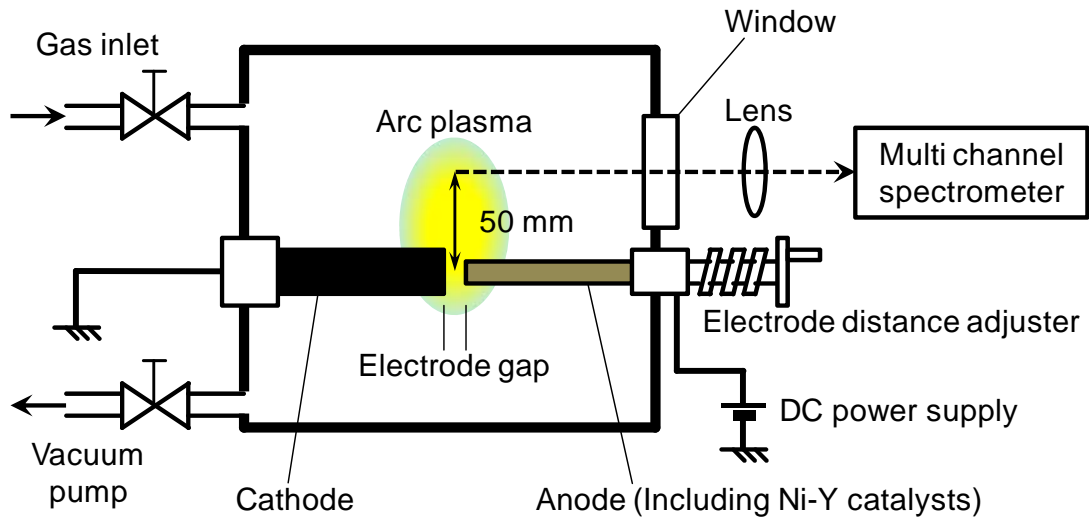


Figure 3.1. Experimental setup to measure optical emission of arc plasma during SWNTs synthesis.

Table 3.1. Summary of experimental conditions.

	Current dependent experimental setup	Pressure dependent experimental setup
Anode	C:94.8 + Ni:4.2 + Y:1.0%	
Cathode	C:99.99%	
Applying current	70, 90, 110 A	70 A
He pressure	13.3 kPa	13.3, 26.6, 39.9 kPa
Voltage	24 V	
Time	90 s	

### 3.2.2 Optical measurements of the arc plasma

Plasma diagnostic was carried out by the OES. For the optical measurement, the optically transparent window is necessary on the synthesis process chamber. The optically transparent window means the window which can pass the light at wavelength region from ultraviolet (UV) to near-infrared (NIR) because carbon, Ni, and Y species emissions appear around visible (VIS) light region. The chamber was equipped with quartz (SiO<sub>2</sub>) windows, which has the transparent region from 200 to 2000 nm and its transmittance is uniform. Plasma emitting light at 50 mm above electrodes gap was collected by a lens. This position is suitable for the detection of the emissions, because the high temperature of arc plasma ingenerate thermal convection and plasma plume extended to upside of electrodes gap. Collected light was measured by the multichannel spectrometer (Ocean Optics HR-4000) with an optical fiber.

### 3.2.3 Crystallographic analyses of the synthesized SWNTs

After the discharge, morphologies of synthesized SWNTs were observed by the transmission electron microscopy (TEM; Hitachi H-7000). For the TEM observation, the collected soot was dispersed in the ethanol by the ultrasonication. The dispersed soot was taken with dropper and hanged it on the TEM grid.

Crystallographic analysis of synthesized SWNTs was carried out by Raman scattering spectroscopy (Kaiser Raman RXN Systems). Usually, the SWNTs have a radical breathing mode (RBM) ranged from 160 to 180 cm<sup>-1</sup> in the Raman spectra. Also the Raman spectra have the D- and G-band. The D-band appeared at 1336 cm<sup>-1</sup>, and the G-band was divided into two peaks as G<sup>-</sup> and G<sup>+</sup>-band at 1569 and 1593 cm<sup>-1</sup>, respectively. Crystallinities of SWNTs were evaluated from the G/D ratio which was

calculated from G<sup>+</sup>-band peak intensity over D-band peak intensity.

### 3.3 Experimental results and discussion

#### 3.3.1 Dependence of the arc current on synthesized SWNTs crystallinity

Anode evaporations and soot deposits were obtained at conditions of the different arc currents. Evaporation rate of anode is shown in Fig. 3.2. The evaporation rate increased with increasing arc current. When the arc current was increased, electron collision on the anode surface increased. As a result, the anode surface became high temperature and the evaporation rate increased. The evaporation rate changed to draw the curve. Similar trends were reported [2,3].

Figure 3.3 shows a TEM image of SWNTs synthesized at 70 A and 13.3 kPa. There were dark particles with approximately 5 to 30 nm diameter and bundled SWNTs with 1 to 2 nm diameter. This image showed typical morphology of SWNTs growth by arc plasma [1,2,4-8]. The dark particles were carbon-catalytic metal compound. These particles were covered by thin films. These films were amorphous carbon. Amorphous carbon film on carbon-catalyst particle generically becomes catalytic poison and disturbs SWNTs growth.

Raman scattering spectroscopy was carried out with collected soot placed on the slide glass. Figure 3.4 shows Raman scattering spectra obtained from samples. In the case of varying arc current, some peaks appeared at low Raman shift region shown in Fig 3.4(a). These peaks were assigned to the RBM of SWNTs. The Raman shift of RBM ranged from 160 to 180 cm<sup>-1</sup>. The diameters of synthesized SWNTs were calculated from Eq. (2.19). The average values of the diameters were calculated by weighting according to the intensities of each RBM peaks. Table 3.2 shows evaluated diameters of SWNTs. At

70 A, diameters of SWNTs ranged from 1.27 to 1.48 nm, 1.27 to 1.46 nm at 90 A, 1.25 to 1.44 nm at 110 A. Average of diameters were 1.43, 1.44, and 1.39 nm at 70, 90, and 110 A, respectively. These diameters were similar to typical value in Ni-Y catalyst used results [1,4]. Figure 3.4(b) shows the higher Raman shift region of D- and G-band. D-band appeared at  $1336\text{ cm}^{-1}$ . G-band was divided into two peaks as G<sup>-</sup> and G<sup>+</sup>-band at  $1569$  and  $1593\text{ cm}^{-1}$ , respectively. Crystallinities of SWNTs were evaluated from the G/D ratio which was calculated from G<sup>+</sup>-band peak intensity over D-band peak intensity. Most of the papers used this method, and the crystallinities were evaluated without contradiction [5-7]. The G/D ratio was shown in Table 3.2. The G/D ratio decreased with increasing arc current. The G/D ratio of SWNTs synthesized at 70 A marked the highest value of 35.5. This G/D ratio at 90 A was 22.6. At 110 A, G/D ratio was 9.8 which is very small value as SWNTs synthesized by arc plasma.

The crystallographic evaluations were carried out to the raw soot rather than purified SWNTs. Therefore, graphitic or amorphous carbons were involved in the samples. Crystallinities of SWNTs synthesized by the arc plasma were not high in the G/D ratio around 30. When the arc current increased, the G/D ratio value, 9.8, was extremely low by the reduction of the G-band intensity. This means that graphitic thin films or amorphous carbons might be involved in the samples.

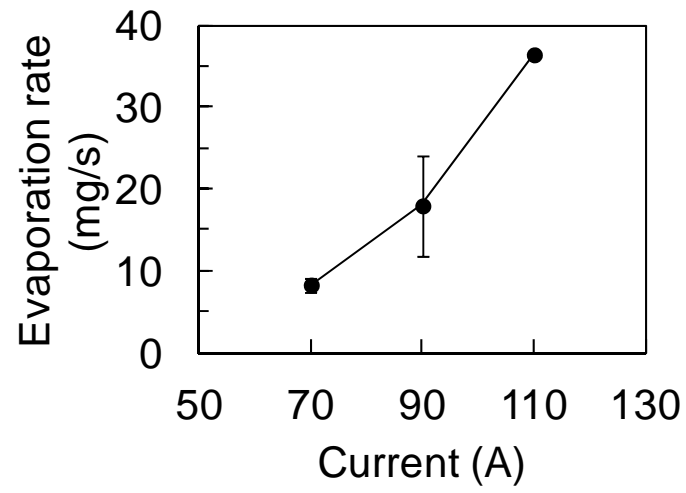


Figure 3.2. Evaporation rate of anode depending on arc current.

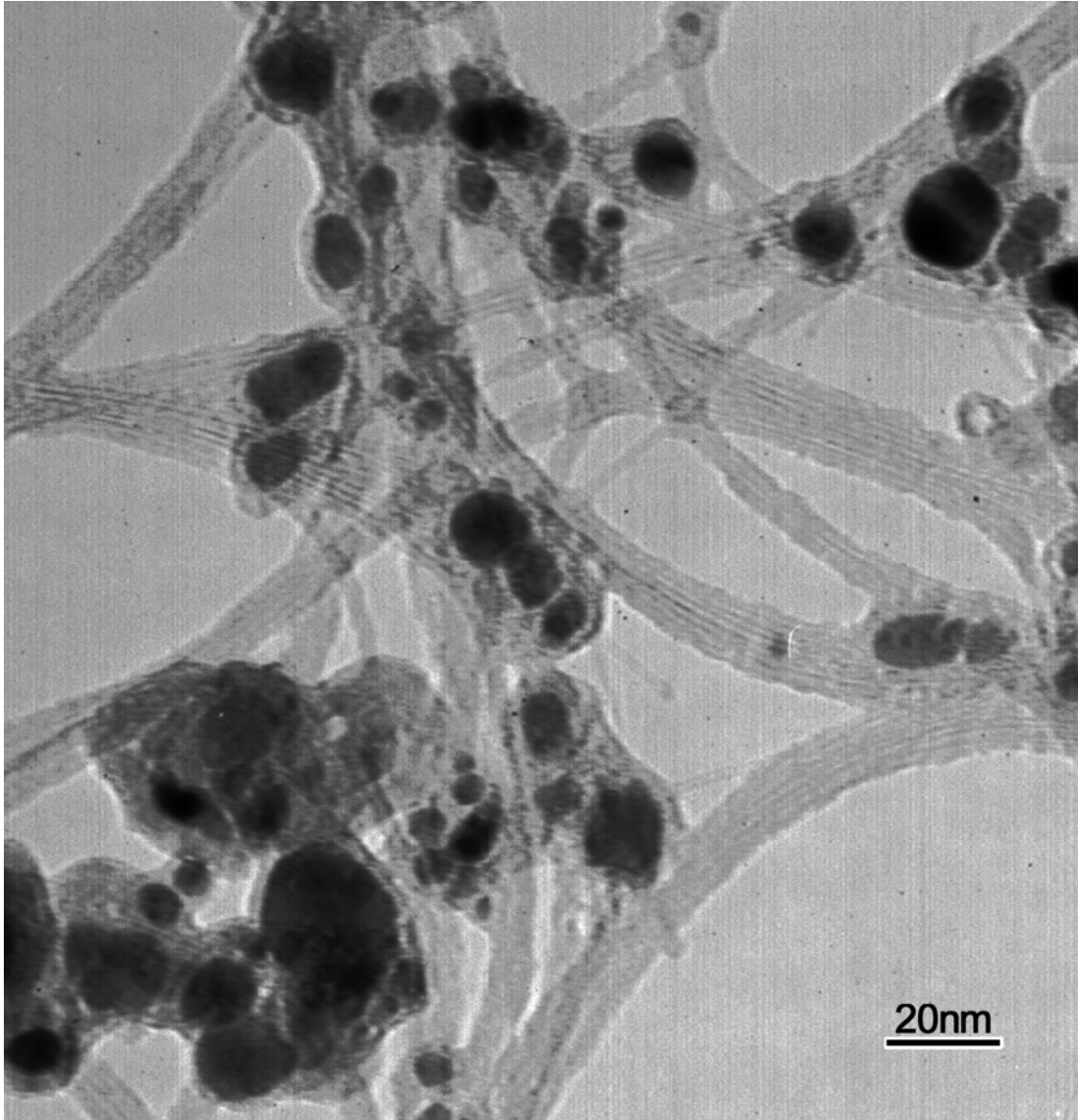
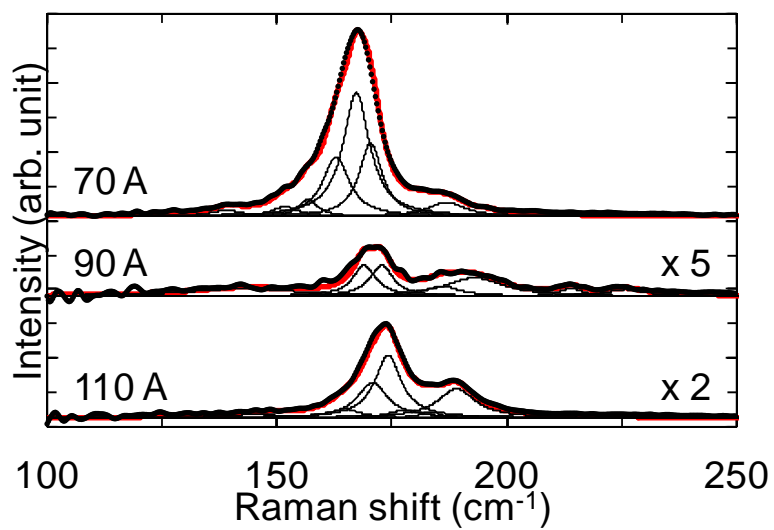
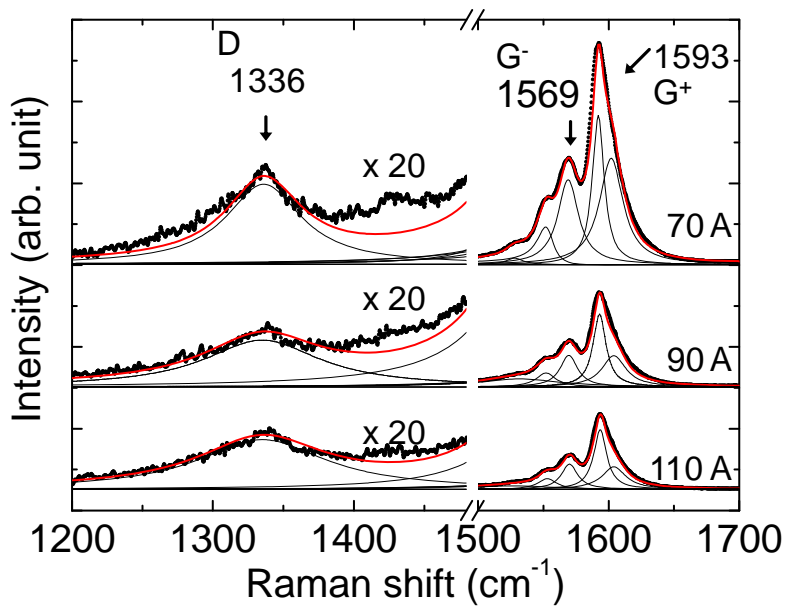


Figure 3.3. TEM image of SWNTs synthesized at 70 A, 13.3 kPa



(a)



(b)

Figure 3.4. Raman scattering spectra of synthesized SWNTs. (a) RBM region in the case of varying arc current. (b) High-frequency region in the case of varying arc current.

Table 3.2. Diameters and G/D ratios of Synthesized SWNTs dependence on arc current.

Current (A)	Diameter (nm)		G/D ratio
	Range	Average	
70	1.27-1.48	1.43	35.5
90	1.27-1.46	1.44	22.6
110	1.25-1.44	1.39	9.8

### 3.3.2 Dependence of the He pressure on synthesized SWNTs crystallinity

The anode evaporation rate is shown in Fig. 3.5. The evaporation rate increased with increasing He pressure. In the case of high pressure condition, the heat flux to the anode increases [8]. The Raman scattering spectra are shown in Figs. 3.6(a, b). RBM signals, D-, G<sup>-</sup>, and G<sup>+</sup>-band were obtained in all samples. Figure 3.6(a) shows RBM region of obtained Raman spectra. Table 3.3 shows evaluated diameters of SWNTs. Diameter distribution was 1.27 to 1.48 nm at 13.3 kPa, 1.28 to 1.45 nm at 26.6 kPa, and 1.39 to 1.48 at 39.9 kPa. Diameter average was 1.43, 1.44, and 1.43 nm at 13.3, 26.6, and 39.9 kPa, respectively. The average of diameter was almost same at the all pressures. The diameter distribution increased with increasing He pressure. Figure 3.6(b) shows D-, G<sup>-</sup> and G<sup>+</sup>-band region of Raman spectra. The G/D ratios were shown in Table 3.3. The G/D ratio decreased with increasing He pressure. At 26.6 kPa, the G/D ratio was 12.4. At 39.9 kPa, the G/D ratio was 12.2 which was almost same as at 26.6 kPa.

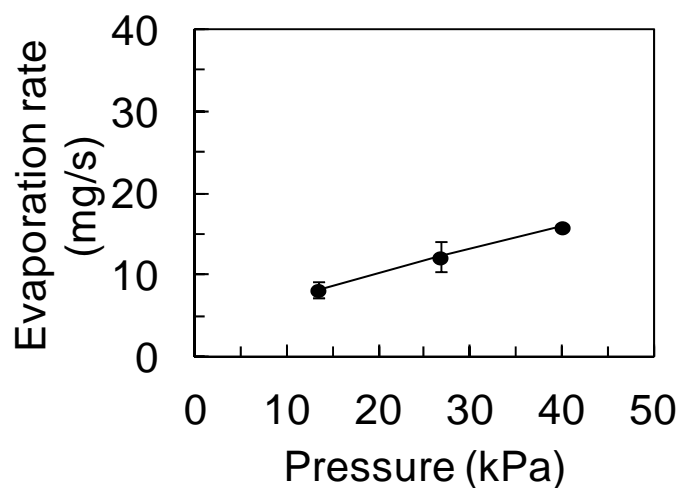
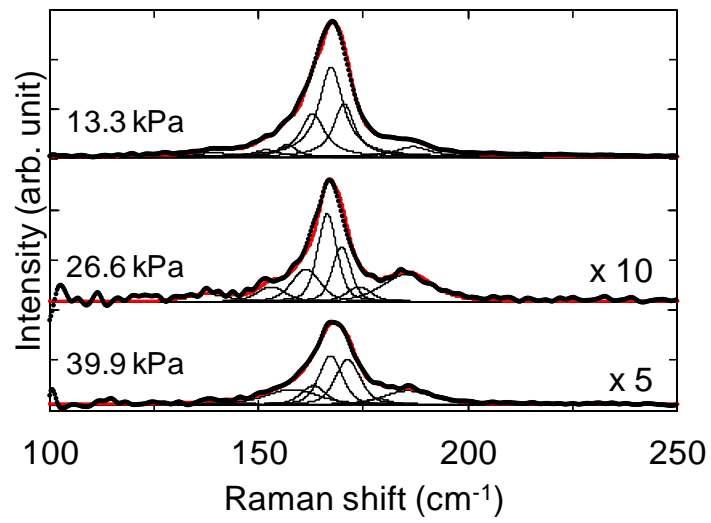
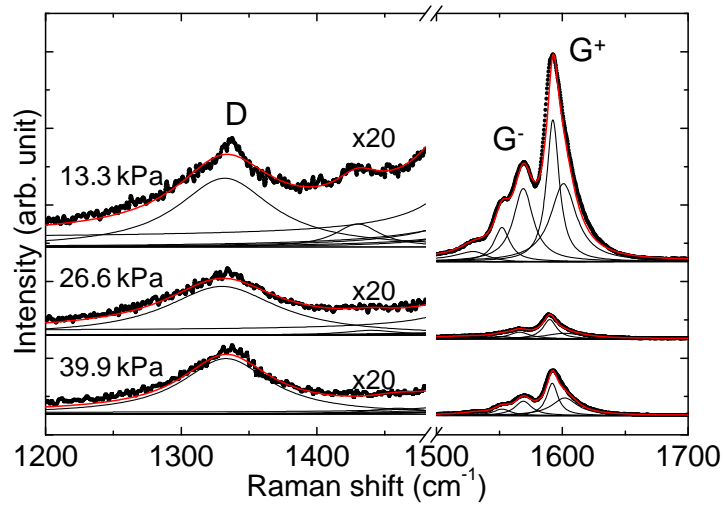


Figure 3.5. Evaporation rate of anode depending on He pressure.



(a)



(b)

Figure 3.6. Raman scattering spectra (a) RBM region in the case of varying He pressure.

(b) High-frequency region in the case of varying He pressure.

Table 3.3. Diameters and G/D ratios of Synthesized SWNTs dependence on He pressure.

Pressure (kPa)	Diameter (nm)		G/D ratio
	Range	Average	
13.3	1.27-1.48	1.43	35.5
26.6	1.28-1.45	1.44	12.4
39.9	1.39-1.48	1.43	12.2

### 3.3.3 Optical diagnostics of the arc plasma during SWNTs synthesis

OES measurements were carried out before the arc plasma ignition, during discharges until turned-off. Spectra results were automatically saved in the storage, temporal analyses of alteration of the arc plasma were also done in details. When the arc plasma was ignited, the distance between electrodes was set at an approximately 3 mm. Then, the electrodes gap distance was maintained to set voltage at 24 V by the mechanical adjuster of the anode electrode. This procedure takes about ten several seconds. The arc plasma became the stable state passing 30 s from ignition of arc plasma. Therefore, the data obtained 30 s passing from ignition were used for the analysis.

Figure 3.7(a) shows emission spectra of arc plasma at 30 s passing from ignition normalized by C<sub>2</sub> emission intensity at 516 nm ( $\nu', \nu''$ ) = (0,0). In all conditions, C<sub>2</sub> Swan band, Ni atom, and Y atom emissions were obtained. In addition, broad emissions were detected. Figure 3.7(b) shows an enlarged figure of Fig. 3.7(a) ranged from 545 to 570 nm. This region included C<sub>2</sub> Swan band  $\Delta\nu = -1$  ( $d^3\Pi_g - a^3\Pi_u$ ), many Ni and Y emissions. In the case of varying arc current, Ni and Y emissions became the stronger at 70 A.

Figure 3.7(c) shows emission spectra when He pressure was changed and Fig 3.7(d) is enlarged figure. C<sub>2</sub> Swan band, Ni, and Y emissions were detected. The emission intensities of catalytic metals decreased with increasing He pressure.

Although the absolute density of species in plasmas is not evaluated from emissions, the relative abundance can be estimated by comparing with emission intensity ratio. The intensity ratios of C<sub>2</sub> ( $\nu', \nu''$ ) = (0,1) at 563 nm against Ni at 566 nm and C<sub>2</sub> ( $\nu', \nu''$ ) = (2,3) at 553 nm against Y at 554 nm are shown in Fig. 3.8(a) with the G/D ratio. The intensity ratio and G/D ratio decreased with increasing arc current. It is thought that there are relationships between emissions of active species in plasmas and crystallinities

of synthesized SWNTs.

Emissions from excited species have their state information. In this case, C<sub>2</sub> Swan band emissions were clearly seen and C<sub>2</sub> energy can be estimated from vibrational emission lines. The vibrational temperature ( $T_v$ ) was calculated from C<sub>2</sub> Swan band  $\Delta\nu = -1$  emissions using Boltzmann plot of band head emission intensities as

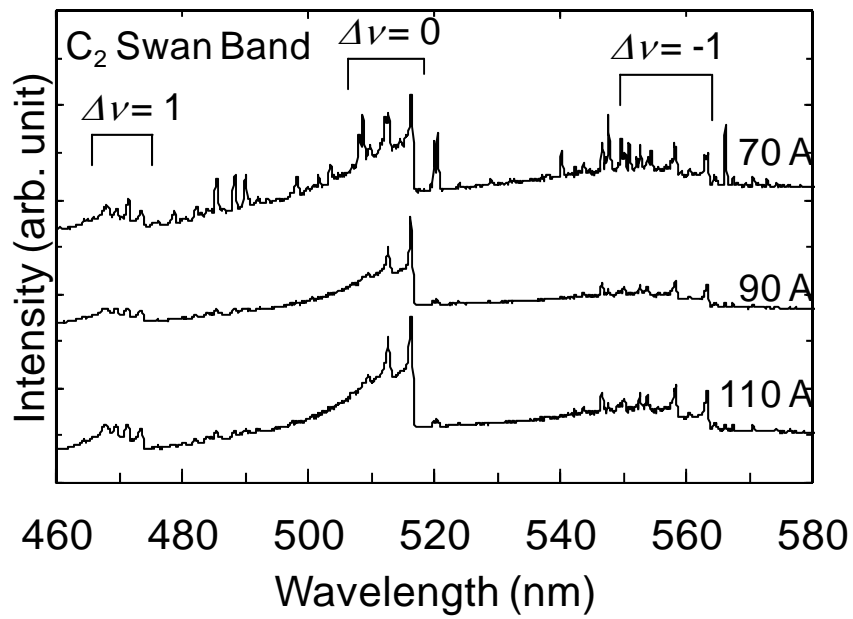
$$\ln\left(\frac{I_{\nu',\nu''}\lambda}{K(\lambda)A_{\nu',\nu}}\right) = \left(\frac{-E_{\nu'}}{k_B T_v}\right) + C, \quad (3.1)$$

where  $K(\lambda)$  is response factor of detector and  $C$  is constant [9]. Figure 3.9 shows  $T_v$  of C<sub>2</sub> with G/D ratio. In the case of varying arc current,  $T_v$  was almost same value or slightly decreased as 4250 K at 70 A, 4210 K at 90 A, 4200 K at 110 A. On the other hand,  $T_v$  decreased with increasing He pressure as 4250, 3680, and 3630 K, at 13.3, 26.6, and 39.9 kPa, respectively.

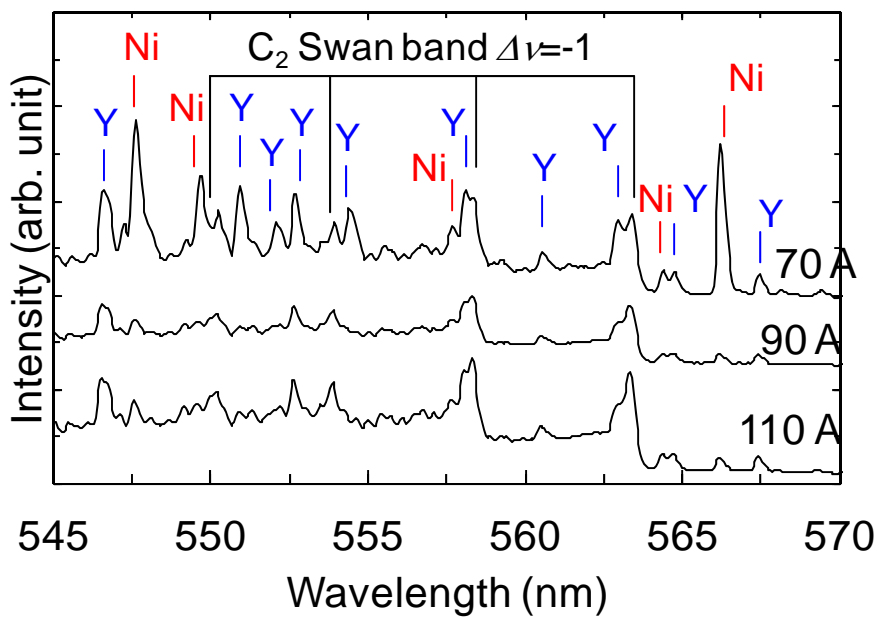
Arc plasma emission includes thermal radiation other than light emission transitions of excited species. Thermal radiation has emission with broad wavelength range dependence on temperature. The peak wavelength of this emission depends on temperature. The relationship between peak wavelength ( $\lambda_{\max}$ ) and temperature ( $T$ ) is described by Wien's displacement law [10] as

$$T = \frac{0.002898}{\lambda_{\max}}. \quad (3.2)$$

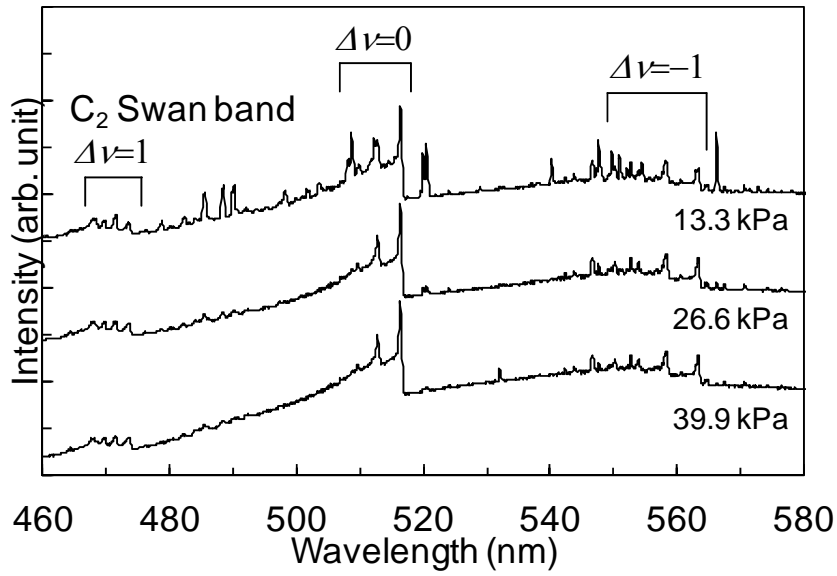
Calculated  $T_v$  of C<sub>2</sub> and  $T$  with G/D ratio are shown in Fig. 3.10.  $T$  increased with increasing arc current. At 70 A,  $T$  was the smallest as 5390 K. In the case of varying He pressure,  $T$  was almost same or slightly increased from 5390 to 5490 K with increasing He pressure.



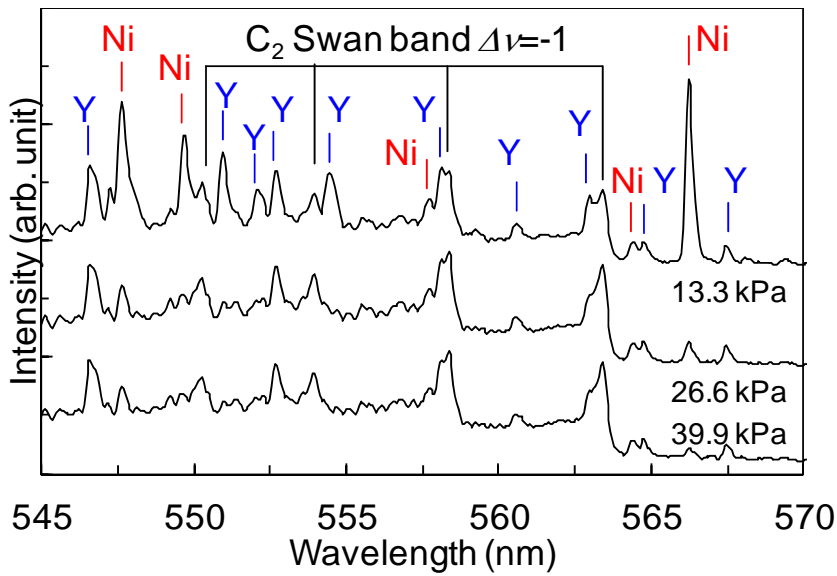
(a)



(b)

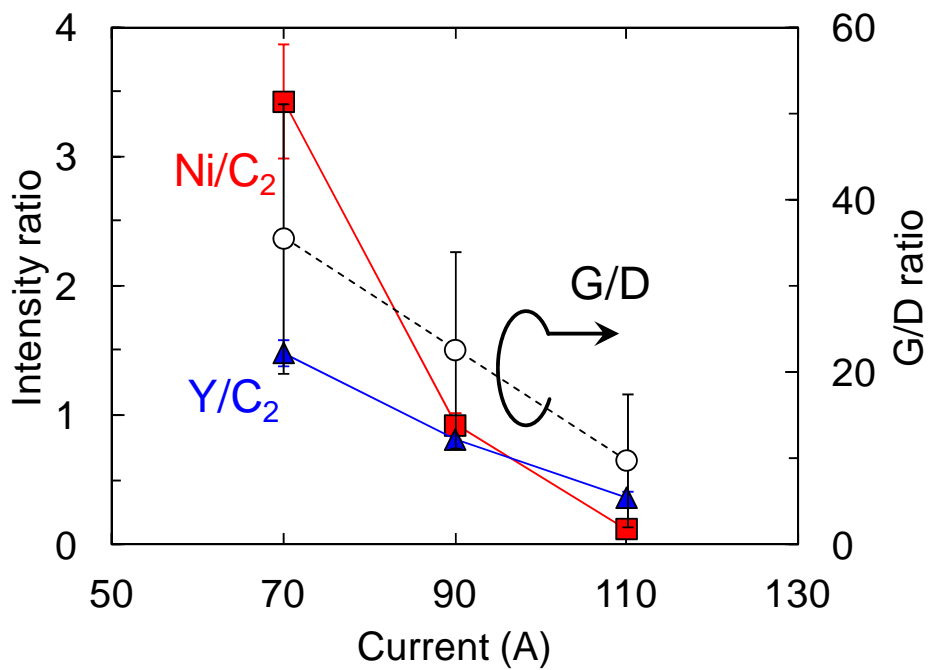


(c)

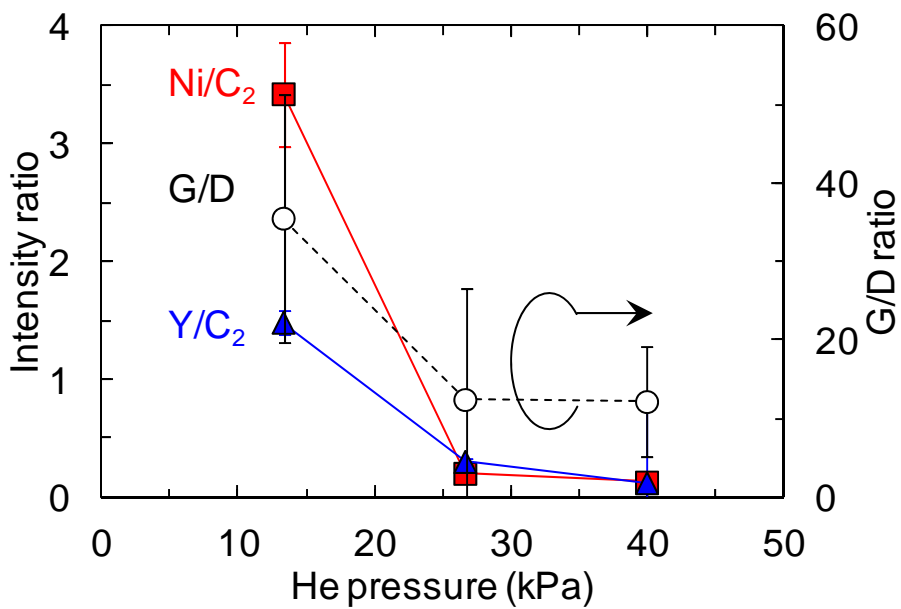


(d)

Figure 3.7. Optical emission spectra of arc plasma 30 s passing from ignition normalized by C<sub>2</sub> at 516 nm emission intensity.. (a) C<sub>2</sub> Swan band  $\Delta\nu = -1, 0, 1$  region dependence on arc current. (b) Enlarged in C<sub>2</sub> Swan band  $\Delta\nu = -1$  region dependence on arc current. (c) C<sub>2</sub> Swan band  $\Delta\nu = -1, 0, 1$  region dependence on He pressure. (d) Enlarged in C<sub>2</sub> Swan band  $\Delta\nu = -1$  region dependence on He pressure.

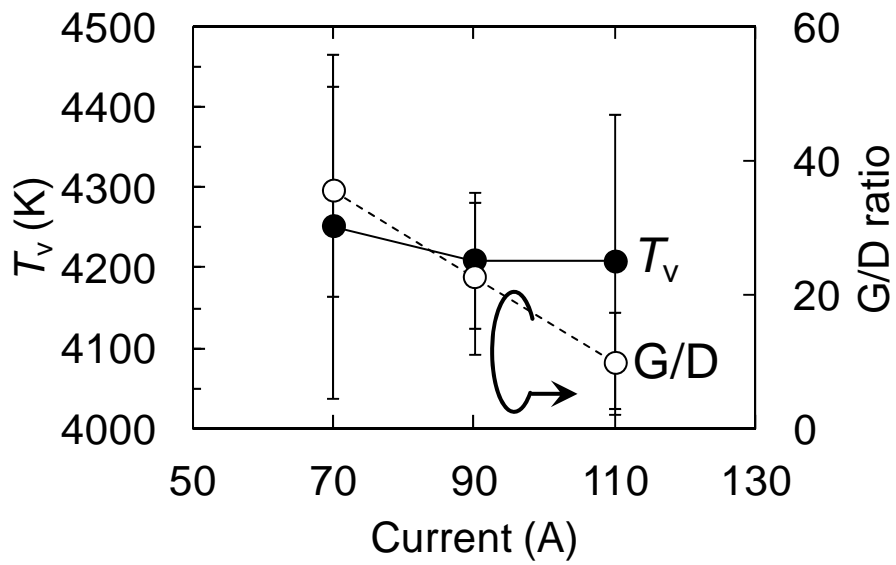


(a)

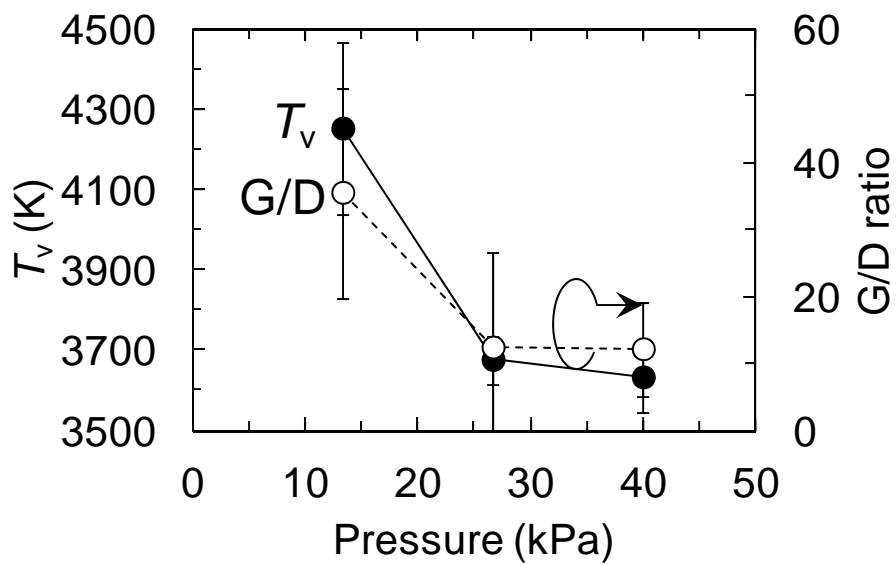


(b)

Figure 3.8. Emission intensity ratios of Ni/C<sub>2</sub> and Y/C<sub>2</sub> with G/D ratio. (a) Dependence on arc current. (b) Dependence on He pressure.

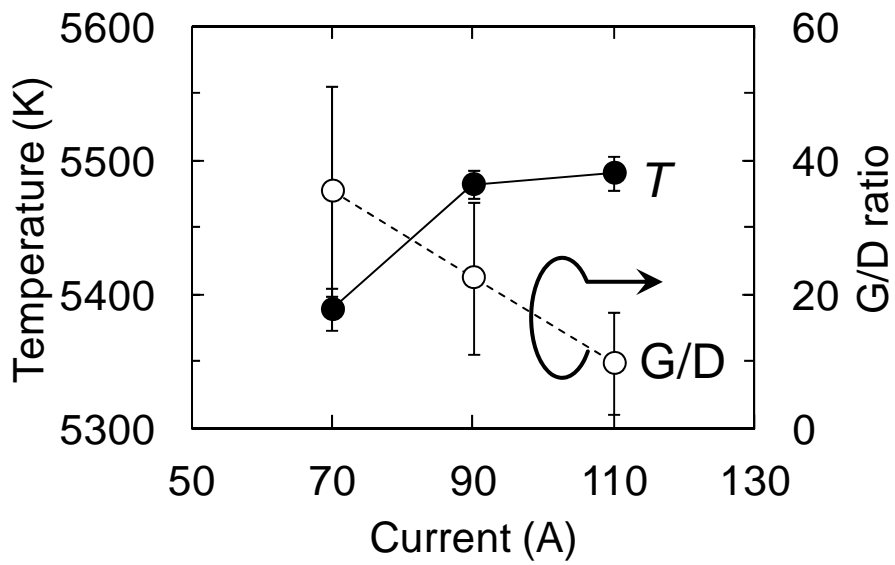


(a)

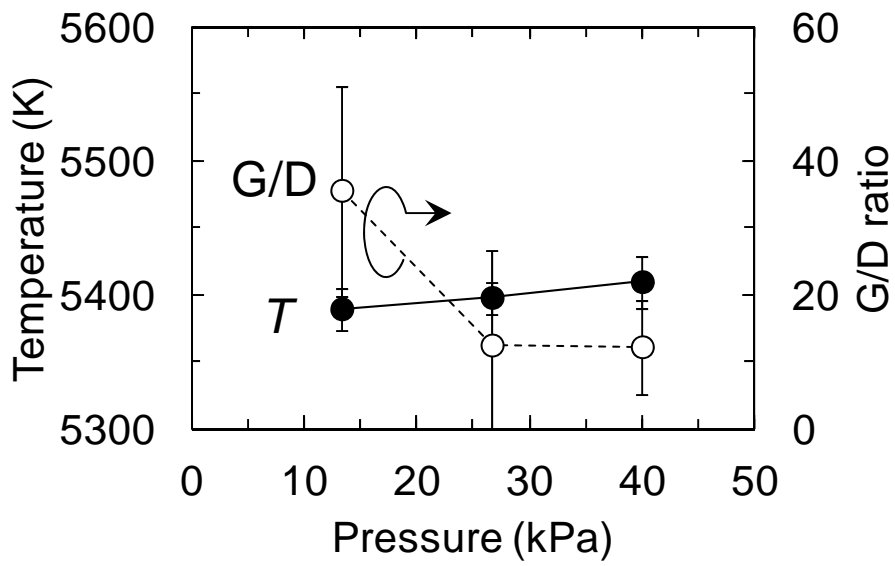


(b)

Figure 3.9.  $T_v$  of  $C_2$  and G/D ratio. (a) Dependence on arc current. (b) Dependence on He pressure.



(a)



(b)

Figure 3.10.  $T$  calculated by Wien's displacement law. (a) Dependence on arc current. (b) Dependence on He pressure.

### 3.3.4 Discussion: a relationship between SWNTs growth and optical emission intensities from species in arc plasmas

SWNTs with different crystallinities were synthesized by various conditions and the OES measurement of arc plasma was carried out. In comparison Ni/C<sub>2</sub> and Y/C<sub>2</sub> with G/D ratio, the tendencies were similar as shown in Fig. 3.8. Intensity ratios, Ni/C<sub>2</sub> and Y/C<sub>2</sub>, indicated that relative abundances of excited catalytic metal atoms. It was thought that higher concentration of excited catalytic metal atoms worked on the high-crystalline SWNTs growth. The cause of decreasing intensity ratio potentially related anode evaporation rates. The anode electrode was made of carbon with uniformly dispersed Ni and Y. Therefore, evaporated elements ratio does not change when the evaporation rate changes by the arc plasma generated condition. The evaporation rates increased with increasing arc current or He pressure.

In the case of increasing arc current, increase of the anode evaporation rate shown in Fig. 3.2 was induced by the electrons collisions increase. This fact was also evident in the temperature change shown in Fig 3.10(a). In the case of increasing He pressure, the heat flux to the anode became large at the high pressure condition [8] The anode evaporation rate shown in Fig 3.5 increased with increasing He pressure. The plasma temperature shown in Fig. 3.10(b) also changed in the same way. The particle concentration in the arc plasma increases with increasing the evaporation amount. The high density induces the frequent collision due to the decrease of mean free pass. Collided excited atoms quench or adhere to collided particle. These particles do not irradiate light. In addition, the input energy was dispersed in the particles in the arc plasma due to increase of the evaporation rate. This induced that the metals were not atomized or excited. The aggregation of carbon and catalytic metal is necessary to grow

SWNTs but the excess supply of carbon sources induces the oversaturation of carbon and covering the catalytic particle with carbon films. As a result, carbons, which did not become SWNTs, increased and formed amorphous carbons. These appeared as decreasing G/D ratio. Excited Ni and Y atoms are one of important factors for SWNTs synthesis. Control of synthesis conditions as arc current and He pressure achieves highly-crystalline SWNTs synthesis. The OES measurement has a high potential to be used for controlling crystallinity of SWNTs.

Growth SWNTs diameters were changed each condition as shown in Tables 3.2 and 3.3. When the arc current increased, increasing carbons and catalytic metals densities induced the aggregation of carbons and oversaturated at an early stage. High density of chemical species in the arc plasma easily occurred due to the high frequent collision with decreasing mean free path. In addition, the high anode evaporation rate induced increasing arc plasma region pressure. The particles in arc plasma were pushed out of arc plasma at once. Therefore, smaller size particles were formed and could grow SWNTs with smaller diameter [11,12]. In contrast, evaporated species dispersion was disturbed due to higher He pressure conditions. Evaporated species were confined by the ambient He gas and formed larger particles [13]. The higher He pressure condition has a potential to grow larger diameter SWNTs but the higher collision frequency is induced at the same time. Therefore, G/D ratio decreased due to the collision and the formation of carbon clusters. In the case of CVD for SWNTs synthesis, the *yarmulke* mechanism is proposed that the diameter of growing SWNTs is determined by the size of catalyst particles [14]. Carbon atoms or molecules are adsorbed on the metal nanoparticles and hemispherical caps are formed on the surfaces of the nanoparticles by carbon diffusion. For the larger diameter nanoparticles, the second cap is formed under the first cap and the MWNTs

grow. Carbon is supplied to the cap from the edge of the cylinder that is in contact with the catalyst surface. Since the radius of curvature of the second and subsequent caps becomes small, the formation of cap is restricted due to an increase in strain energy. Even in arc plasma, cap formation occurs on the catalyst nanoparticles and they are coupled when moving to the plasma remote region on the thermal convection. After that, SWNTs grow from catalyst particles of 5 to 30 nm as seen in the TEM image shown in Fig. 3.3.

The estimated  $T_v$  of  $C_2$  shown in Fig. 3.9 indicated the  $C_2$  energy. The  $T_v$  was almost the same when the arc current was changed as shown in Fig. 3.9(a). The input power increased with increasing the arc current. The input power was used for the dissociation and the acceleration of chemical species. If the chemical species densities increased with increasing the arc current, the input power was dispersed. Therefore, the input energy per particle does not change significantly. In the case of changing He pressure, the input power was the same in all conditions. However, the evaporation rate increased with increasing the He pressure due to increasing heat flux [8]. Decreasing  $T_v$  with increasing He pressure shown in Fig 3.9(b) was induced by the stable input power and increasing particles density in the arc plasma. Comparing the arc plasma condition at 90 A, 13.3 kPa with at 70 A, 26.6 kPa, these two conditions had different G/D ratios as 22.6 and 12.4, respectively, which are approximately two times different.  $C_2$  with high energy affected highly-crystalline SWNTs formation. On the other hand, it is thought that the effect of  $C_2$  energy is not so large to grow highly-crystalline SWNTs. When compared with the intensity ratios, Ni/ $C_2$  and Y/ $C_2$  shown in Fig. 3.8, the tendency did not coincide with the G/D ratio, so it is considered that  $T_v$  of  $C_2$  was not main factor for determining crystallinity of synthesized SWNTs.

The temperature,  $T$  shown in Fig. 3.10(a), estimated from Wien's displacement

law increased with increasing the arc current. This is probably due to increase the number of particles that obtain more energy because the input power increased. The reason why the  $T$  tendency differed from  $T_v$  of  $C_2$  shown in Fig. 3.9(a) is considered that the ratio of other particles to  $C_2$  increased. In the case of varying He pressure,  $T$  was almost the same as shown in Fig. 3.10(b). The input power was not changed. It was thought that the input energy was preserved because the binding was promoted by trapping particles in narrow space by the high pressure. The estimated  $T$ , 5390 to 5490 K, was enough high comparing with the temperature to 3915 K which is sublimation point of carbon. In addition, the range of change was within 100 K, and the range of change was small compared to  $T_v$  of  $C_2$  (3630 to 4250 K). Therefore, it was thought that temperature effect to SWNTs growth was not large.

### 3.5 Conclusion of chapter 3

In the arc plasma employing catalytic metal including carbon electrode for SWNTs synthesis, the synthesized SWNTs were analyzed. Different crystallinities of the SWNTs were observed when the applied arc current and/or He pressure were changed. The SWNTs crystallinities were evaluated by Raman scattering spectroscopy. The G/D ratio of synthesized SWNTs decreased with increasing the arc current or increasing the He pressure. The author studied a reason why the arc plasma conditions determined the crystallinity of the synthesized SWNTs.

Emission spectra of arc plasmas obtained by OES had  $C_2$ , Ni, and Y emissions. For the estimation of abundance ratio,  $C_2$  to catalytic atoms emission intensity ratios were calculated. The author found that the intensity ratio of Ni/ $C_2$  and Y/ $C_2$  linked with the G/D ratio. Since the high intensity ratio means the high abundance ratio of excited

species, this result suggested that excited catalytic metal atoms have played important roles to grow the highly-crystalline SWNTs. The changing Ni/C<sub>2</sub> and Y/C<sub>2</sub> might be induced by the collision and absorption into the metal catalyst.

These C<sub>2</sub> radical and metal catalyst species were originated from the evaporation of the anode electrode, which contained uniform mixture of carbon and catalytic metals. As carbon and catalytic metals supplemented in the gas-phase, the ratio might be kept a constant ratio regardless of the evaporation amount of anode.

In the case of higher evaporation rate, the collision frequently increased and the deexcitation process dominated. The deexcitation occurred in two possibilities; one was emissive energy-level transition and the other was nonradiative relaxation. The frequent collision induced the quenching at higher arc currents and higher He pressures. Therefore, large amounts of evaporating species in the gas-phase may disturb the improvement of the crystallinity in the SWNTs growth.

The distribution of diameters of the synthesized SWNTs decreased with increasing arc current. This was predominantly due to the large diameter of metal catalysts. When chemical species in the arc plasma became high density, mean free paths of the species decreased and collision frequency among the species increased. The size of metal-catalyst particles dispersed within early stage of absorption carbon into the metal catalyst. Especially for the high pressure process of arc plasma with the high arc current, evaporated species were filled with high density in the arc discharge regions.

Moreover, the diameter increased with increasing He pressure. At the high pressure ambient, the evaporated species aggregated favorably. This phenomenon supported large-size particle formation. Therefore, large-diameter SWNTs were synthesized at high He pressures.

$T_v$  of  $C_2$  was calculated from  $C_2$  Swan band  $\Delta\nu = -1$  emission.  $T_v$  was changed with the amount of anode evaporation and arc current. In the case of changing the arc current, the input power of arc plasma increased with increasing the arc current.  $T_v$  hardly changed. It was considered that the energy was dispersed due to increasing evaporation amount.  $T_v$  decreased with increasing He pressure at the same arc current. The energy was dispersed due to the large evaporation amount at high He pressures. The range of  $T$  change was smaller than  $T_v$ .  $T$  was enough high value compared to carbon sublimation point.  $T$  of particles increased with increasing the arc current.

Consequently, a monitoring of the OES signals of Ni/ $C_2$  and Y/ $C_2$  enables us to control the crystallinity of synthesized SWNTs. For highly-crystalline SWNTs synthesis, the higher Ni/ $C_2$  and Y/ $C_2$  are required. The higher anode evaporation rate condition induces the low-crystalline SWNTs growth. The author points out the trade-off relationship between the crystallinity and the synthesis amount.

## References

- [1] C. Journet, W. Maser, P. Bernier, A. Loiseau, M. L. Chapelle, S. Lefrant, P. Deniard, R. Lee, and J. E. Fischer, "Large-scale production of single-walled carbon nanotubes by the electric-arc technique" *Nature* **388**, pp.756-758 (1997).
- [2] Y. Ando, X. Zhao, K. Hirahara, K. Suenaga, S. Bandow, and S. Iijima, "Mass-production of single wall-carbon nanotubes by the arc plasma jet method" *Chem. Phys. Lett.* **323**, pp.580-585 (2000).
- [3] S. Farhat, I. Hinkov, and C. Scott, "Arc Process Parameters for Single-Walled Carbon Nanotube Growth and Production: Experiments and Modeling" *J. Nanosci. Nanotechnol.* **4**, pp.377-389 (2004).
- [4] Y. Ando, X. Zhao, K. Hirahara, K. Suenaga, S. Bandow, and S. Iijima, "Arc plasma jet method producing single-wall carbon nanotubes" *Diamond Relat. Mater.* **10**, pp.1185-1189 (2001).
- [5] T. Suzuki, K. Suhama, X. Zhao, S. Inoue, N. Nishikawa, and Y. Ando, "Purification of single-wall carbon nanotubes produced by arc plasma jet method" *Diamond Relat. Mater.* **16**, pp.1116-1120 (2007).
- [6] M. Kanai, A. Koshio, H. Shinohara, T. Mieno, A. Kasuya, Y. Ando, and X. Zhao, "High-yield synthesis of single-walled carbon nanotubes by gravity-free arc discharge" *Appl. Phys. Lett.* **79**, pp.2967-2969 (2001).
- [7] J. Li, M. Kundrapu, A. Shashurin, and M. Keidar, "Emission spectra analysis of arc plasma for synthesis of carbon nanostructures in various magnetic conditions" *J. Appl. Phys.* **112**, 024329 (2012).
- [8] E. I. Waldorff, A. M. Waas, P. P. Friedmann, and M. Keidar, "Characterization of carbon nanotubes produced by arc discharge: Effect of the background pressure" *J. Appl. Phys.* **95**, pp.2749-2754 (2004).
- [9] F. U. Khan, N. U. Rahman, S. Naseer, M. Y. Naz, N. A. D. Khattak, and M. Zakaullah, "Effect of Excitation and Vibrational Temperature on the Dissociation of Nitrogen Molecules in Ar-N<sub>2</sub> Mixture RF Discharge" *Spectrosc. Lett.* **44**, pp.194-202 (2011).
- [10] C. Poonjarernsilp, N. Sano, H. Tamon, and T. Charinpanitkul, "A model of reaction field in gas-injected arc-in-water method to synthesize single-walled

- carbon nanohorns: Influence of water temperature” J. Appl. Phys. **106**, 104315 (2009).
- [11] A. Gorbunov, O. Jost, W. Pompe, and A. Graff, “Solid-liquid-solid growth mechanism of single-wall carbon nanotubes” Carbon **40**, pp.113-118 (2002).
- [12] P. J. F. Harris, “Solid state growth mechanisms for carbon nanotubes” Carbon **45**, pp.229-239 (2007).
- [13] Y. Saito and Y. Tani, “Diameter of Single-Wall Carbon Nanotubes Depending on Helium Gas Pressure in an Arc Discharge” J. Phys. Chem. B **104**, pp.2495-2499 (2000).
- [14] H. Dai, A. G. Rinzler, P. Nikolaev, A. Thess, D. T. Colbert, and R. E. Smalley, “Single-wall nanotubes produced by metal-catalyzed disproportionation of carbon monoxide” Chem. Phys. Lett. **260**, pp.471-475 (1996).

## **Chapter 4. Nanographene synthesized by the in-liquid plasma employing various kinds of alcohols**

### **4.1 Backgrounds of this study**

In-liquid plasmas employing alcohols are one of novel techniques to synthesize carbon nanomaterials [1]. The synthesis rate and the crystallinity of synthesized nanographene were difference depending on employed alcohol type. However, the reason of this difference and synthesis mechanism of nanographene by the in-liquid plasma has not been clarified yet. This difference was caused by a change in the reaction in the plasma due to the difference in the type of alcohol. Therefore, the investigation of chemical species in the in-liquid plasma provided the important information about the synthesis mechanism. The in-liquid plasma process for the nanographene synthesis does not require catalytic metals. This is different point from the arc plasma for the SWNTs synthesis. Although OES measurements of in-liquid plasma provide the information on chemical species in the plasma, there is not sufficient for information of reactions. Therefore, in this study, the analysis of alcohol treated by the in-liquid plasma was performed to investigate by-products and intermediates. Based on these results, the synthesis mechanism of nanographene by the in-liquid plasma was investigated and critical factors for synthesized nanographenes were also discussed.

### **4.2 Experimental setup**

#### **4.2.1 Synthesis method of nanographenes in the in-liquid plasma**

Figure 4.1 shows experimental setup of in-liquid plasma to nanographene synthesis. The synthesis chamber was made of glass with an inner size of 30 mm depth x

80 mm width. The glass chamber has ports with optical windows made of sapphire ( $\text{Al}_2\text{O}_3$ ). Electrodes made of SUS were placed to face each other across the liquid surface. Employed alcohol types were methanol ( $\text{CH}_3\text{OH}$ ), ethanol ( $\text{C}_2\text{H}_5\text{OH}$ ), 1-butanol ( $\text{C}_4\text{H}_9\text{OH}$ ), and 1-hexanol ( $\text{C}_6\text{H}_{13}\text{OH}$ ). Alcohol of 150 ml was filled up to one half of the glass chamber. The liquid surface was set at 2 mm above from the tip of the lower side electrode. Ar was flowed at 3 slm. The in-liquid plasma was generated after 1 min or more time passing since start of gas flow. A 8 kV modulated sinusoidal voltage was applied to generate the in-liquid plasma. The liquid level was maintained by the reservoir tube made of silicon.

After the synthesis, solid products and the residual liquid were separated by the filtration using 1- $\mu\text{m}$ -pore-size filters (Merck Omnipore JAWP04700). Obtained solid products were treated by 30%  $\text{H}_2\text{O}_2$  water at 120 °C in 120 min to remove the by-products such as amorphous carbons [1]. The crystallinity of nanographene evaluated by Raman scattering spectroscopy is improved by treating the synthesized nanographene with  $\text{H}_2\text{O}_2$  water.

Experimental conditions are shown in Table 4.1.

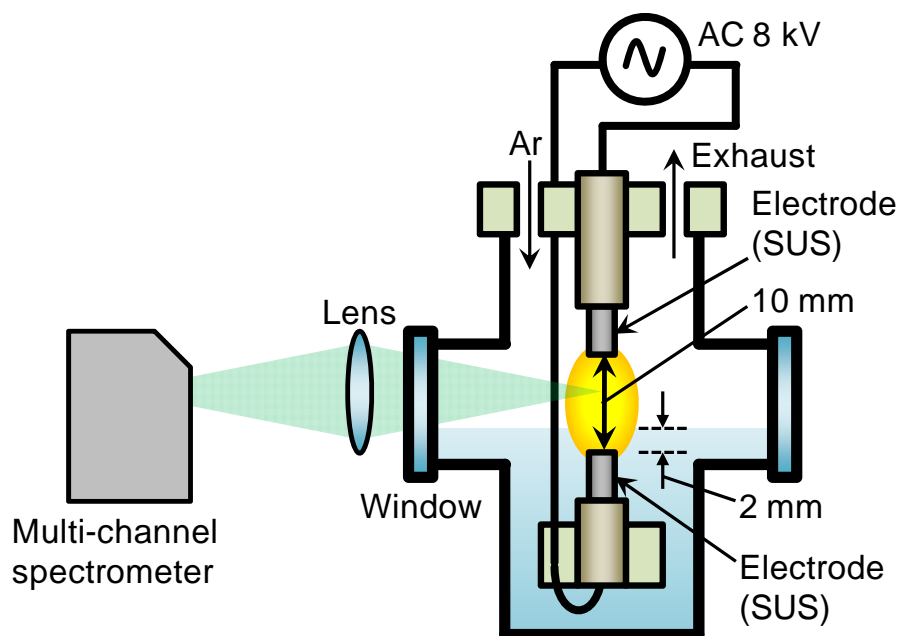


Figure 4.1. Experimental setup of in-liquid plasma to nanographene synthesis and OES.

Table 4.1. Experimental conditions to nanographene synthesis.

Applying voltage	8 kV	
Electrodes	SUS	
Gas	Ar, 3 slm	
Processing time	1, 3, 5, 10 min	
Alcohol	Methanol (CH <sub>3</sub> OH)	C-OH
	Ethanol (C <sub>2</sub> H <sub>5</sub> OH)	
	1-Butanol (C <sub>4</sub> H <sub>9</sub> OH)	
	1-Hexanol (C <sub>6</sub> H <sub>13</sub> OH)	
Filter	1 μm pore	
Treatment	H <sub>2</sub> O <sub>2</sub> water (30%), 120 min 120 °C	

#### 4.2.2 Optical measurements

The sapphire has over 80% uniform transmittance at wide-range from 250 to 4000 nm. Therefore, UV-VIS-NIR emission spectra can be detected. Figure 4.1 shows the nanographene synthesis equipment with plasma optical measurement system.

The in-liquid plasma was measured by multichannel spectrometer (Ocean Optics HR-4000) and high-resolution spectrometer (Andor Shamrock 500) connected with a fast-gated intensified charge-coupled device image sensor (Andor iStar 334T) with lens and optical fiber. The lens focus set at under the tip of the upper electrode.

#### 4.2.3 Crystallographic measurements

Crystallographic analyses of treated solid products were carried out by transmission electron microscopy (TEM; JEOL JEM2010) observation and Raman scattering spectroscopy (Renishaw InVia Reflex; 532 nm of excitation).

For TEM observation, solid samples were dispersed in the ethanol by the ultrasonication and dropped on TEM grids. TEM images were taken with the acceleration at 200 kV.

The residual liquid was analyzed by GC-MS (Hewlett-Packard HP6870 Series GC System with Agilent Technology J&W GC column DB-WAX 122-7032, 0.25 mm diameter, connected to a 5973 mass-selective detector) to determine by-products. Oven temperatures were changed from 40 to 290 °C with a heating rate at 10 °C/min.

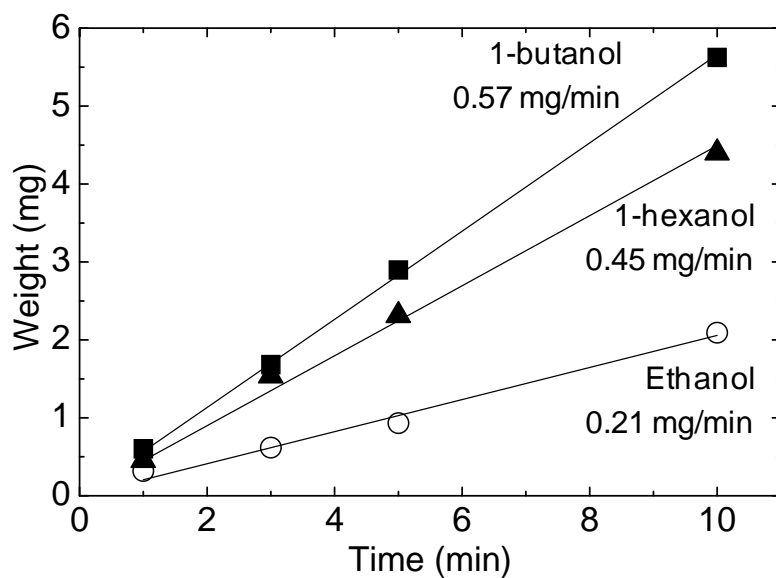
### 4.3 Results and discussion

#### 4.3.1 Synthesis rates of nanographene

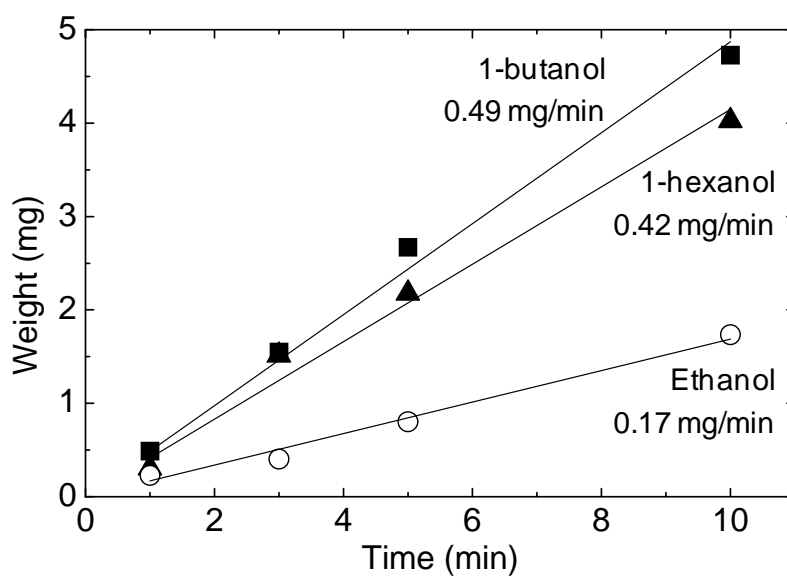
All alcohols employed in in-liquid plasmas changed the liquid color to dark

except for the methanol. After the filtration, the liquid color was changed yellow and the dark solid products were obtained except for the methanol. Collected solid products were treated by the H<sub>2</sub>O<sub>2</sub> water and measured the weights. Figure 4.2 shows synthesized products weight as before and after the H<sub>2</sub>O<sub>2</sub> water treatments. The synthesis rates decreased at after H<sub>2</sub>O<sub>2</sub> treatment. The decreased weights corresponded to the by-products. Synthesis amounts linearly increased with plasma irradiation time. Synthesis rates were different on each alcohol. In a case of the use of methanol, no product was synthesized. The ethanol had the smallest synthesis rate, 0.17 mg/min at after the treatment except for the methanol.

1-Butanol and 1-hexanol had almost the same synthesis rates, 0.49 and 0.42 mg/min, respectively, after the treatment. In the comparison ethanol and 1-butanol, it has been reported that the synthesis rate of 1-butanol became larger than that of ethanol [1]. Increasing synthesis rate dependent on the kinds of alcohols was considered that carbon atoms in unit molecule affected synthesis rates, i.e., the larger number of carbon atoms in unit molecule can synthesize the larger amount of nanographene. In the case of using 1-hexanol, the synthesis rate was not increased compared to that of 1-butanol.



(a)



(b)

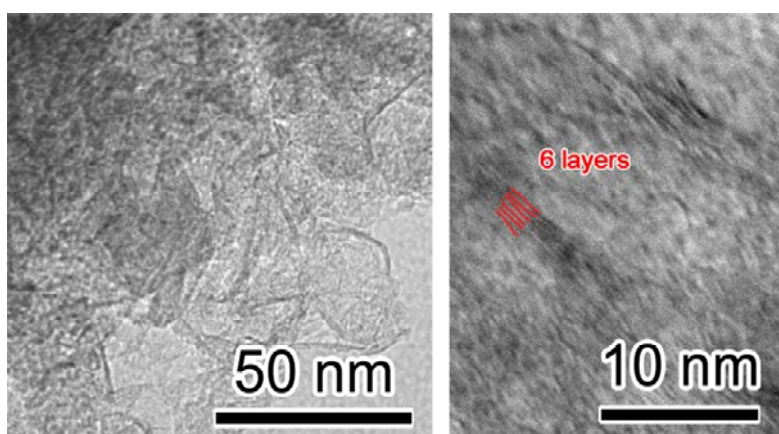
Figure 4.2. Synthesis amount of nanographene by in-liquid plasma. (a) Before H<sub>2</sub>O<sub>2</sub> water treatment. (b) After H<sub>2</sub>O<sub>2</sub> treatment.

#### 4.3.2 Dependence of types of alcohols on nanographene crystallinity

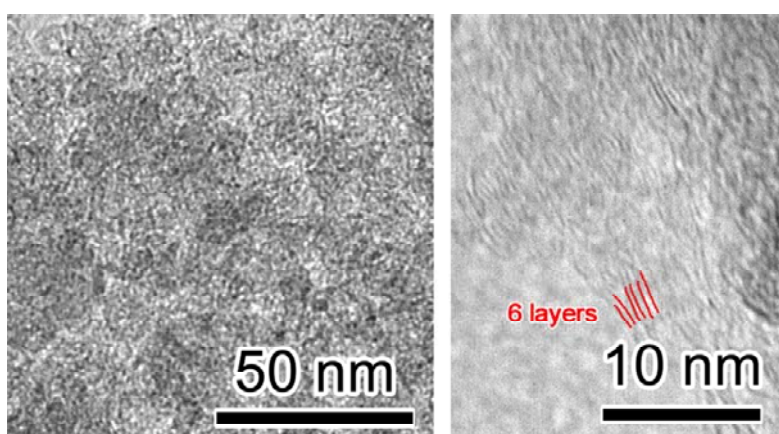
Collected solid samples were dispersed in the ethanol by the ultrasonication for TEM observation. Obtained TEM images are shown in Fig. 4.3. All samples had layers of film-like structures. The fringes were corresponded to graphene edges. The interlayer distance was estimated 0.33 to 0.36 nm. In the ethanol employed sample, approximately 10 to 30 nm ranged size grains were obtained. These grains have approximately 6 layers. From this result, the synthesized graphene had few layer nanographene. In the 1-butanol employing sample, many grains with size of approximately 10 nm were obtained. The number of layers was approximately 6 but the image was not clear compared to those of ethanol. More layers might exist. In the case of 1-hexanol, large and many layers containing crystals were synthesized. The number of layers was approximately 24. The sample contained over 100 nm size grain.

Raman scattering spectroscopy was carried out to evaluate crystallographic characters of nanographene. Figure 4.4 shows normalized Raman scattering spectra of synthesized nanographene. The peaks as D-, G-, D'- and 2D-band were detected at 1336, 1580, 1610, and 2670  $\text{cm}^{-1}$ , respectively. The synthesized nanographene had large domain to edge ratio. D-band intensity became large due to these edges. Therefore, the crystallinity of nanographene was evaluated from FWHM of G-band ( $\text{FWHM}_G$ ). Table 4.2 shows the estimated  $\text{FWHM}_G$ . The employing ethanol sample marked the smallest  $\text{FWHM}_G$  as 32.3  $\text{cm}^{-1}$ . The  $\text{FWHM}_G$  of the sample employed 1-butanol was 44.1  $\text{cm}^{-1}$ . The  $\text{FWHM}_G$  of 1-hexanol was 48.8  $\text{cm}^{-1}$ .  $\text{FWHM}_G$  increased with increasing carbon atoms number in unit molecule. Synthesized nanographene had the higher-crystallinity when smaller number of carbon atoms contained in unit molecule was employed. The domain size was calculated from the integrated intensities of G- and D-band ratio using

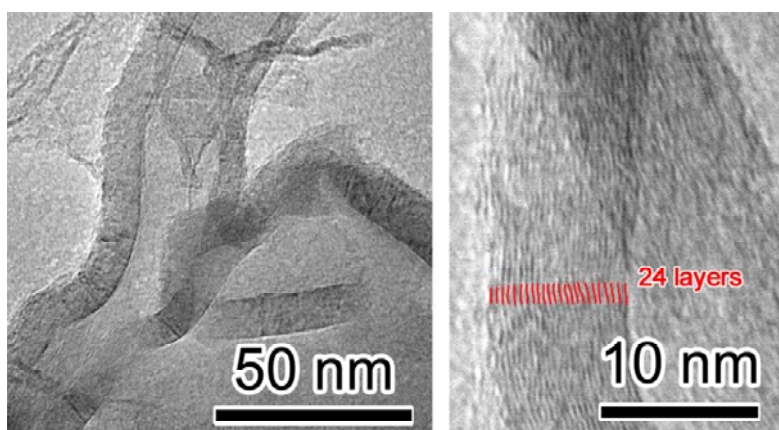
Eq. (2.20) [2]. Calculated domain sizes were shown in Table 4.2. The largest domain size was 11.9 nm which was remarked at the ethanol. Those of 1-butanol and 1-hexanol were smaller, 10.6 and 11.1 nm, respectively. The tendency of domain size change was similar to the synthesis rate. The 2D-band was originated in the graphene structure [3,4]. Comparison of 2D-band FWHM ( $\text{FWHM}_{2D}$ ) is shown in Table 4.2. The  $\text{FWHM}_{2D}$  increased with increasing carbon atoms number in unit molecule. When graphitization was progressed, The  $\text{FWHM}_{2D}$  was increased. Therefore, 1-hexanol synthesized the graphitic structure comparing with ethanol and 1-butanol.



(a)



(b)



(c)

Figure 4.3. TEM images of synthesized nanographenes (methanol couldn't synthesized any solid products). (a) Ethanol. (b) 1-Butanol. (c) 1-Hexanol.

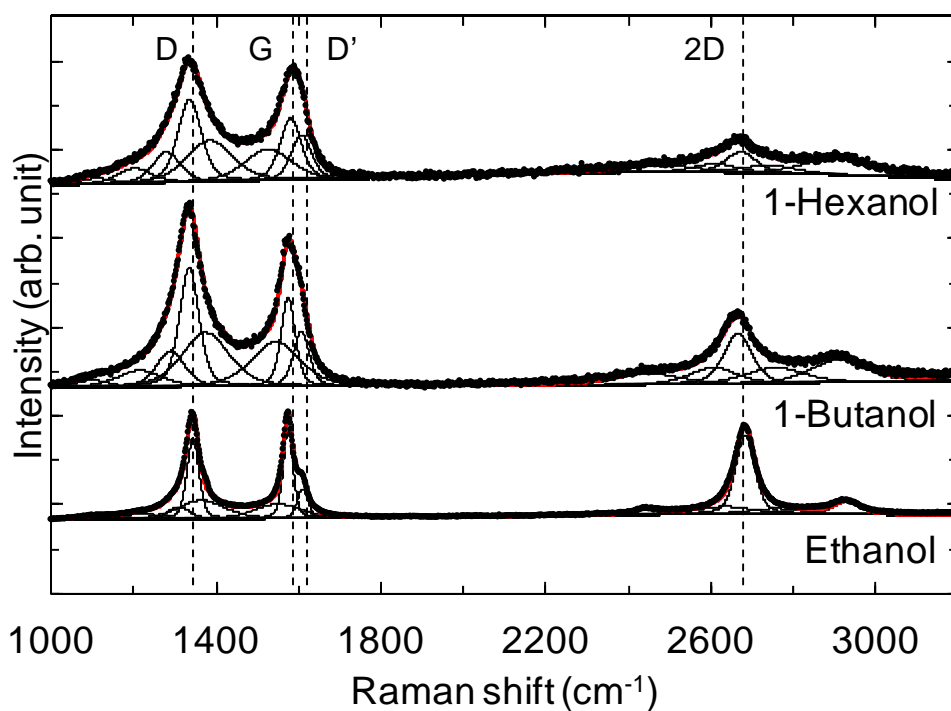


Figure 4.4. Raman scattering spectra of synthesized nanographene by in-liquid plasma employing alcohols.

Table 4.2. Estimated crystallographic properties of synthesized nanographene.

	$\text{FWHM}_G$ ( $\text{cm}^{-1}$ )	Domain size (nm]	$\text{FWHM}_{2D}$ ( $\text{cm}^{-1}$ )
Ethanol	32.3	11.9	67.0
1-Butanol	44.1	10.6	77.8
1-Hexanol	48.8	11.1	87.9

### 4.3.3 Optical diagnostics of the in-liquid plasma

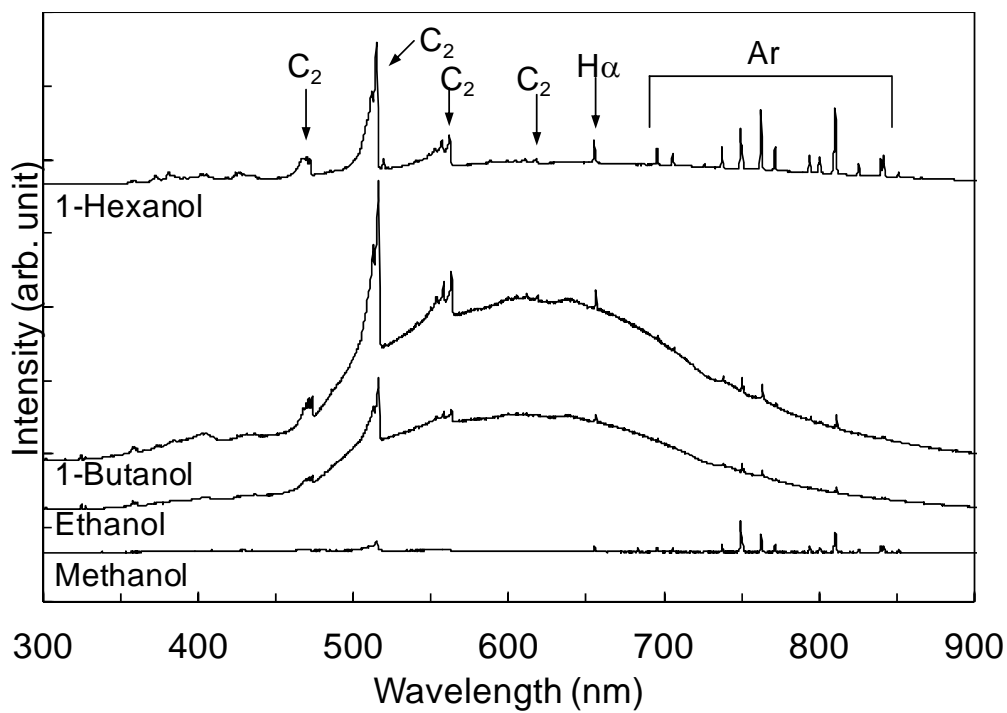
The in-liquid plasma has a basically pulse-like discharge waveform shown in Fig. 2.3(c). The discharge duration time was approximately 4 to 5 ms and the cycle time was approximately 8.3 ms. The exposure time of spectrometer detector was set at enough long comparing with the discharge duration. The intensities of spectra were divided by each exposure time.

Figure 4.5(a) shows raw optical emission spectra of in-liquid plasmas employing each alcohol. The emissions of C<sub>2</sub> Swan band, H $\alpha$ , and Ar were detected at all alcohols. Figure 4.6(b) is enlarged spectra in 300-500 nm region of Fig. 4.5(a). C<sub>2</sub> at 474.8 nm and some weak peaks could be seen in spectra. These peaks were weak in intensity and couldn't be assigned, but molecular emission at 431 nm might be CH. If OH emitted, it should appear at 309 nm, but only a very weak peak was observed in methanol and it couldn't be observed in other alcohols. In the UV region, the sensitivity of the spectrometer decreases due to its performance. It is difficult to identify the peak unless it is strong emission like C<sub>2</sub>. In the case of employing methanol, emission intensities of C<sub>2</sub> and H $\alpha$  were weak compared with other alcohols. Broad emissions were observed except for the methanol. The broad-emission was originated from the thermal radiation of synthesized carbon materials [5,6] heated in the in-liquid plasma or photons emitted when electrons collide with another particle and transmit to another state [5]. The temperature was estimated by thermal radiation from nanoparticles in Ref. [5,6]. Graphene emits light when heated [7]. From these facts, the thermal radiation was thought to be derived from nanographene and by-products in the in-liquid plasma. The temperature of the thermal radiation can be estimated from peak position of spectrum which was corrected by sensitivity of spectrometer using Eq. (3.2). Estimated

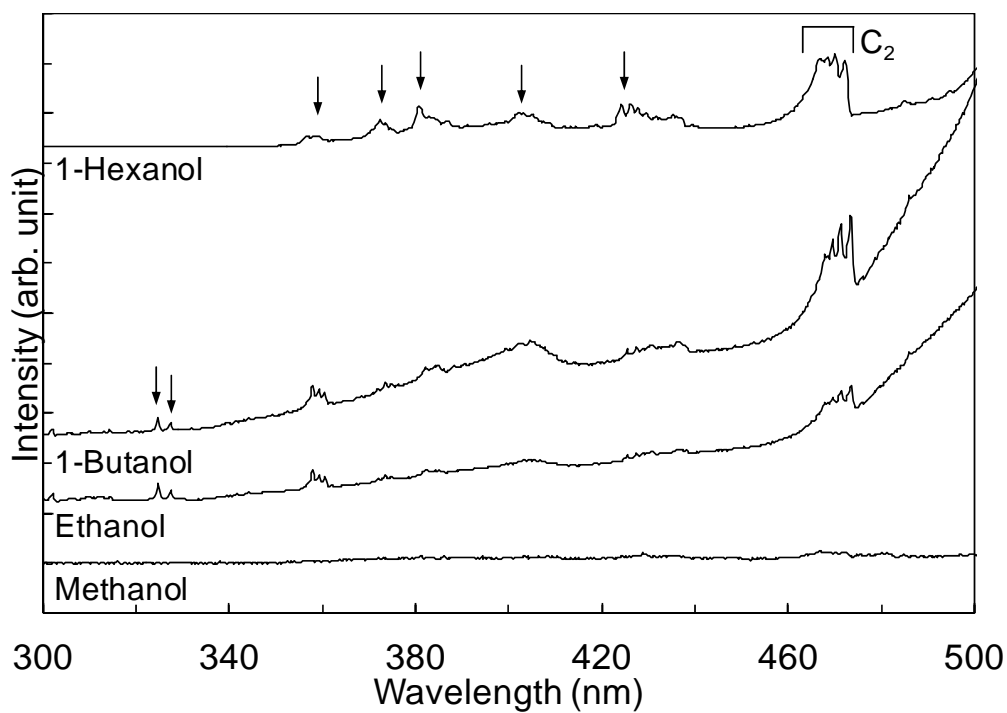
temperature ( $T$ ) is shown in Table 4.3.  $T$  was ranged from 4720 to 4800 K and decreased with increasing carbon atoms number in unit molecule but the range of change was small.

Broad background emissions were analyzed. Intensities of broad emission were different among ethanol, 1-butanol, and 1-hexanol. It was thought that this difference was caused by the synthesis rate and material liquids properties. Boiling point and vapor pressure might affect the gas phase of in-liquid plasma. Ethanol employed for the in-liquid plasma had the smallest synthesis rate. Boiling point and vapor pressure of ethanol show the tendency to be most easily vaporized. 1-Butanol had the highest synthesis rate and indicates second most easily vaporized. 1-Hexanol is the least volatile. It was thought that vaporized alcohol was supplied to the gas phase of the in-liquid plasma as the source of products. Therefore, the synthesis reactions also occurred same as the liquid phase.

Rotational temperature ( $T_r$ ) and vibrational temperature ( $T_v$ ) of  $C_2$  were estimated from  $C_2$  Swan band  $\Delta v = 0$  emissions using spectrum fitting. A fitted example is shown in Fig 4.6 and results are shown in Table 4.3.  $T_v$  and  $T_r$  increased with increasing carbon atoms number in unit molecule. In the case of employing ethanol,  $T_v$  and  $T_r$  were 1870 and 1770 K. In the case of employing 1-butanol,  $T_v$  and  $T_r$  were 2200 and 2070 K. In the case of employing 1-hexanol,  $T_v$  and  $T_r$  were 2130 and 2030 K.



(a)



(b)

Figure 4.5. Optical emission spectra of in-liquid plasma. (a) Wide range spectra.

(b) Enlarged spectra in 300-500 nm region of (a).

Table 4.3. Estimated  $T$ ,  $T_v$ , and  $T_r$ .

	$T$ (K)	$T_v$ (K)	$T_r$ (K)
Ethanol	4800	1870	1770
1-Butanol	4770	2200	2070
1-Hexanol	4720	2130	2030

Table 4.4. Physical properties of alcohol.

	Boiling point (°C)	Vapor pressure at 20 °C (kPa)
Ethanol	78.2	6.0
1-Butanol	117.7	0.8
1-Hexanol	157.0	0.1

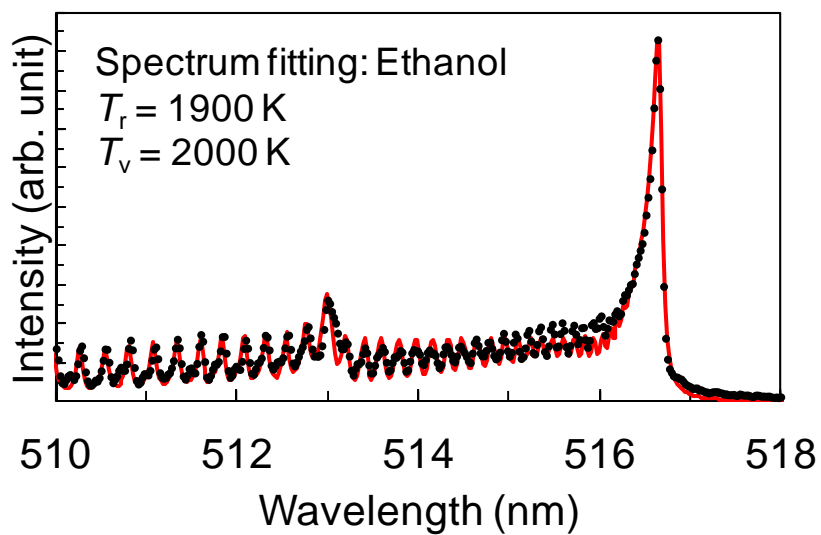
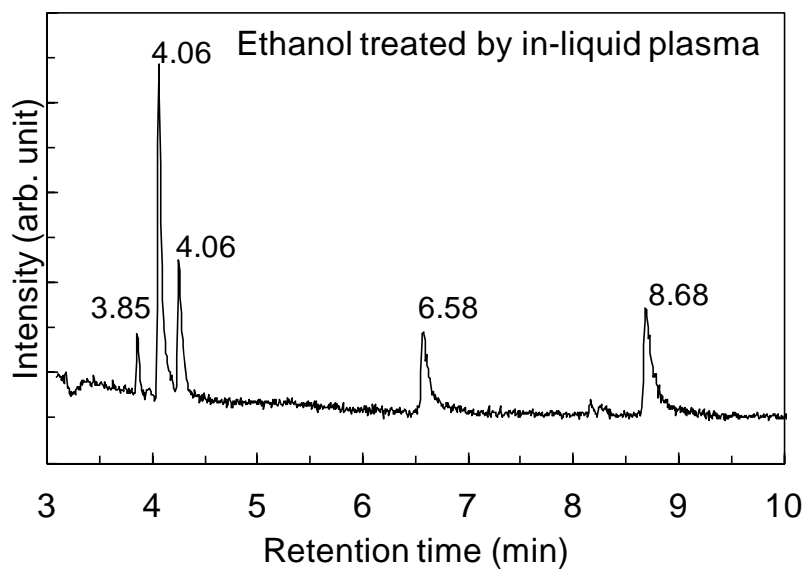


Figure 4.6. A example of spectrum fitting (ethanol). Solid circles are measured spectrum.

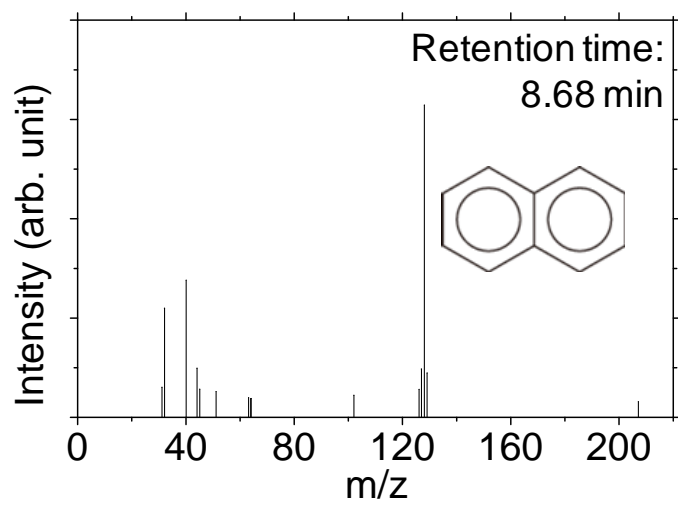
Red solid curve is calculated spectrum.

#### 4.3.4 Chemical components in the residual liquids

Filtered liquids, which were the alcohols treated by the in-liquid plasma, were analyzed by GC-MS to determine substances in liquids. Figure 4.7 shows the result of ethanol treated by in-liquid plasma. The parts of detected substances are shown in Table 4.5. The methanol treated by in-liquid plasma, any substances couldn't be detected. In the case of ethanol, the benzene ring included molecules were detected. These species seemed intermediates of nanographene. In the case of 1-butanol, benzene ring included structures and organic compounds without ring structures were detected. The 1-Butanol has longer carbon chain than the ethanol. Therefore, the 1-butanol that was not decomposed to C<sub>2</sub> might generate such organic compounds. In the case of 1-hexanol, benzene ring, six-, and five-membered ring carbon structures were detected. Organic compounds without ring structures were also detected. Longer carbon chain of 1-hexanol induced these species. The naphthalene (retention time: 8.68 min, m/z: 128) was detected at all alcohols except for the methanol.



(a)



(b)

Figure 4.7. Chromatogram of in-liquid plasma treating ethanol and mass spectrum at retention time 8.68 min.

Table 4.5. Detected substances from residual liquids.

Retention time (min)	m/z	Material liquid (Matching Quality)			Formula	Structure
		Ethanol	1-Butanol	1-Hexanol		
4.06	102	✓ (91)	✓ (60)		$C_8H_6$	
4.11	130		✓ (78)		$C_8H_{18}O$	
4.25	104	✓ (68)	✓ (81)		$C_8H_8$	
4.78	128		✓ (87)		$C_8H_{16}O$	
4.82	116			✓ (78)	$C_7H_{16}O$	
5.13	84			✓ (58)	$C_6H_{12}$	
5.53	128			✓ (64)	$C_8H_{16}O$	
5.75	144		✓ (83)		$C_8H_{16}O_2$	
5.90	130			✓ (83)	$C_8H_{18}O$	
6.58	116	✓ (90)	✓ (90)		$C_9H_8$	
8.68	128	✓ (91)	✓ (91)	✓ (91)	$C_{10}H_8$	
8.76	170			✓ (95)	$C_{11}H_{24}$	

#### 4.3.5 Discussion: Nanographene synthesis in the in-liquid plasma

The synthesis rates and crystallinities of nanographene were different at each alcohol. Methanol couldn't synthesize nanographene. More than two carbon atoms in unit molecule are necessary to synthesize nanographene. Synthesis rate was increased at 1-butanol and 1-hexanol compared with the ethanol as shown in Fig. 4.2. Difference between 1-butanol and 1-hexanol was small. There were complicate relationships between structures of alcohol and synthesis rate.

The  $FWHM_G$  shown in Table 4.2 increased with increasing carbon atoms number in unit molecule. This tendency was caused by material molecule configurations. Smaller molecular mass alcohol as ethanol could synthesize the highly-crystalline nanographene. In addition, the alcohol with large molecular mass tended to be graphitized, and the  $FWHM_{2D}$  was broadened. Larger molecular mass alcohol employed for the in-liquid plasma synthesized nanographite-like structures rather than nanographene.

The broadened emissions obtained by OES shown in Fig. 4.5 were originated from the thermal radiation of synthesized carbon materials. The estimated temperature shown in Table 4.3 was approximately 4800 K at the ethanol. Higher temperature supported the crystal formation.

Individual emission peaks as  $C_2$  Swan band,  $H\alpha$  and Ar were detected but elements from electrodes were not detected. This point was different from the DC arc plasma for SWNTs synthesis. In the case of DC arc plasma, anode electrode is heated by electron collision. On the other hand, in-liquid plasma was intermittently generated. The in-liquid plasma is driven by the AC high voltage and the discharge duration time is approximately 4 to 5 ms. High temperature time is short and modulated sinusoidal

voltage inhibits charged particles collision to electrodes. Therefore, electrodes are hardly evaporated on in-liquid plasma. In methanol,  $C_2$ ,  $H\alpha$ , and Ar emissions intensities were weak comparing to other alcohols.  $C_2$  and  $H\alpha$  originated from alcohol.  $C_2$  was one of carbon sources to grow nanographene.  $T_v$  and  $T_r$  of  $C_2$  became the lowest at the ethanol. In the case of ethanol, it was considered that  $C_2$  was generated with lower energy compared to other alcohols.  $C_2$  with high energy had a potential to collide and destroy crystal structures. In the case of higher  $T_v$  and  $T_r$  observed as employing 1-butanol and 1-hexanol, the collision of  $C_2$  to formed crystal structure induced lattice defects. It is thought that  $C_2$  has played important roles to grow the graphene structures [8-10].

The residual liquid included by-products or intermediates and they were analyzed by GC-MS as shown in Table 4.5. In the case of employing methanol, they were only detected. Methanol was hardly changed by the in-liquid plasma. In the case of employing ethanol, benzene ring contained structures were detected. Ethanol may easily generate  $C_2$  due to its molecular structure which has two carbon atoms. Therefore, ethanol employed for the in-liquid plasma is easy to form graphene structures with the help of high temperature. In the case of employing 1-butanol or 1-hexanol, in addition to benzene ring contained structures, substances having chained or branched carbon were detected. These substances were generated due to material alcohols with relatively complicated structures comparing to the ethanol.

Figure 4.8 shows an example of possible reaction path of 1-butanol. During the in-liquid plasma irradiation, the 1-butanol was dehydrated or dissociated and generates free radicals. Alcohol with dangling bonds causes  $\beta$ -scission to produce ethylene and ethyl radicals. These substances were dehydrated by plasma or hydroxyl radical and  $C_2$  radicals were generated. The  $C_2$  radicals form crystalline structure in high temperature

region. Then, the edges or arisen amorphous structures are etched by hydroxyl radicals [11]. The former leads decreasing crystallinity and the latter supports the crystal growth.  $C_2$  is easily generated from the ethanol dissociation due to its molecular structure constructed from two carbon atoms. On the other hand, the 1-butanol has potential to generate two  $C_2$  radicals via single  $\beta$ -scission. This is one of reasons why the synthesis rate increase. However, longer carbon chain structures in alcohol molecules induce by-products. Alcohol with dangling bond bonds other radicals. Alcohols combine with other materials to form complex molecules.

Both high crystallinity and high synthesis rate were achieved by the condition of large amounts of  $C_2$  with low temperatures.

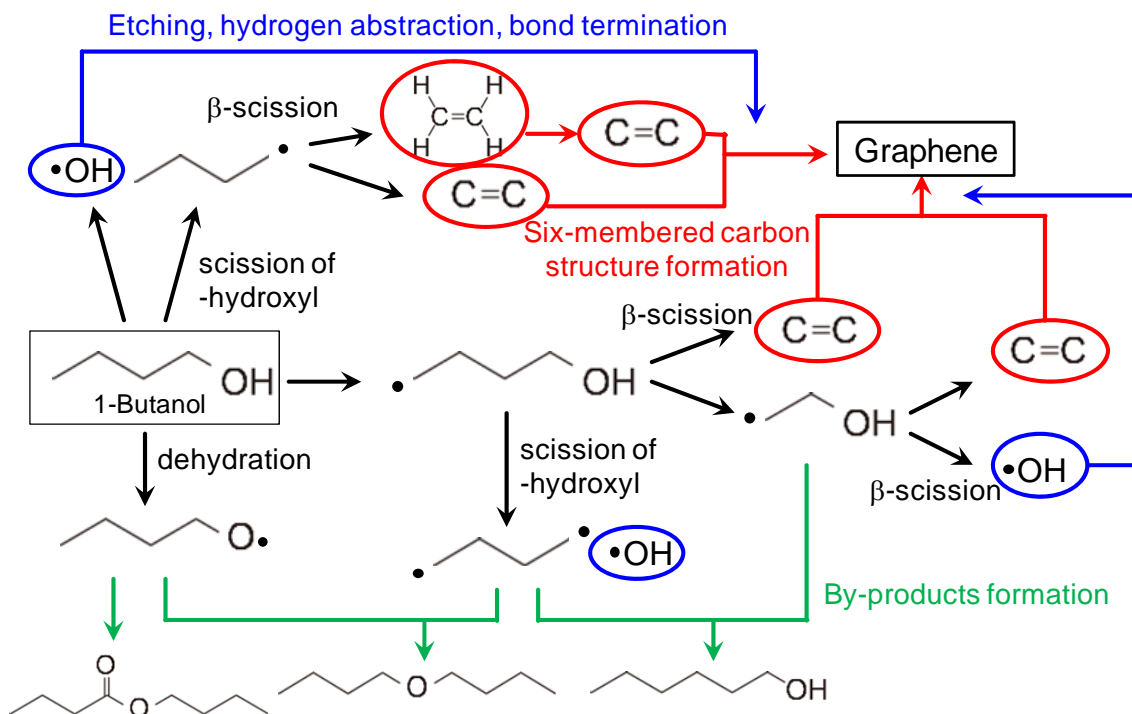


Figure 4.8. Possible pathways of nanographene formation from 1-butanol.

#### 4.4 Conclusion of chapter 4

The OES measurements of the in-liquid plasma employing alcohols were carried out to investigate a relationship between active species in in-liquid plasma region and crystallinity of the synthesized nanographene. Residual liquids, which were filtered after in-liquid plasma treatment of alcohols, were analyzed by the gas-chromatography mass-spectrometry (GC-MS) to estimate components.

Methanol employed for the in-liquid plasma couldn't synthesize any solid products. Synthesis rate of ethanol employed for the in-liquid plasma was 0.17 mg/min. 1-butanol and 1-hexanol synthesized nanographene in approximately 3 times larger rate. There was no big difference in the synthesis rate of 1-butanol and 1-hexanol. Synthesized nanographene had layered structures. The domain sizes were approximately ten several to several ten nanometer. In the case of employing 1-hexanol, several ten nanometers and over twenty layered structures were synthesized. These interlayer spaces were almost the same at 0.35 nm which was similar value of the graphene layer in graphite, 0.34 nm. Crystalline characterization was carried out by Raman scattering spectroscopy. Crystallinity was estimated from  $FWHM_G$ . Crystallinity decreased with increasing number of carbon atoms in unit molecule. Ethanol marked the largest domain size. In addition,  $FWHM_{2D}$  were broadened with increasing carbon atoms number. In 1-hexanol, it was thought that synthesized materials were nanographite-like structures.

Optical emission lines of  $C_2$  Swan band,  $H\alpha$  and Ar were detected at all conditions but methanol had weak intensities. Broad emissions were overlapped except for the methanol. These emissions were considered to blackbody radiation.  $T_v$  and  $T_r$  of  $C_2$  became the smallest at ethanol and blackbody temperature was the lowest. High temperature supported highly crystalline nanographene and high temperature  $C_2$

disturbed crystal formations.

Residual liquids included intermediates and by-products except for the methanol. Ethanol had the benzene ring structure included molecules. 1-butanol and 1-hexanol had chained and branched carbon included molecules besides these molecules. Ethanol can easily generate  $C_2$  due to its molecular structure. 1-Butanol can generate two  $C_2$  on the simple scheme. Therefore,  $C_2$  has played important roles to form the graphene structure and the large amount of  $C_2$  increases the synthesis rate.

In order to realize the high crystallinity and the high synthesis rate, it is necessary to generate  $C_2$  efficiently, and to set the temperature of reaction region high.

## References

- [1] T. Hagino, H. Kondo, K. Ishikawa, H. Kano, M. Sekine, and M. Hori, “Ultrahigh-Speed Synthesis of Nanographene Using Alcohol In-Liquid Plasma” *Appl. Phys. Express* **5**, 035101 (2012).
- [2] L. G. Cançado, K. Takai, T. Enoki, M. Endo, Y. A. Kim, H. Mizusaka, A. Jorio, L. N. Coelho, R. Magalhães-Paniago, and M. A. Pimenta, “General equation for the determination of the crystallite size  $L_a$  of nanographite by Raman spectroscopy” *Appl. Phys. Lett.* **88**, 163106 (2006).
- [3] R. P. Vidano, D. B. Fishbach, L. J. Willis, and T. M. Loehr, “OBSERVATION OF RAMAN BAND SHIFTING WITH EXCITATION WAVELENGTH FOR CARBONS AND GRAPHITES” *Solid State Commun.* **39**, pp.341-344 (1981).
- [4] E. J. Heller, Y. Yang, L. Kocia, W. Chen, S. Fang, M. Borunda, and E. Kaxiras, “Theory of Graphene Raman Scattering” *J. Am. Chem. Soc.* **10**, pp.2803-2818 (2016).
- [5] S. S. Harilal, N. Farid, A. Hassanein, and V. M. Kozhevnikov, “Dynamics of femtosecond laser produced tungsten nanoparticle plumes” *J. Appl. Phys.* **114**, 203302 (2013).
- [6] A. Mohanta, B. Lanfant, M. Asfaha, and M. Leparoux, “Optical emission spectroscopic study of Ar/H<sub>2</sub>/CH<sub>4</sub> plasma during the production of graphene nano-flakes by induction plasma synthesis” *J. Phys. Conf. Ser.* **825**, 012010 (2017).
- [7] T. Matsumoto, T. Koizumi, Y. Kawakami, K. Okamoto, and M. Tomita, “Perfect blackbody radiation from a graphene nanostructure with application to high-temperature spectral emissivity measurements” *Optics Express* **21**, pp.30964-30974 (2013).
- [8] F. Müller, H. Sachdev, S. Hüfner, A. J. Pollard, E. W. Perkins, J. C. Russell, P. H. Beton, S. Gsell, M. Fischer, M. Schreck, and B. Stritzker, “How Does Graphene Grow? Easy Access to Well-Ordered Graphene Films” *small* **5**, pp.2291-2296 (2009).
- [9] K. Teii, S. Shimada, M. Nakashima, and A. T. H. Chuang, “Synthesis and electrical characterization of *n*-type carbon nanowalls” *J. Appl. Phys.* **106**,

084303 (2009).

- [10] S. Mori, T. Ueno, and M. Suzuki, "Synthesis of carbon nanowalls by plasma-enhanced chemical vapor deposition in a CO/H<sub>2</sub> microwave discharge system" *Diam. Relat. Mater.* **20**, pp.1129-1132 (2011).
- [11] G. Zhao, D. Shao, C. Chen, and X. Wang, "Synthesis of few-layered graphene by H<sub>2</sub>O<sub>2</sub> plasma etching of graphite" *Appl. Phys. Lett.* **98**, 183114 (2011).

## **Chapter 5. Effects of carbon-sources on nanographene synthesis: A comparison between hydrocarbons and alcohols**

### 5.1 Backgrounds of this study

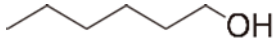
In the case of other types of in-liquid plasma, alkane or benzene was used to synthesize carbon nanomaterials [1-5]. Therefore, employing benzene as material has a potential to improve synthesis rate. *n*-Hexane and benzene were verified as possible raw materials. The difference between hydrocarbons and alcohol is whether hydroxyl group is included or not. Hydroxyl group roles could be investigated by comparing results of alcohols with hydrocarbons. In this study, optical emission spectroscopy (OES), Raman scattering spectroscopy, and GC-MS were carried out to investigate the synthesis mechanism of nanographene by the in-liquid plasma employing various liquids.

### 5.2 Experimental setup

#### 5.2.1 In-liquid plasma synthesis of nanographene

Synthesis methods were the same as chapter 4.1 except for employing materials. Employed material liquids were ethanol ( $C_2H_5OH$ ), 1-hexanol ( $C_6H_{13}OH$ ), *n*-hexane ( $C_6H_{14}$ ), and benzene ( $C_6H_6$ ). Synthesis time was 1, 3, and 5 min. 10 min was too long because liquids rapidly decreased during in-liquid plasma irradiation in *n*-hexane and benzene. Synthesized nanographene was filtered by 1  $\mu$ m-pore-size filter (Merck Omnipore JAWP04700). Filtered nanographene was treated using 30 %  $H_2O_2$  water at 120°C on 120 min. The conditions were summarized in Table 5.1.

Table 5.1. Experimental conditions.

Applying voltage	8 kV	
Electrodes	SUS	
Gas	Ar, 3 slm	
Processing time	1, 3, 5 min	
Alcohol	Ethanol (C <sub>2</sub> H <sub>5</sub> OH)	
	1-Hexanol (C <sub>6</sub> H <sub>13</sub> OH)	
	<i>n</i> -Hexane (C <sub>6</sub> H <sub>14</sub> )	
	Benzene (C <sub>6</sub> H <sub>6</sub> )	
Filter	1 μm pore	
Treatment	H <sub>2</sub> O <sub>2</sub> water (30%), 120 min 120 °C	

## 5.2.2 Analysis of the synthesized nanographene

Obtained nanographenes were analyzed by transmission electron microscope (TEM) and Raman scattering spectroscopy. Filtered samples were dispersed by ultrasonication into ethanol to be observed by TEM (JEOL JEM2010). The morphologies of synthesized samples were compared between alcohols and hydrocarbons. Crystallographic analysis was carried out by Raman scattering spectroscopy (Renishaw InVia Reflex; 532 nm of excitation). Nanographenes were synthesized by in-liquid plasmas employing hydrocarbons Raman scattering spectra similar to alcohols were detected. Obtained spectra of nanographene synthesized using hydrocarbons were compared with alcohols.

## 5.3 Results and discussion

### 5.3.1 Crystallographic analysis of nanographene synthesized by the in-liquid plasma

Dramatic changes were observed in the synthesis rate on employing hydrocarbons. Figure 5.1 shows synthesis amounts of H<sub>2</sub>O<sub>2</sub> treated solid products. The synthesis rate at the in-liquid plasma employing benzene dramatically increased compared to alcohols. The synthesis rate at benzene was 6.98 mg/min which was approximately 40 times larger than ethanol of 0.17 mg/min. The synthesis rate at the *n*-hexane employed for the in-liquid plasma was 0.73 mg/min. The synthesis rate of the *n*-hexane was 1.7 times larger than that of 1-hexanol which was 0.42 mg/min. In addition, the *n*-hexane employed for the in-liquid plasma generated dark solid products not only the liquid phase but also the gas phase. The soot was formed at the internal wall of the glass chamber, the chamber cap, and the outside of chamber. These products were

generated at the gas phase. *n*-Hexane has relatively a high vapor pressure of 17.6 kPa. Vapor pressure and boiling point are shown in Table 5.2. Vaporized *n*-hexane existed in large amount which were reacted by the gas phase part of in-liquid plasma.

In early stage, products generated at the gas phase were isolated. These products moved to the chamber wall, cap, and outside via space between chamber and cap by the Ar gas flow. In this stage, products formed soot. These products were not collected, i.e., synthesis amount at only the liquid phase. In the case of employing benzene, the synthesis rate became extremely high. Benzene also produced solid products at both gas and liquid phases. Vapor pressure of benzene is 12.7 kPa.

Figure 5.2 shows TEM images of synthesized products by each liquids employed for the in-liquid plasma. *n*-Hexane employed for the in-liquid plasma synthesized layered and screw-shaped nanographene shown in Fig. 5.2(a). The number of layers was approximately 15. In the case of employing benzene, layered structures were observed shown in Fig. 5.2(b). The structure had 12 layers but the image became unclear at the edge of the grain and might be constructed by more layers. The inter layer spaces of *n*-hexane and benzene were 0.35 and 0.32 nm, respectively.

Figure 5.3 shows Raman scattering spectra of synthesized products. All spectra had D-, G-, D', and 2D-bands. In the spectra of alcohols, 2D-bands could be clearly seen. In contrast, 2D-bands of *n*-hexane and benzene were weaker and broader than those of alcohols. Table 5.3 shows the  $\text{FWHM}_G$  and domain size at each product. The  $\text{FWHM}_G$  of *n*-hexane was  $55.3 \text{ cm}^{-1}$  which was larger than 1-hexanol. The 1-hexanol employed for the in-liquid plasma synthesized the lowest crystallinity that of nanographene in all alcohols. Benzene  $\text{FWHM}_G$  was the broadest,  $61.3 \text{ cm}^{-1}$ , in all employed liquids. Hydrocarbons synthesized lower crystalline nanographene comparing to alcohols. In

addition, FWHM<sub>2D</sub> of *n*-hexane and benzene were 93.4 and 123.7 cm<sup>-1</sup>, respectively. These values were very large comparing to those of alcohols. Therefore, the graphitization was progressed at hydrocarbons in the nanographene synthesis processes by in-liquid plasmas. The results indicated that synthesized materials included nanographenes with several ten layers. It was considered that the increase of nanographenes with several ten layers ratios in the products induced the 2D-bands broadening.

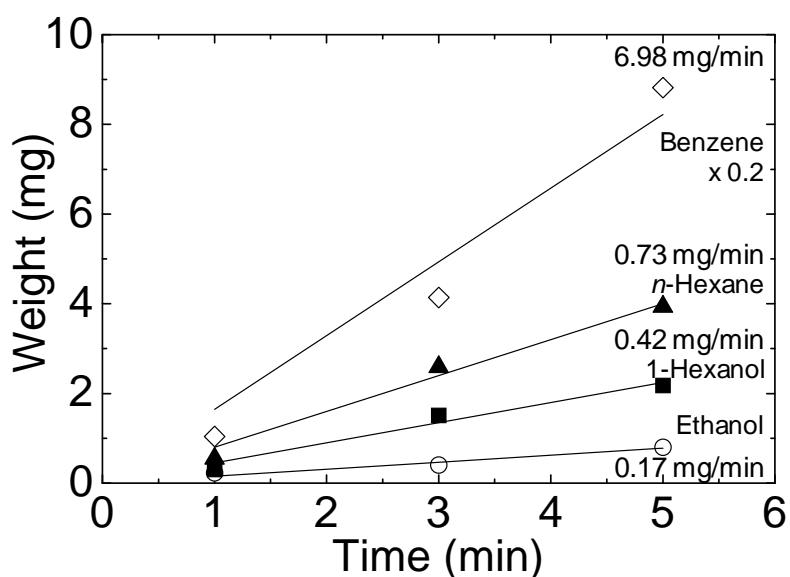
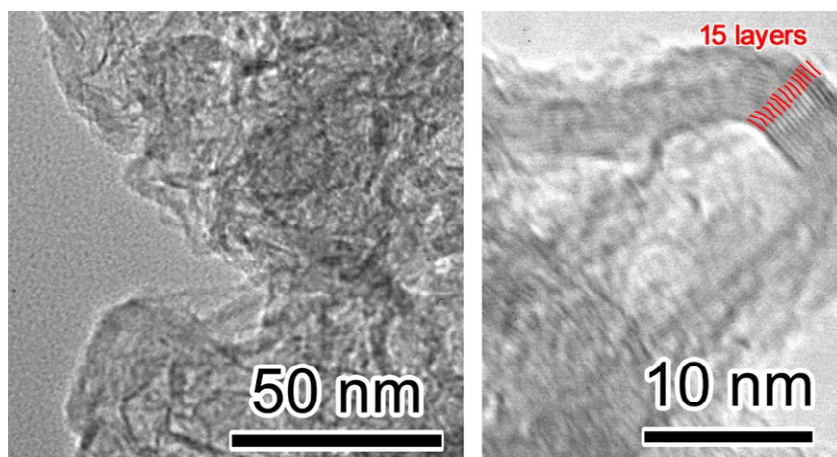


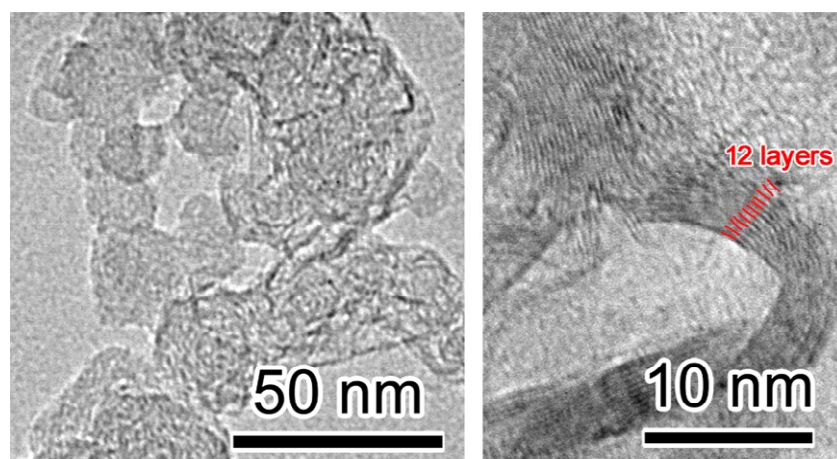
Figure 5.1. Synthesis amounts of solid products by in-liquid plasma.

Table 5.2. Physical properties of used liquids

	Vapor pressure @ 20 °C (kPa)	Boiling point (°C)
Ethanol	6.0	78.2
1-Hexanol	0.1	157.0
<i>n</i> -Hexane	17.6	68.8
Benzene	12.7	80.1



(a)



(b)

Figure 5.2. TEM images of synthesized nanographene. (a) In-liquid plasma employing n-hexane. (b) In-liquid plasma employing benzene.

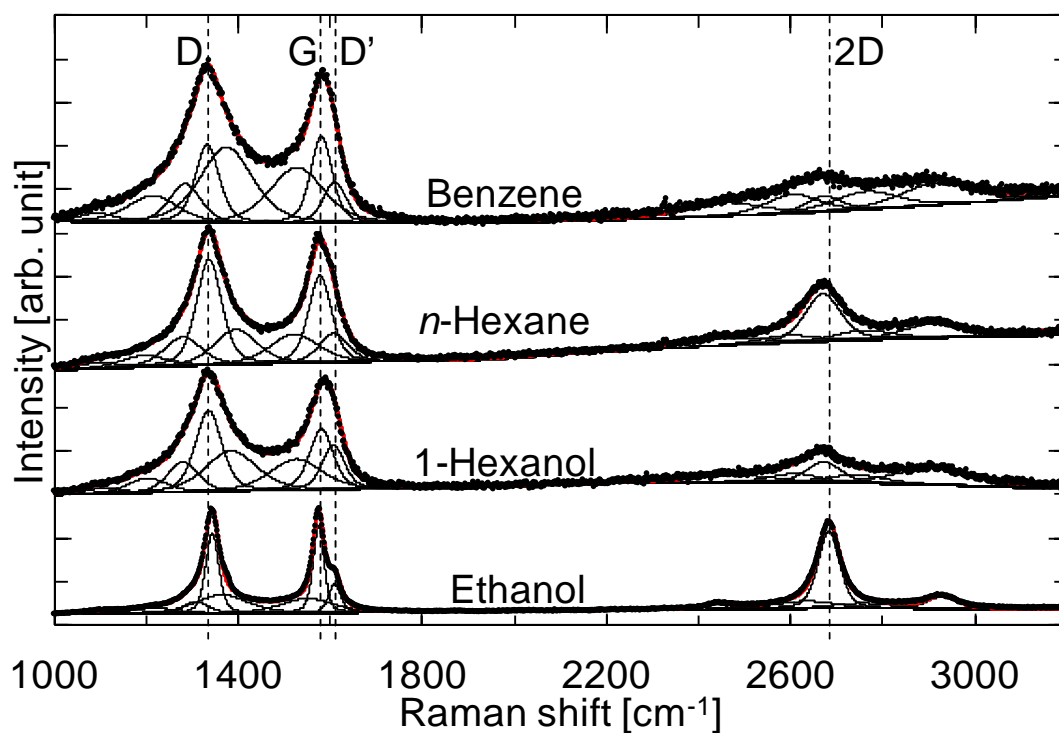


Figure 5.3. Raman scattering spectra of synthesized nanographene.

Table 5.3. Results of Raman scattering spectroscopy.

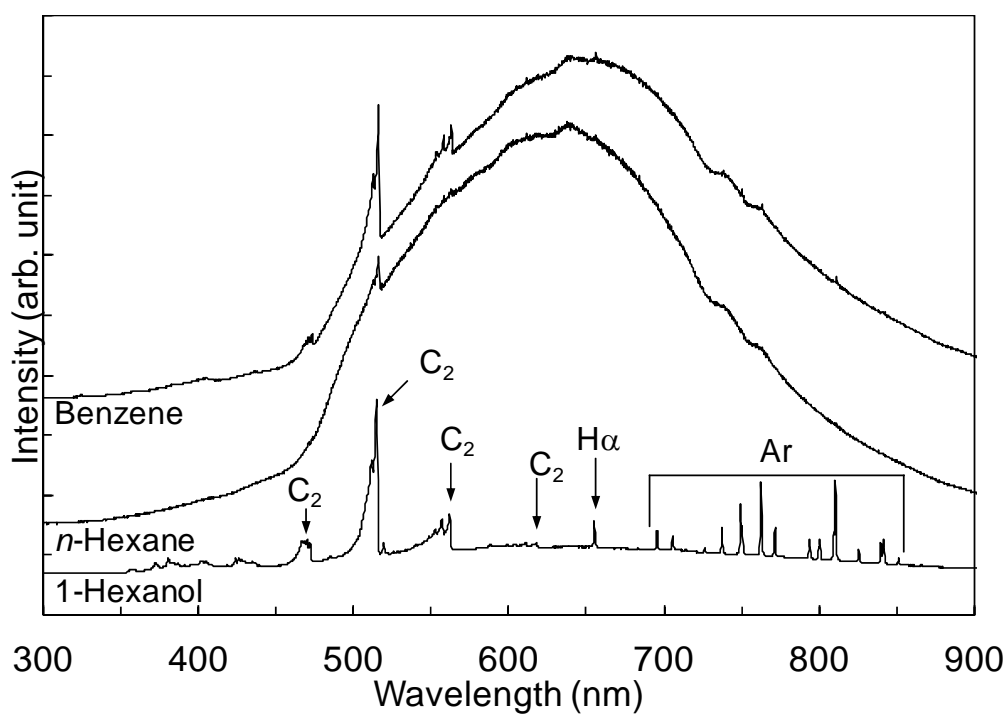
	$\text{FWHM}_G$ ( $\text{cm}^{-1}$ )	Domain size (nm)	$\text{FWHM}_{2D}$ ( $\text{cm}^{-1}$ )
Ethanol	32.1	11.9	67.0
1-Hexanol	48.8	11.1	87.9
<i>n</i> -Hexane	55.3	12.7	93.4
Benzene	61.3	12.5	123.7

### 5.3.2 Optical diagnostics of the in-liquid plasma

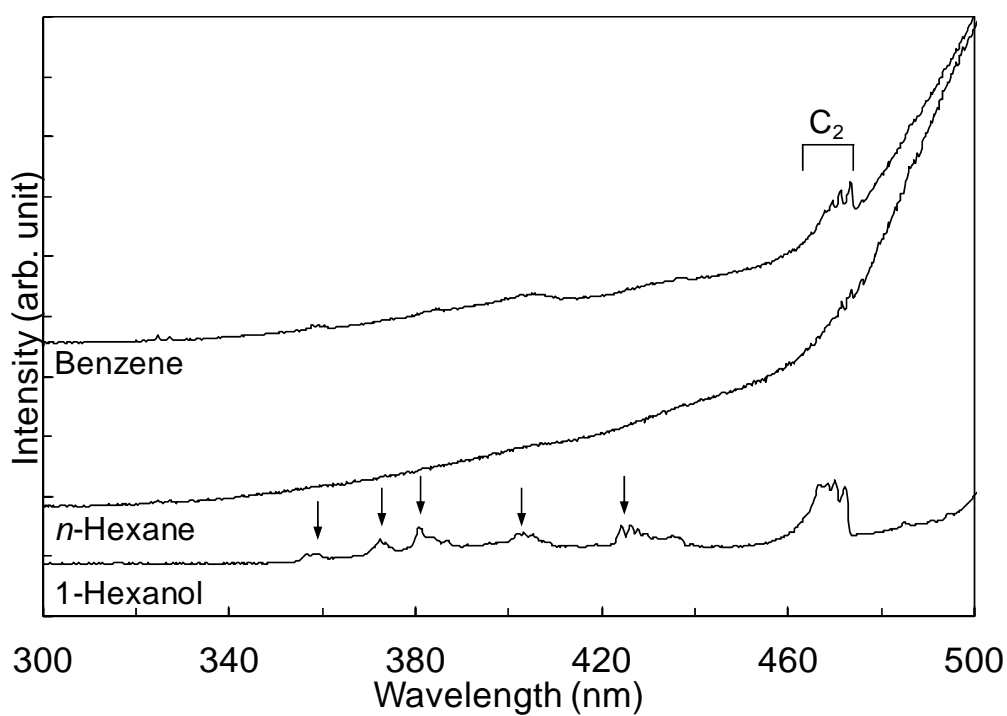
Measured optical emission spectra are shown in Fig. 5.4. 1-Hexanol had C<sub>2</sub> Swan band, H $\alpha$ , and Ar emission lines, and blackbody radiation which were overlapped. On the other hand, the *n*-hexane had only very weak C<sub>2</sub> emissions of excited species but the blackbody radiation was stronger than that of 1-hexanol. In the case of benzene employed for the in-liquid plasma, C<sub>2</sub> Swan band emissions were clearly seen and weak H $\alpha$  and Ar emissions were also detected. Figure 5.4(b) shows enlarged spectra at 300-500 nm region of Fig 5.4(a). C<sub>2</sub> emissions at 474.8 nm were detected except for the *n*-hexane. Several weak peaks could be seen in 1-hexanol. The blackbody radiation of benzene was stronger than that of *n*-hexane. The blackbody radiation intensity increased in an order of 1-hexanol, *n*-hexane, and benzene. The radiation of blackbody originated from synthesized nanomaterials in in-liquid plasma and its intensity depended on amounts of nanomaterials. Moreover, the vapor pressure and the boiling point of the alcohol affected the gas phase part of in-liquid plasma. The liquid with the higher vapor pressure and the low boiling point determine the characteristics of the vaporized liquid near the liquid surface, the vaporized liquid rich atmosphere is formed and it is reacted by the in-liquid plasma. This phenomenon was confirmed at *n*-hexane or benzene in the plasma conditions which had the soot at the gas phase. These volatile liquids employed for the in-liquid plasma can synthesize nanomaterials not only in the liquid phase but also in the gas phase.

Blackbody temperature was estimated by Wien's displacement law.  $T_v$  and  $T_r$  of C<sub>2</sub> were calculated by spectra fitting of C<sub>2</sub>  $\Delta v = 0$  emissions. The calculated results were shown in Table 5.4.  $T$  of hydrocarbons was lower than alcohols. In hydrocarbons, it was thought that the input power was used for heating.  $T_v$  and  $T_r$  of C<sub>2</sub> were higher at

hydrocarbons comparing to alcohols. In hydrocarbons,  $C_2$  efficiently absorbed and kept the input power comparing to alcohols.



(a)



(b)

Figure 5.4. Optical emission spectra of in-liquid plasma employing each liquid. (a) Wide range spectra. (b) Enlarged spectra in 300-500 nm region of (a).

Table 5.4. Estimated  $T$ ,  $T_v$ , and  $T_r$ .

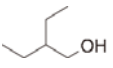
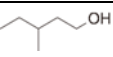
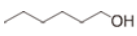
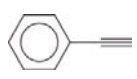
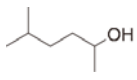
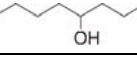
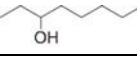
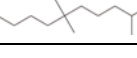
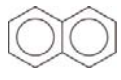
	$T$ (K)	$T_v$ (K)	$T_r$ (K)
Ethanol	4820	1870	1770
1-Hexanol	4710	2130	2030
<i>n</i> -Hexane	4630	2480	2270
Benzene	4510	2270	2130

### 5.3.3 Intermediates and by-products in the residual liquids after filtration of solid materials

Alcohols by the irradiation of the in-liquid plasma irradiated changed to be a yellowish liquid. Hydrocarbons also changed liquids color but their colors were very dark comparing to alcohols. Table 5.5 shows GC-MS results for substances detected from 1-hexanol, *n*-hexane, and benzene treated by in-liquid plasma. Treated *n*-hexane included O atom contained molecules. O atoms did not exist during the in-liquid plasma treatment. Therefore, O atoms were bonded by oxidation after the treatment. In addition, treated *n*-hexane included larger types of benzene rings contained molecules. In the case of 1-hexanol, when the molecular structure was dissociated by in-liquid plasma, OH radical generated from carbon chain end of molecule. OH radicals induced dehydration reactions. Yielded dangling bond induced  $\beta$ -scission reactions. The fragmentized 1-hexanol formed short-carbon chain molecules. These molecules were bonded and formed branching molecules. The branching molecules and the short-carbon chains might become core of the benzene rings, e.g., 2-ethyl-1-butanol [C<sub>6</sub>H<sub>13</sub>OH] (retention time: 3.52 min) can form to benzene ring with C<sub>2</sub>. Figure 5.5 shows an example of possible pathway of nanographene formation from 1-hexanol. 1-Hexanol generates C<sub>2</sub> easily via  $\beta$ -scission due to dehydration reactions of oxygen species. On the other hands, the *n*-hexane has no hydroxyl group. Figure 5.6 shows an example of possible pathway of nanographene formation from *n*-hexane. Dehydration reactions occurred by only plasma. *n*-Hexane does not fit to form short carbon chain such as C<sub>2</sub> radicals. In the case of Benzene, all detected substances had carbon ring structures. Benzene ring with carbon chain such as phenylethyne [C<sub>8</sub>H<sub>6</sub>] (retention time: 4.06 min) is constructed from the dehydrated benzenes and C<sub>2</sub> radicals. Figure 5.7 shows an example of possible pathway of graphene

formation from benzene. The benzene was hardly fragmentized because  $\beta$ -scission was not induced due to its ring structure. Dangling bond on benzene easily bonded to other benzenes with dangling bonds and formed large-carbon rings structures.

Table 5.5. Detected substances in treated liquids.

Retention time (min)	m/z	Material liquid (Matching quality)			Formula	Structure
		1-Hexanol	<i>n</i> -Hexane	Benzene		
3.52	102	✓(83)	✓(83)		C <sub>6</sub> H <sub>13</sub> OH	
3.58	102	✓(53)	✓(86)		C <sub>6</sub> H <sub>13</sub> OH	
3.93	102	✓(83)	✓(83)		C <sub>6</sub> H <sub>13</sub> OH	
4.06	102		✓(91)	✓(91)	C <sub>8</sub> H <sub>6</sub>	
4.99	116	✓(78)			C <sub>7</sub> H <sub>15</sub> OH	
5.90	130	✓(72)			C <sub>8</sub> H <sub>17</sub> OH	
5.98	130	✓(83)			C <sub>8</sub> H <sub>17</sub> OH	
7.01	184	✓(64)			C <sub>13</sub> H <sub>28</sub>	
7.27	156	✓(95)	✓(95)		C <sub>11</sub> H <sub>24</sub>	
8.68	128	✓(91)	✓(91)	✓(90)	C <sub>10</sub> H <sub>8</sub>	

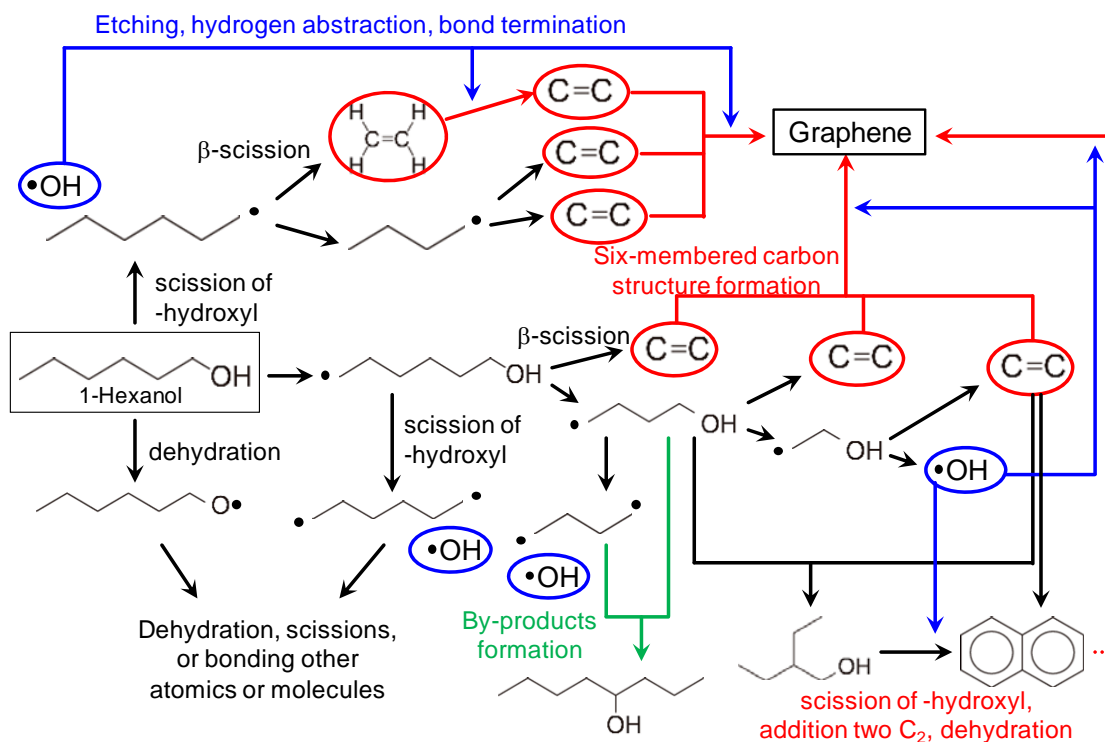


Figure 5.5. Schematic diagram of possible pathway of nanographene formation from 1-hexanol by in-liquid plasma.

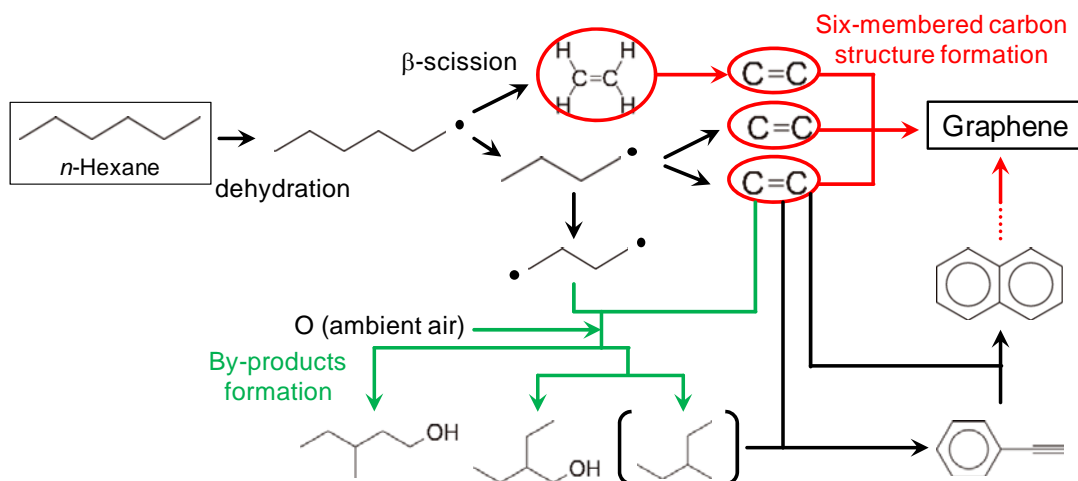


Figure 5.6. Schematic diagram of possible pathway of nanographene formation from n-hexane by in-liquid plasma.

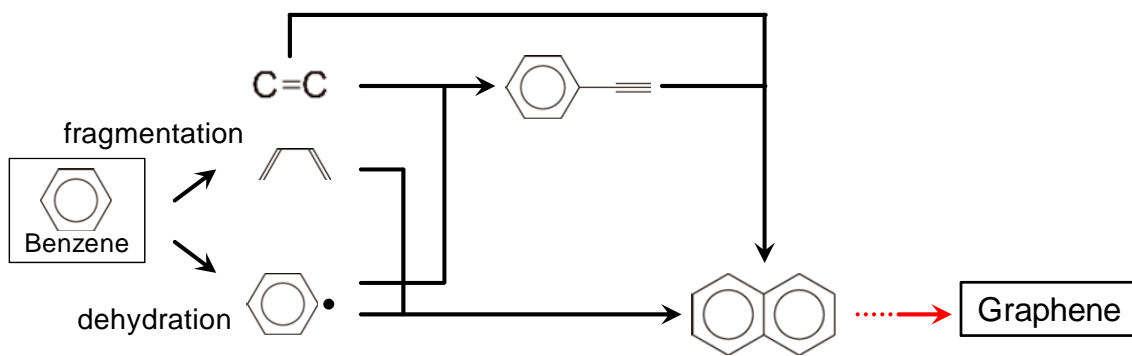


Figure 5.7. Schematic diagram of possible pathway of nanographene formation from benzene by in-liquid plasma.

#### 5.3.4 Discussion: Nanographene synthesis reactions taken into accounts of alcohols and hydrocarbons employment results

Hydrocarbons precursors improved the synthesis rate of solid materials as shown in Fig. 5.1. In the case of hydrocarbons employed for the in-liquid plasma, the synthesized nanographene showed the screw-shaped structures as shown in Fig. 5.2. These screwed nanographene had several tens layers of graphene sheets. These large stacks of the graphene sheets in the synthesized crystalline structures are called as nanographite rather than nanographene.

Comparing 1-hexanol with *n*-hexane which has the same number of carbon atoms and the difference point is including hydroxyl group or not, and alcohols worked effectively for the synthesis of highly crystalline nanographene, shown in Table 5.2, owing to the removal of amorphous carbons by hydroxyl group of alcohol.

In the case of benzene, it dramatically increased one order higher rates of the synthesis amount of solid products than the other cases as shown in Fig. 5.1. By occurring dehydration reactions on benzene ring, dangling bonds on the ring-structure easily form highly ordered aromatic ring structure likely graphene sheets. In this case, crystal structures are getting worse than those with the C<sub>2</sub> radical chemistry based on the reaction-pathway occurring in the alcohol cases.

The crystallinity observed by the Raman scattering spectra of nanographene synthesized by the in-liquid plasma employing hydrocarbons did not show the good quality, which had broad FWHM<sub>G</sub> and FWHM<sub>2D</sub> as shown in Table 5.2

Prior to explain our model, optical diagnostic results are discussed. The OES results, shown in Fig. 5.4, hydrocarbons had very weak H $\alpha$  emission intensities. Hydrogen atoms were generated by the dehydration reactions in the in-liquid plasma.

These results indicated that hydrocarbons employed for in-liquid plasma hardly generated H atoms. In the case of alcohol employed for the in-liquid plasma, dehydration reactions were supported by OH radicals originated from hydroxyl group of alcohol molecule. Dehydrated alcohols and alkane have the potential to form C<sub>2</sub> radicals via  $\beta$ -scission. Highly crystalline nanographene formation needs C<sub>2</sub> radical as the carbon source. C<sub>2</sub> is considered as one of key factors of graphene structure formation [6-8].

The tendencies among plasma temperature, C<sub>2</sub> temperature as  $T_v$  and  $T_r$ , and crystallinity of nanographene were similar to the case of changing alcohol types. Highly crystalline nanographenes were synthesized under higher temperatures and lower  $T_r$ ,  $T_v$  of C<sub>2</sub> conditions.

In the case of 1-hexanol employed for in-liquid plasma, molecules with carbon branches were generated and these substances were detected by GC-MS shown in Table 5.5. Branched structures were formed by short-carbon chains originated from fragmentized alcohols. The branches were circularized by bonding of C<sub>2</sub>. O atoms have a potential to form C<sub>2</sub> radicals and support graphene formations. Amorphous carbon effects are removed of O atoms [9,10]. Therefore, O atoms in material molecules play important roles for the crystal formation.

Alcohols are the best materials containing hydroxyl group and synthesizing certain amount of highly crystalline nanographene. Although hydrocarbons can improve the synthesis rate, the crystallinity is greatly reduced due to no oxygen source. Oxygen-related reactions prevent a graphene formation due to its etching effect.

#### 5.4 Conclusion of chapter 5

This chapter described the effects of kinds of carbon precursors such as alcohols,

hydrocarbons, *n*-hexane or benzene employing for the in-liquid plasma on the synthesis of nanographene. A question opens why the alcohol precursor can synthesize high crystalline nanographenes. In contrast, in the case of employing hydrocarbons, synthesis rates were significantly high but worse crystallinities of the synthesized nanographene. In summary, oxygen-containing groups in alcohols play an important role for the improvement of formation with crystal structure owing to removal of amorphous carbons by oxidation reaction with respect to the containing oxygen. Alcohols can synthesize higher crystalline nanographene comparing to hydrocarbons employed for the in-liquid plasma.

In the case of *n*-hexane employed for the in-liquid plasma, the emission intensity for C<sub>2</sub> Swan band emissions was characteristically weak. Because of weak C<sub>2</sub> emission in only *n*-hexane cases, the pathways of  $\beta$ -scission of the alkyl chains were unfavorably. In contrast of alcohol cases, the dehydration from alcohols is considered to be predominantly form OH radicals and O atoms, which etched synthesized carbon materials consequently. Oxygen species have important roles to crystal structures formation.

The nanographene synthesis employing hydrocarbons proceeds furthermore regardless of crystal structures formations. Without oxygen species, this leads the high synthesis rate. The in in-liquid plasma for nanographene synthesis process can be determined by the C atoms-O atoms ratio as an indicator of nanographene crystallinity.

## References

- [1] O. L. Li, H. Hayashi, T. Ishizaki, and N. Saito, "Enhancement of conductivity in nano carbon balls by the addition of carbon tetrachloride via room temperature solution plasma process" *RSC Adv.* **6**, pp.51864-51870 (2016).
- [2] P. Muthakarn, N. Sano, T. Charinpanitkul, W. Tanthapanichakoon, and T. Kanki, "Characteristics of Carbon Nanoparticles Synthesized by a Submerged Arc in Alcohols, Alkanes, and Aromatics" *J. Phys. Chem. B* **110**, pp.18299-18306 (2006).
- [3] O. L. Li, J. Kang, K. Urashima, and N. Saito, "Solution Plasma Synthesis Process of Carbon Nano Particles in Organic Solutions" *Int. J. Plasma Environmental Sci. Technol.* **7**, pp.31-36 (2013).
- [4] J. Kang, O. L. Li, and N. Saito, "Synthesis of structure-controlled carbon nano spheres by solution plasma process" *Carbon* **60**, pp.292-298 (2013).
- [5] M. Matsushima, M. Noda, T. Yoshida, H. Kato, G. Kalita, T. Kizuki, H. Uchida, M. Umeno, and K. Wakita, "Formation of graphene nano-particle by means of pulsed discharge to ethanol" *J. Appl. Phys.* **113**, 114304 (2013).
- [6] F. Müller, H. Sachdev, S. Hüfner, A. J. Pollard, E. W. Perkins, J. C. Russell, P. H. Beton, S. Gsell, M. Fischer, M. Schreck, and B. Stritzker, "How Does Graphene Grow? Easy Access to Well-Ordered Graphene Films" *small* **5**, pp.2291-2296 (2009).
- [7] K. Teii, S. Shimada, M. Nakashima, and A. T. H. Chuang, "Synthesis and electrical characterization of *n*-type carbon nanowalls" *J. Appl. Phys.* **106**, 084303 (2009).
- [8] S. Mori, T. Ueno, and M. Suzuki, "Synthesis of carbon nanowalls by plasma-enhanced chemical vapor deposition in a CO/H<sub>2</sub> microwave discharge system" *Diam. Relat. Mater.* **20**, pp.1129-1132 (2011).
- [9] G. Zhao, D. Shao, C. Chen, and X. Wang, "Synthesis of few-layered graphene by H<sub>2</sub>O<sub>2</sub> plasma etching of graphite" *Appl. Phys. Lett.* **98**, 183114 (2011).
- [10] W. Takeuchi, K. Takeda, M. Hiramatsu, Y. Tokuda, H. Kano, S. Kimura, O. Sakata, H. Tajiri, and M. Hori, "Monolithic self-sustaining nanographene sheet grown using plasma-enhanced chemical vapor deposition" *Phys. Status Solid A*

207, pp.139-143 (2010).

## **Chapter 6. Control of nanographene crystallinity in the in-liquid plasma processes using methanol mixture with the other alcohols**

### 6.1 Backgrounds of this study

Comparing alcohols employed for the in-liquid plasma with hydrocarbons as the feed material, there were differences at the synthesis rate and the crystallinity. Alcohols employed for the in-liquid plasma could synthesize nanographenes with higher crystallinities but synthesis rates were lower compared to those of hydrocarbons. It was considered that the hydroxyl group in the alcohol molecule has a role of crystal formation support. In fact, from results of methanol employed for the in-liquid plasma, any solid products couldn't be synthesized. In addition, the methanol is soluble in many organic solvents and there is a possibility that the amount of hydroxyl group in the liquid can be controlled as additive agent. Methanol mixed alcohol and hydrocarbons were employed to control the crystallinity of synthesized nanographene by in-liquid plasma processes.

### 6.2 Experimental setup

The synthesis equipment was the same as the in-liquid plasma setups as shown in Fig. 4.1. Synthesis conditions are shown in Table 6.1. Mixture liquids were prepared as shown in Tables 6.2 and 6.3. 1-Butanol and *n*-hexane were used as base liquids. Tables show C atoms over O atoms ratios in the liquid. C atoms were counted in the liquid except for originated from methanol and O atoms were main carbon source liquid, 1-butanol or *n*-hexane, plus methanol. Synthesized products were treated by H<sub>2</sub>O<sub>2</sub> water.

Samples were balanced and their crystallographic analyses were carried out

using TEM observation and Raman scattering spectroscopy. For the TEM observation, synthesized samples were dispersed in the ethanol by the ultrasonication. Dispersed samples were dropped on the TEM grids and observed. TEM images were taken at 200 kV acceleration of electrons.

The crystallinity was estimated by Raman scattering spectroscopy. If the crystallinity of synthesized nanographene was improved due to hydroxyl group effects, the full width-half maximum of G-band ( $\text{FWHM}_G$ ) becomes narrow. These results of mixed liquids were compared to the case of employing pure liquids.

Residual liquids after the filtration were analyzed by the GC-MS. Hydroxyl group effects also affected by-products and intermediates. In-liquid plasma emission spectra were observed by the multichannel spectrometer. In the case of 1-butanol, it was considered that emission lines did not change greatly because both methanol and 1-butanol are alcohols, and each emission lines are also common. On the other hand, *n*-hexane had only weak emissions of  $\text{C}_2$ . It is thought that methanol additional effects appear.

Table 6.1. Experimental conditions.

Applying voltage	8 kV
Electrodes	SUS
Gas	Ar, 3 slm
Processing time	10 min
Mixture liquids	1-Butanol + Methanol <i>n</i> -Hexane + Methanol
Filter	1 $\mu\text{m}$ pore
Treatment	$\text{H}_2\text{O}_2$ water (30%), 120 min 120 °C

Table 6.2. Prepared 1-butanol based methanol added liquids.

1-Butanol (ml)	Methanol (ml)	C in 1-butanol/O in entire liquid at 150 ml
150	0	4.00 (Pure 1-butanol)
143	7	3.60
138	12	3.34
123	27	2.67

Table 6.3. Prepared *n*-hexane based methanol added liquids.

<i>n</i> -Hexane (ml)	Methanol (ml)	C in <i>n</i> -hexane/O in entire liquid at 150 ml
150	0	6/0 (Pure <i>n</i> -hexane without O)
93	57	3.01
78	72	2.00
67	83	1.49
59	91	1.20
50	100	0.92
45	105	0.79
32	118	0.50
21	129	0.30

## 6.3 Results and discussion

### 6.3.1 Crystallographic analysis

Figure 6.1 shows synthesis amounts of solid products by in-liquid plasma employing each mixture liquids and ethanol for a reference. Synthesis amounts decreased with increasing methanol added ratio. In the case of 1-butanol based liquid, the decrease rate of synthesis amounts with increasing methanol addition rate was larger comparing with those of *n*-hexane based liquid. At  $C/O = 3.34$ , the synthesis amount was 1.57 mg which was almost the same as that of ethanol. The synthesis amount at  $C/O = 2.67$  was 0.32 mg. In the case of *n*-hexane based liquid employed for the in-liquid plasma, synthesis amounts slightly decreased till  $C/O$  equal to 1. In the condition of  $C/O$  less than 1, synthesis amounts rapidly decreased. At  $C/O = 2.00$ , the synthesis amount was 6.47 mg which was approximately 4 times larger than the ethanol of 1.73 mg. The point of almost the same amount to ethanol was  $C/O = 0.30$  of 1.54 mg. 86% of total liquid volume was methanol at  $C/O = 0.30$ . It is considered that the synthesis amount of nanographene is not determined by the  $C/O$  ratio of material liquid.

Figure 6.2 shows TEM images of synthesized nanographene. It was found that several ten layered structures with sub micrometer grain size were synthesized. Such structures were not observed at the case of single alcohols or hydrocarbons employed for the in-liquid plasma. In the case of *n*-hexane based liquid employed for the in-liquid plasma, several ten nanometer grains and approximately 10 nm many small grains were observed. The configurations were similar in the case of 1-butanol.

Figure 6.3 shows Raman scattering spectra.  $FWHM_G$  of the methanol added liquids were narrowed and 2D-bands became stronger and sharp. Figure 6.4 shows  $FWHM_G$ ,  $FWHM_{2D}$ , and domain size.  $FWHM_G$  linearly decreased with decreasing  $C/O$

ratio. In the case of 1-butanol and methanol mixed liquid at  $C/O = 2.67$ , the  $FWHM_G$  was  $29.7 \text{ cm}^{-1}$ . The nanographene with higher crystallinity comparing to that of ethanol employed could be successfully synthesized. On the other hand, the crystallinities of nanographenes synthesized employing *n*-hexane and methanol mixed liquids were as high as that of 1-butanol.

$FWHM_{2D}$  at small  $C/O$  ratio were narrower than that of ethanol. The 1-Butanol and methanol mixed liquid,  $C/O = 2.67$ , showed  $53.0 \text{ cm}^{-1}$ . Its intensity was 1.06 times larger than G-band intensity. The results were similar to few layer graphene [1,2]. Therefore, highly crystalline nanographene with few layers was included in synthesized products. In the case of *n*-hexane and methanol mixed liquids,  $FWHM_{2D}$  at under  $C/O = 1.00$  rapidly narrowed. The tendency of  $FWHM_{2D}$  was similar to synthesis amounts. It was thought that  $C/O$  ratio less than 1.00 conditions worked effectively on the crystallization but this phenomenon was trade-off relationship with the synthesis rate.

The domain size calculated from D- and G-band peak area intensities were shown in Fig. 6.4(c) In the case of 1-butanol and methanol mixed liquids, domain size increased with decreasing  $C/O$  ratio. On the other hand, in the case of *n*-hexane based liquid, the range of increase and decrease was large and there was independent of  $C/O$  ratio.

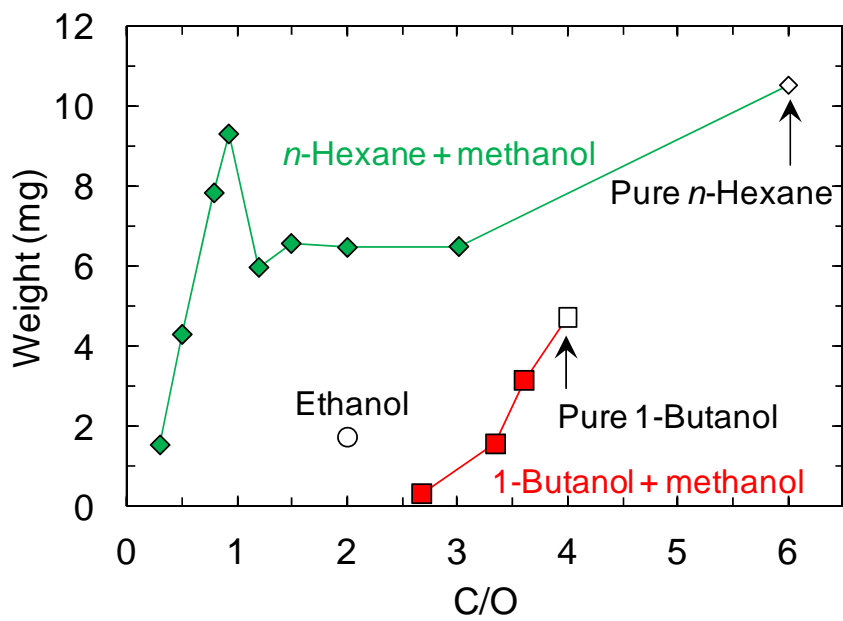
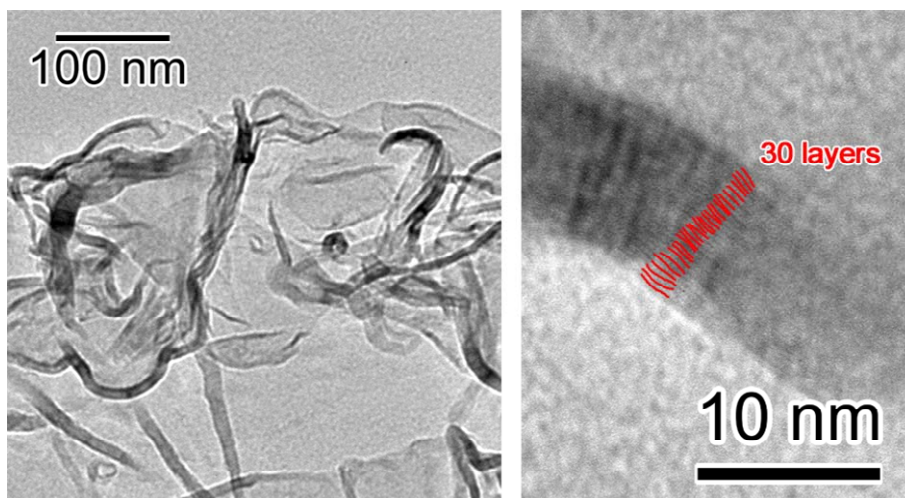
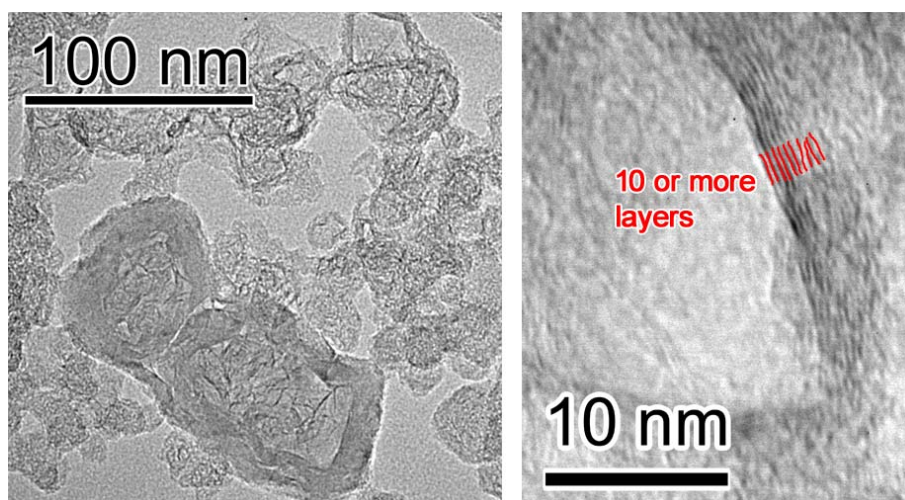


Figure 6.1. Synthesis amounts of nanographene by mixture liquids employed in-liquid plasma.



(a)



(b)

Figure 6.2. TEM images of synthesized nanographene. (a) 1-Butanol + Methanol (C/O = 2.67). (b) n-Hexane + Methanol (C/O = 2.00).

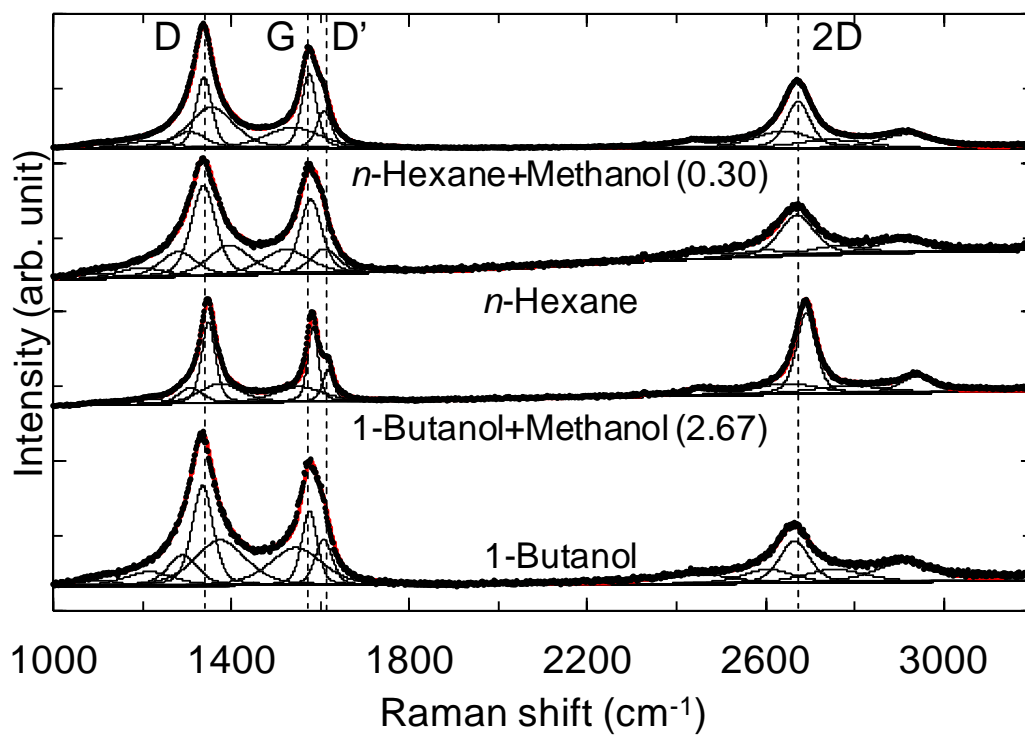
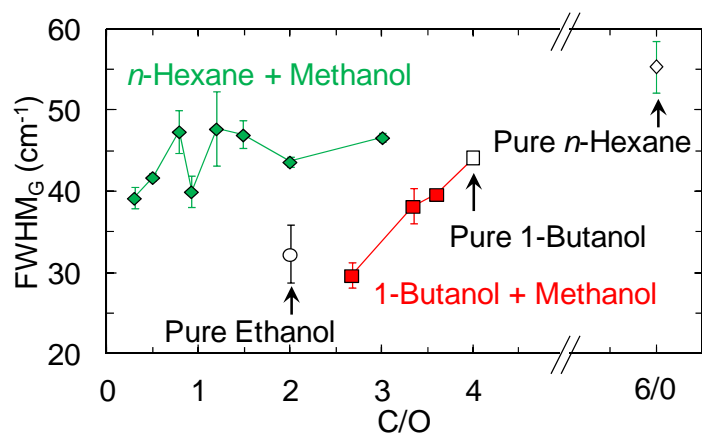
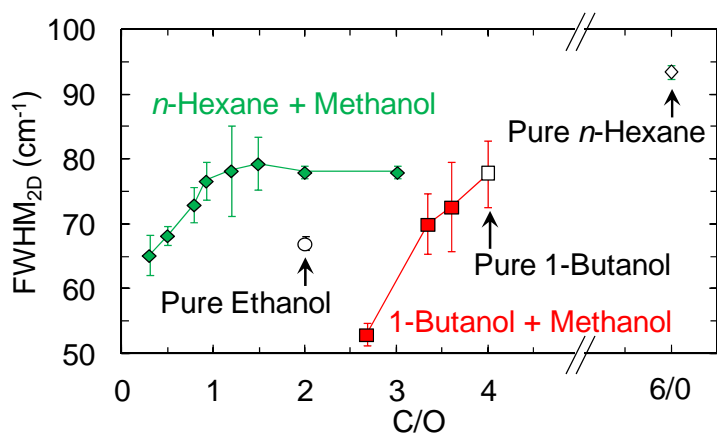


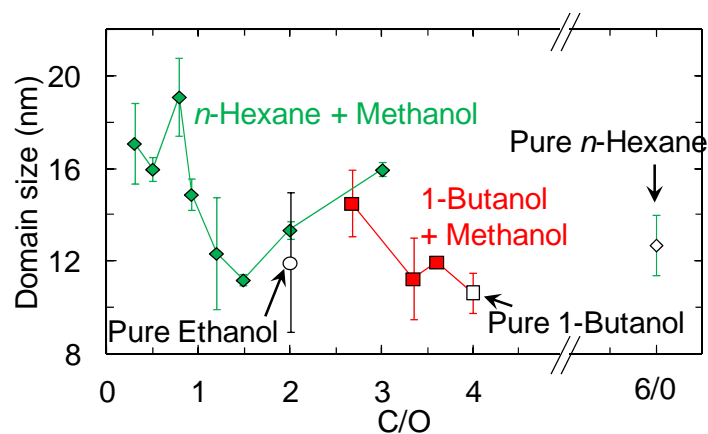
Figure 6.3. Raman scattering spectra.



(a)



(b)



(c)

Figure 6.4. Results of crystallographic analysis by Raman scattering spectroscopy. (a)

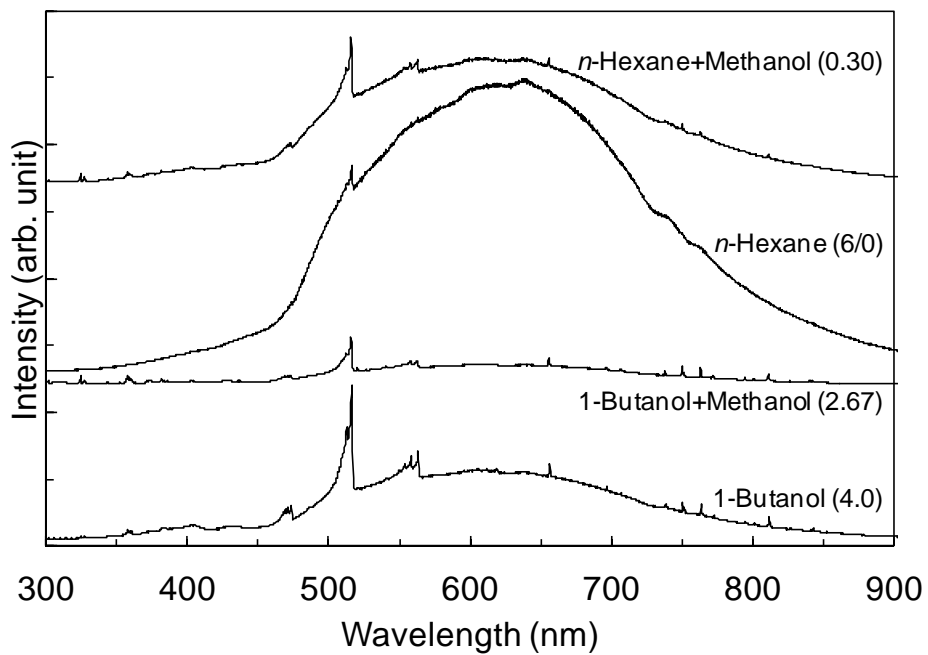
FWHM<sub>G</sub>. (b) FWHM<sub>2D</sub>. (c) Domain size.

### 6.3.2 Measurement of the in-liquid plasma employing mixture liquid

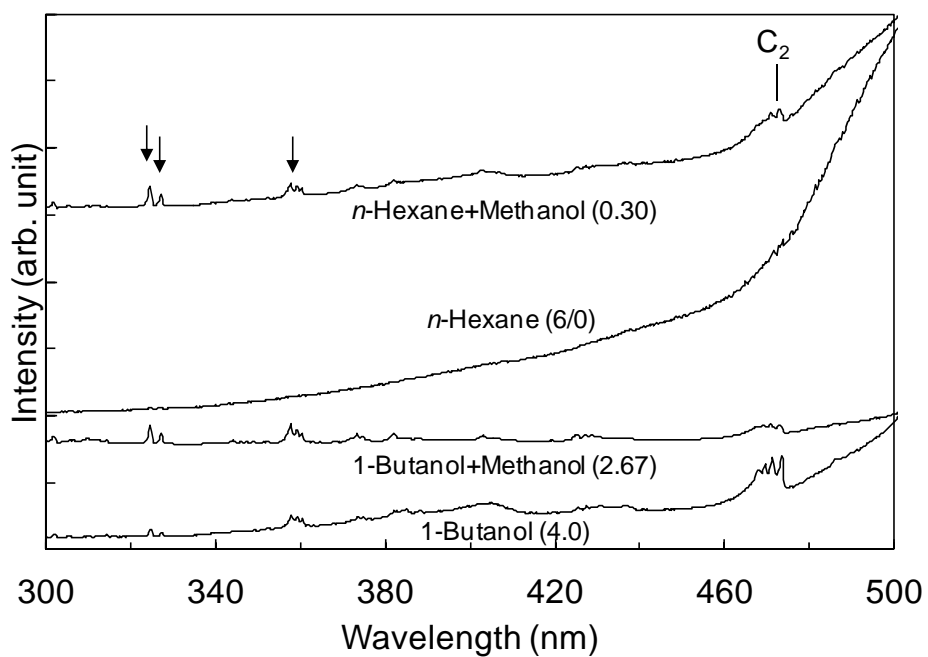
Figure 6.5(a) shows optical emission spectra of in-liquid plasma. In the case of employing 1-butanol and methanol mixed liquid, C<sub>2</sub> Swan band emission intensities became lower comparing to pure 1-butanol. In addition, blackbody radiation intensity decreased. This was caused by decrease of synthesis rate. Decreasing density of synthesized nanomaterials in the in-liquid plasma induced the decrease of radiance. In the case of *n*-hexane and methanol mixed liquid, C<sub>2</sub> Swan band, H $\alpha$ , and Ar emissions were clearly seen comparing to those of pure *n*-hexane. Figure 6.5(b) shows enlarged spectra in 300-500 nm region of Fig 6.5(a). In the case of 1-butanol and methanol mixed liquid, the intensity of C<sub>2</sub> at 474.8 nm became weaker than that of pure 1-butanol. As the proportion of the 1-butanol decreased, the density of C<sub>2</sub> decreased and the emission intensity declined. On the other hand, the peaks at 324.8, 327.5, and 358.0 nm became stronger. These changes were considered to be indications of the effect by adding methanol. In the case of *n*-hexane and methanol mixed liquid, the intensity of C<sub>2</sub> at 474.8 nm became stronger than that of pure *n*-hexane. It was considered that generation of the C<sub>2</sub> was promoted by the mixing methanol. The peaks at 324.8, 327.5, and 358.0 nm were not seen with pure *n*-hexane, but they appeared in the *n*-hexane and methanol mixed liquid.

Blackbody radiation intensity decreased.  $T$  calculated from blackbody radiation using Wien's displacement law,  $T_v$  and  $T_r$  of C<sub>2</sub> calculated from C<sub>2</sub>  $\Delta\nu = 0$  emissions using spectra fitting were shown in Fig. 6.6. In the case of 1-butanol and methanol mixed liquid,  $T$  was decreased with decreasing C/O ratio. In the pure liquid case, nanographenes synthesized under higher temperature conditions had the higher crystallinity. The synthesis reaction of nanographene on mixed liquid employed for the in-liquid plasma is

different from that of pure liquid.  $T_v$  and  $T_r$  decreased with decreasing C/O ratio and values were approached to ethanol. In the case of *n*-hexane and methanol mixed liquid,  $T$  slightly increased with decreasing C/O ratio. This tendency was different from 1-butanol and methanol mixed liquid.  $T_v$  and  $T_r$  decreased with decreasing C/O ratio but values were relatively high.

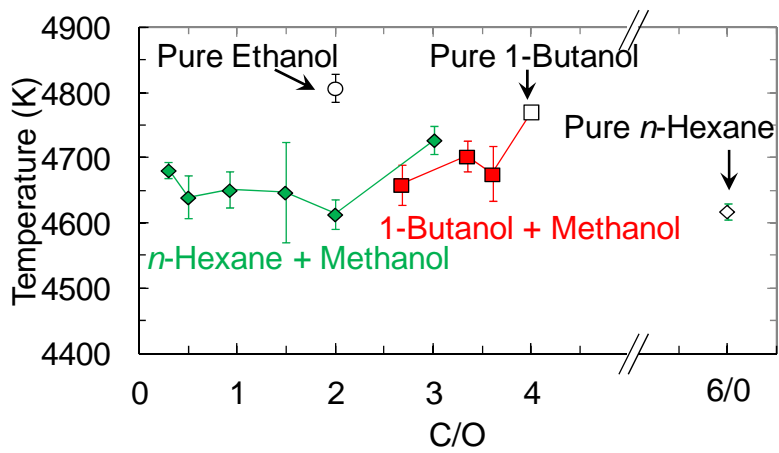


(a)

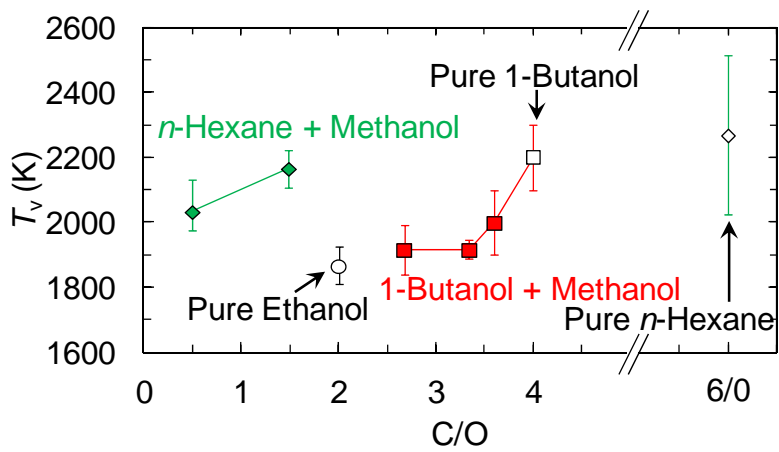


(b)

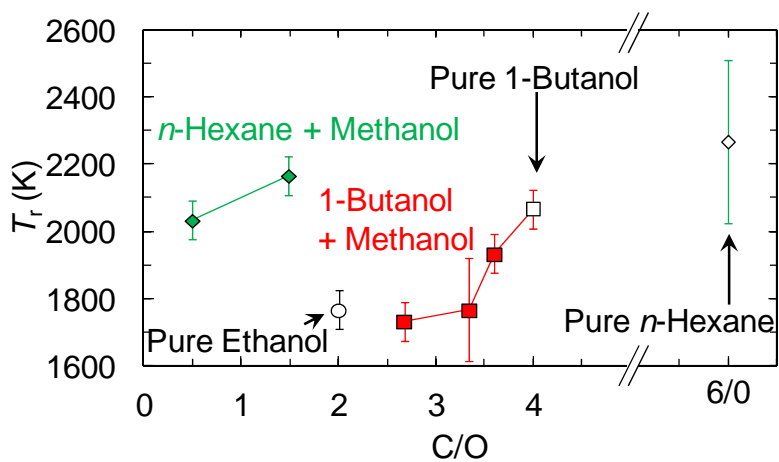
Figure 6.5. Optical emission spectra of the in-liquid plasma. Numbers in brackets are C/O ratio. (a) Wide range spectra. (b) Enlarged spectra in 300-500 nm region of (a).



(a)



(b)



(c)

Figure 6.6. Temperatures. (a) Blackbody temperature. (b)  $T_v$  of  $C_2$ . (c)  $T_r$  of  $C_2$ .

### 6.3.3 By-products and intermediates analysis in the filtered liquids

After in-liquid plasma treatment liquids color were changed into yellowish but their depths were dilute comparing to the pure liquid case. These differences indicated that reactions were inhibited by methanol. Table 6.4 shows detected substances from 1-butanol and methanol mixed liquids. Methanol added 1-butanol generated carbon chain and branch structures but the number of types was low comparing to pure 1-butanol. Oxygen species affects the formation of substances. Benzene ring structures contained substances were hardly generated. In the case of *n*-hexane and methanol mixed liquids, benzene rings contained substances were generated on a preferential basis. The added methanol supported to generate benzene rings due to oxygen species supply in the C-poor conditions (C/O ratio < 1), e.g., *n*-hexane.

Table 6.4. Detected substances from filtered 1-butanol and methanol mixed liquids.

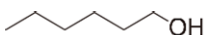
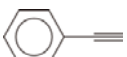
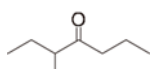
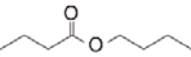
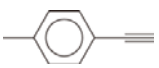
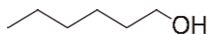
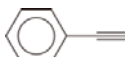
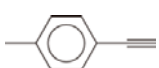
Retention time (min)	m/z	1-butanol + Methanol C/O (Matching quality)			Formula	Structure
		4.00	3.34	2.67		
3.92	102	✓ (86)			C <sub>6</sub> H <sub>13</sub> OH	
4.02	102	✓ (60)			C <sub>8</sub> H <sub>16</sub>	
4.10	130	✓ (86)	✓ (59)	✓ (38)	C <sub>8</sub> H <sub>18</sub> O	
4.76	128	✓ (91)			C <sub>8</sub> H <sub>16</sub> O	
5.72	144	✓ (90)	✓ (59)	✓ (64)	C <sub>8</sub> H <sub>16</sub> O <sub>2</sub>	
6.50	116	✓ (90)			C <sub>9</sub> H <sub>8</sub>	
8.58	128	✓ (91)			C <sub>10</sub> H <sub>8</sub>	

Table 6.5. Detected substances from filtered *n*-hexane and methanol mixed liquids.

Retention time (min)	m/z	<i>n</i> -Hexane + Methanol C/O (Matching quality)			Formula	Structure
		6/0	1.49	0.92		
3.92	102	✓ (83)		✓ (78)	C <sub>6</sub> H <sub>13</sub> OH	
4.02	102	✓ (91)	✓ (91)	✓ (91)	C <sub>8</sub> H <sub>16</sub>	
6.50	116	✓ (90)	✓ (90)	✓ (90)	C <sub>9</sub> H <sub>8</sub>	
7.26	156	✓ (95)			C <sub>11</sub> H <sub>24</sub>	
8.58	128	✓ (94)	✓ (91)	✓ (91)	C <sub>10</sub> H <sub>8</sub>	

### 6.3.4 Discussion: Oxygen species effects

The methanol addition to liquids improved to the crystallinity of synthesized nanographene shown in Fig 6.4(a) but the synthesis rate shown in Fig. 6.1 decreased with decreasing C/O ratio. Effects of oxygen species on the synthesizing nanographenes were different between alcohols and hydrocarbons. In the case of 1-butanol, the 1-butanol inherently has a hydroxyl group in the molecule. This hydroxyl group is fragmented and then enhances the reactions of nanographene formation. Addition of methanol, which has a hydroxyl group and a carbon atom in the molecule, does not contribute to formation of nanographene. Oxygen species generated from the methanol affected the potentiating dehydration, and the etching of amorphous carbon removal. Higher abundance of oxygen species promoted fragmentations of 1-butanol and suppressed nanographene growth; however, the nanographene synthesized in these conditions had the high crystallinity due to the removal of amorphous carbon by oxygen species.

The large film-like graphene shown in Fig. 6.2(a) which had sub-micrometer order grain size could be synthesized at  $C/O = 2.67$ . Such graphene with large grain was not synthesized under other conditions. It was considered that the effect of oxygen species induced growth of graphene with sub-micrometer grain. On the other hand, from the GC-MS result shown in Table 6.4, the by-products or intermediates with benzene rings were hardly synthesized. This result indicated that oxygen species have played to inhibit nucleation of nanographene, but they had the function of further growing formed nanographene. These reactions were considered to accelerate the decompositions of the 1-butanol as a raw material of nanographene by oxygen species from the methanol. It was thought that oxygen species made it easy to supply  $C_2$  by breaking lattice defects and edges in the nanographene to form dangling bonds.  $C_2$  contributed to the growth of

nanographene nuclei probably by incorporating into dangling bonds generated in the six-membered ring structures.

In the case of *n*-hexane and methanol mixed liquids, the effects of methanol addition appeared as decrease of the synthesis rate shown in Fig. 6.1 and improvement of the crystallinity shown in Fig. 6.4(a) but changes were gradual comparing with those of 1-butanol. *n*-Hexane has the longer-carbon chain comparing to 1-butanol. *n*-Hexane needs a large amount of methanol for the obtaining high performances of the nanographene. The synthesis rate rapidly decreased less than  $C/O = 1.00$ .

From the results of Raman scattering spectroscopy shown in Fig 6.4, 1-butanol and methanol mixed liquid, of which  $C/O = 2.67$ , the  $FWHM_G$  was smaller than ethanol which was the smallest  $FWHM_G$  in the pure liquid employed for the in-liquid plasma. In addition,  $FWHM_{2D}$  and intensity of 2D-band were narrow and strong. These two values indicated that synthesized nanographenes had few layers [1,2].

The plasma temperature estimated from the blackbody radiation at 1-butanol and methanol mixed liquid employed for the in-liquid plasma decreased with decreasing  $C/O$  ratio as shown in Fig. 6.6(a). In the case of pure alcohol, the highly crystalline nanographene was synthesized at higher temperatures. The mixed liquid of 1-Butanol and methanol employed generated many oxygen species. Oxygen species were originated from 1-butanol and methanol. Therefore, a large amount of oxygen species were generated in the mixed liquid and showed large effects. In the case of a mixed liquid of *n*-hexane and methanol, temperature slightly increased with decreasing  $C/O$  ratio. The range of change was small; therefore, effects of oxygen species were larger.

$T_v$  and  $T_r$  of  $C_2$  decreased with decreasing  $C/O$  ratio as shown in Fig. 6.6(b) and (c). Oxygen species supported  $C_2$  generations via dehydrations. Therefore, it was able to

generate  $C_2$  with smaller  $T_v$  and  $T_r$ . Comparing  $T_v$  and  $T_r$  with the crystallinity,  $T_v$  and  $T_r$  showed lower values when nanographene with high crystallinity was synthesized. These were the same trend as the results shown in Chapter 4 and 5. It was considered that  $T_v$  and  $T_r$  of  $C_2$  were key plasma parameters which determine the crystallinity of nanographene. The difference between nanographene synthesis by in-liquid plasma and SWNTs synthesis by arc plasma is whether raw materials are decomposed to form nanographene or SWNTs are formed via catalysts. In the in-liquid plasma process, lower energy  $C_2$  behaves favorably for the synthesis of nanographene with high crystallinity.

From the results of GC-MS analysis shown in Table 6.4 and 6.5, the substances containing benzene rings in 1-butanol and methanol mixed liquids decreased comparing with those of pure 1-butanol. It was thought that formations of benzene rings were difficult due to the effects of large amount of oxygen species. In this condition, it was hard to form small structures like nanographene. But if large-weight molecule is used, amorphous carbons were effectively removed by oxygen species during the growth to a large size of sheets. In the case of *n*-hexane and methanol mixed liquids, generations of substances without benzene rings were suppressed. Figure 6.7 shows an example of possible pathway of nanographene formation from *n*-hexane and methanol mixed liquid. The oxygen species which was generated from methanol supported the reactions such as dehydration and etching amorphous carbons. When  $C_2$  and benzene rings structures were formed, by-products with carbon chain and branch groups more were yielded.

The methanol has a potential as an additional agent to improve the crystallinity. Oxygen species have key roles for the formation of crystal structure of carbon. The problem is the synthesis rate. In this study, the in-liquid was generated by a pair of small electrodes. Therefore, the synthesis rates of this study were smaller than previous study

[3]. Previous study had used electrodes with vertical at gas phase and horizontal at liquid phase. This configuration can generate larger volume plasma compared with this study. One of the solutions of synthesis rate problem is change of electrodes configuration. Another solution is equipment of multiple electrodes. A pair of electrodes can treat narrow region. By arranging multiple electrodes, a large amount of liquid can be treated.

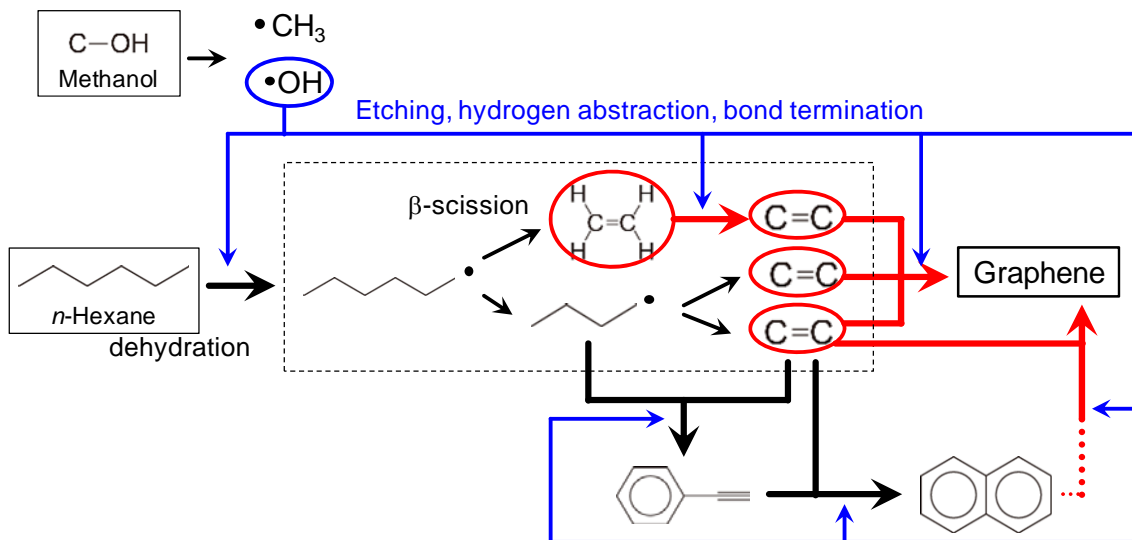


Figure 6.7. Schematic diagram of possible pathway of nanographene formation from methanol and *n*-hexane mixed liquid.

## 6.4 Conclusion of chapter 6

The methanol added 1-butanol or *n*-hexane were employed to obtain the highly crystalline nanographene. Synthesis rates decreased with decreasing C/O ratio. When the C/O ratio decreased, the synthesis rate tended to be similar as pure alcohols, but in the case of 1-butanol and methanol mixed liquid, the C/O ratio was 3.34 which was comparable to that of ethanol (C/O = 2.00), and in the case of *n*-hexane and methanol mixed liquids, C/O = 0.30. On the other hand, 1-Butanol has hydroxyl group itself, and *n*-hexane is not. This difference will cause these results. 1-butanol and methanol at C/O = 2.67 employed for the in-liquid plasma synthesized sheets with sub micrometer size and several ten layers. Large amounts of oxygen species enable us to synthesize small crystals and enhance the growth of large crystals. In addition, from Raman scattering spectroscopy, C/O = 2.67 of 1-butanol and methanol had the sharp 2D-band. The products included few layer nanographene. Large sheets formations were analyzed by GC-MS results. Benzene rings contained substances were hardly formed. Small crystals were fragmentized by many oxygen species.

In the case of *n*-hexane and methanol mixed liquids, improvement of crystallinity also appeared but the effects were small compared to the case of 1-butanol and methanol mixed liquids. On the other hand, in the case of liquid with less than 1.00 of C/O ratio, the synthesis rate rapidly decreased. Since there were more oxygens than carbons, it could be sufficiently reduced rapidly. By-products and intermediates had substances containing benzene rings. Carbon chain and branch structures were not detected much. Oxygen species worked at the forming of crystal structures and decomposing the by-products.

The oxygen species in the in-liquid plasma may act dehydration and removal of

amorphous carbons. The concentration of oxygen species increases with increasing adding methanol. When the dehydration reaction is promoted by the increase of oxygen species, the  $\beta$ -scission of the carbon chain increases is induced. Alcohols and hydrocarbons are fragmentized and  $C_2$  is more likely to form.  $C_2$  binds to each other and combines with the branch to cyclize to form six membered ring structures. In addition, oxygen species may act on by-products and may promote the generation of  $C_2$ . However, significant increase in oxygen species in the in-liquid plasma is thought to work for decomposition of nanographene.

It could be regarded as appearing at the  $T_v$  and  $T_r$  of  $C_2$  as to the point that  $C_2$  was more likely to be formed. The  $T_v$  and  $T_r$  of  $C_2$  were lower when nanographene with high crystallinity was synthesized. The  $T_v$  and  $T_r$  of  $C_2$  in the in-liquid plasma are important factors determining the crystallinity of synthesized nanographene.

In in-liquid plasma for nanographene synthesis process, the methanol can be used for controlling the crystallinity. However, the crystallinity has a trade-off relationship with the synthesis rate. It is necessary to improve processing efficiency in order to realize a high synthesis rate. For example, it is considered effective to increase the number of electrodes to be place.

## References

- [1] A. C. Ferrari, “Raman spectroscopy of graphene and graphite: Disorder, electron-phonon coupling, doping and nonadiabatic effects” *Solid State Commun.* **143**, pp.47-57 (2007).
- [2] L. M. Malard, M. H. D. Guimarães, D. L. Mafra, M. S. C. Mazzoni, and A. Jorio, “Group-theory analysis of electrons and phonons in  $N$ -layer graphene systems” *Phys. Rev. B* **79**, 125426 (2009).
- [3] T. Hagino, H. Kondo, K. Ishikawa, H. Kano, M. Sekine, and M. Hori, “Ultrahigh-Speed Synthesis of Nanographene Using Alcohol In-Liquid Plasma” *Appl. Phys. Express* **5**, pp.035101(3) (2012).

## **Chapter 7. Conclusions and future works**

### **7.1 Summary of this thesis**

In this thesis, the arc plasma for SWNTs synthesis and the in-liquid plasma employing alcohols or hydrocarbons for nanographene synthesis were measured by OES and synthesized SWNTs and nanographene were analyzed to investigate growth mechanisms. The relationships between  $C_2$  and catalytic metals atoms in arc plasma were clarified for the first time. Alcohols dissociations and nanographene or by-products formation pathways were suggested and the crystallinity control technique was successfully developed. Each chapter is briefly summarized in this chapter.

In Chapter 1, basic physics of SWNTs and graphene were described. In addition, their typical synthesis methods and used in this study synthesis methods were explained. Previous works which focused relationships between ambient gas and chemical species in arc plasma for SWNTs synthesis or in-liquid plasma synthesized nanographene with different crystallinity employing various types of alcohols were described. Then purpose and outline of this thesis were described.

In Chapter 2, carbon nanomaterials synthesis systems were described. For SWNTs synthesis, arc plasma apparatus, measurement setup, and experimental procedure were briefly described. In addition, physics of arc plasma for SWNTs synthesis was briefly explained. In-liquid plasma were also described. The principle of OES and evaluation techniques, Raman scattering spectroscopy and GC-MS, were explained.

In Chapter 3, the effects of active species in arc plasma on the crystallinity of SWNTs and factors of crystallinity were investigated using OES of arc plasma and Raman scattering spectroscopy of SWNTs. The OES was especially focused behaviors of

carbon species and used mixture catalytic metals, i.e., Ni and Y. The crystallinity decreased with increasing arc current or He pressure. Emission intensity ratios of Ni/C<sub>2</sub> and Y/C<sub>2</sub> decreased with increasing arc current or He pressure. These relationships had similar tendencies. High Ni/C<sub>2</sub> or Y/C<sub>2</sub> ratio indicated relatively high density condition of atomized and excited catalytic metals. Active atoms reacted with other catalytic metals and carbon species to form growth base of SWNTs. Decreasing intensity ratios were controlled by increasing evaporation rate of electrode due to increasing arc current or He pressure. Higher particles density plasma easily induced collisions of chemical species. At that time, too many carbon species covered catalytic metals and became catalytic poison. Covering carbons were amorphous carbons. Therefore, increasing content rate of amorphous carbons induced as decreasing crystallinity. Highly crystalline SWNTs synthesis needs the balance of appropriate amount of evaporation and excited atomic catalytic metals.

In Chapter 4, in-liquid plasma employing various types of alcohols, methanol, ethanol, 1-butanol, or 1-hexanol was measured by OES, synthesized nanographene was analyzed using Raman scattering spectroscopy, and residual liquids were analyzed using GC-MS. Methanol employed for the in-liquid plasma couldn't synthesize any solid products. 1-butanol and 1-hexanol synthesized the larger amount of nanographene compared with that of ethanol but the difference between 1-butanol and 1-hexanol was small. Crystallinity of synthesized nanographene became low with increasing carbon atoms number in unit molecule. OES result showed C<sub>2</sub> and H $\alpha$  emissions as the alcohol origin. Residual liquids included various types of substances except for the methanol. Ethanol plasma generated substances containing benzene rings. 1-butanol and 1-hexanol generated carbon chain and branch structures in addition to benzene rings. From these

results, the C<sub>2</sub> formation by the plasma was the first step of nanographene formation. In the case of ethanol, C<sub>2</sub> was easily formed due to ethanol molecular structure. In the case of 1-butanol, two C<sub>2</sub> can be generated via single β-scission. High synthesis rate on 1-butanol may be originated from this feature. This chapter suggested the nanographene synthesis pathway and singularity of methanol.

In Chapter 5, *n*-hexane and benzene were employed as materials for nanographene synthesis by the in-liquid plasma. The *n*-hexane has the similar molecular structure to the 1-hexanol. The difference point is with or without a hydroxyl group. Basic structure of nanographene consists of the benzene ring. Therefore, benzenes were expected to increase the synthesis rate. As the result, these materials could dramatically increase the synthesis rate. However, crystallinities significantly became low. From GC-MS analysis, larger numbers of types of branched molecules were detected at the 1-hexanol compared with *n*-hexane. It was considered that oxygen species enhanced formation of short-carbon chain due to the dehydration. Dehydrated molecules induced β-scission. Oxygen species have a potential to make crystal structures.

In Chapter 6, 1-butanol and *n*-hexane with addition of methanol were employed to control of crystallinity of nanographenes. From the result of Chapter 5, oxygen species have played important roles to form crystal structures. In addition, from results of chapter 4, methanol had potential to increase hydroxyl group in liquids. Addition of methanol improved the crystallinity with a trade-off relationship to the synthesis rate. In the case of 1-butanol based liquids, the synthesis rate was decreased but synthesized nanographene crystallinity was drastically improved. On the other hand, the changes in *n*-hexane based liquids were moderate compared to 1-butanol. The difference was dependent on the liquid molecule. The 1-butanol has hydroxyl group; therefore, it was considered that

1-butanol based liquids suddenly increased effects of oxygen species. These results suggested that methanol can be used to control the nanographene crystallinity. It was noteworthy that the graphene with sub-micrometer grain size was synthesized in the methanol and 1-butanol mixed liquid employed in-liquid plasma. Although it was the trade-off relationship with the synthesis rate, synthesizing several hundred nanometers grain size of graphene was succeeded which was difficult with the conventional in-liquid plasma. The added methanol, i.e., the oxygen species played very important roles in graphene growth by in-liquid plasma.

In this thesis, a part of synthesis mechanisms of carbon nanomaterials were clarified for the first time by measuring different types of high-density media plasmas using OES and analyzing synthesized carbon nanomaterials. This study revealed the reactions of the chemical species in the high-density media plasma and opened up a way to improve and control the synthesis processes.

## 7.2 Scopes for future works

Plasmas for synthesizing carbon nanomaterials were measured and carbon nanomaterials were synthesized and analyzed to clarify their synthesis mechanisms. It was found that  $C_2$  radical was the important precursor to synthesize carbon nanomaterials. In the case of the arc plasma for SWNTs synthesis,  $C_2$ , Ni, and Y abundances are important for the synthesizing highly crystalline SWNTs synthesis. In this study, relative densities of the chemical species were measured but absolute densities have not been measured. In plasma processes, chemical species in plasmas have played important roles and their densities determine the most important properties of plasma. In addition, measurements of electron densities also provide important information about plasma

properties. In order to elucidate the synthesis mechanism of SWNTs completely, it is necessary to develop a system that can observe the synthesis reactions in real-time. If visualization by electron microscope is possible, it is easy to observe the growth of SWNTs. However, arc plasma for SWNTs synthesis is harsh environment for electron microscopes and contact type probes. Therefore, for observation, it is desirable to apply observation method without contact that does not affect the arc plasma. These measurements enable us to clarify behaviors of chemical species and electrons, and their interaction. These knowledge will lead to the elucidation of SWNTs synthesis mechanism and development of quality control of SWNTs is realized.

In in-liquid plasma for nanographene synthesis, measurements of chemical species are also necessary to clarify the synthesis mechanism. Results of methanol added liquids employed for the in-liquid plasma suggested the possibility of achieving the growth control of nanographenes using oxygen species. Therefore, the measurement of species, especially C<sub>2</sub> and oxygen species are considered to be important. As clarified by this study, liquids containing carbon may potentially be sources of nanographene. In addition, considering the fact that the graphene with sub-nanometer grain size was synthesized by the in-liquid plasma employing methanol and 1-butanol mixed liquid, it can be expected to be applied to various material synthesis. For example, it is possible to simplify a complicated process by dispersing substances to be supported on nanographene in a liquid. It is considered that synthesis other than carbon nanomaterials is also possible.

The in-liquid plasma has great potential to be applied to the wide area. Besides material synthesis, we can expect unprecedented plasma applications such as the liquid treatment, the liquid treatment of substances, the mixed plasma reactions of liquid and

gas, and so on. Furthermore, the characterization of in-liquid plasma is necessary to establish a science and technologies in the in-liquid plasma processes.

## **Acknowledgements**

The present study was performed in Professor Hori, Professor Sekine, and Professor Ishikawa Laboratory Department of Electrical Engineering and Computer Science, Nagoya University, and Professor Ito and associate Professor Ohta Laboratory Department of Electrical and Electronic Engineering, Meijo University. Author would like to appreciate his research advisor, Professor Masaru Hori, Institutes of Innovation for Future Society, Nagoya University, for his guidance, advices, and encouragements through the course of this research. The author also would like to appreciate his advisor, Professor Masafumi Ito, Department of Electric and Electronic Engineering, Meijo University, for his guidance, advices, and encouragements through the course of this research. The author also would like to appreciate his vice-advisors, Professor Makoto Sekine, Plasma Nanotechnology Research Center, Nagoya University, Professor Kenji Ishikawa, Plasma Nanotechnology Research Center, Nagoya University, associate Professor Hiroki Kondo, Department of Electrical Engineering and Computer Science, Nagoya University, associate Professor Takayuki Ohta, Department of Electrical and Electronic Engineering, Meijo University, and associate Professor Keigo Takeda, Department of Electrical and Electronic Engineering, Meijo University, associate Professor Takayoshi Tsutsumi, Department of Electrical Engineering and Computer Science, Nagoya University, associate Professor Hiroshi Hashizume, Institutes of Innovation for Future Society, Nagoya University, and Dr. Hiromasa Tanaka, Institutes of Innovation for Future Society, Nagoya University, for lots of valuable comments. The author also would like to thanks his vice-advises, Professor Hirotaka Toyoda, Department of Electrical Engineering and Computer Science, Nagoya University, Professor Nobuyuki Ikarashi, Department of Electrical Engineering and Computer Science, Nagoya University, and Professor Minoru Sasaki, Department of Advanced Science and Technology, Toyota Technological Institute, for their guidance and valuable suggestions in preparing this thesis.

At the same time, the author would like to thank Professor Hirotaka Toyoda, Department of Electrical Engineering and Computer Science, Nagoya University, for his hearty management in International Training Program.

The author is enormous grateful to Professor Mineo Hiramatsu, Department of Electrical and Electronic Engineering, Meijo University, Professor Yoshinori Ando, Department of Material Science and Engineering, Meijo University, for their valuable comments and suggestions. The author would like to acknowledge Dr. Fengdong Jia, Dr. Hiroyuki Kano at NU Eco Engineering Co.,Ltd, Dr. Koji Yamakawa at Katagiri Engineering Co.,Ltd, Dr. Sakae Inoue at Material Science and Engineering, Meijo University, and Dr. Tomoko Suzuki at Material Science and Engineering, Meijo University, for their helpful advices and discussions.

The author appreciates Prof. Francesco Fracassi, Prof. Pietro Favia, Dr. Maria Grazia, and all other members in Laboratory, Università di Bari “Aldo Moro”, Italy, for giving me the opportunity to study in the group.

The author also thanks sincerely Mr. Naoki Aoyama, Mr. Kenta Niwa, and Mr. Kazuaki Kojima who aided his experimental works carried out in this study and also expressed their valuable suggestions and discussions. The author also thanks Dr. Yudai Miyawaki, Dr. Hironao Shimoeda, Dr. Toshiya Suzuki, Dr. Hyung Jun Cho, Dr. Lu Yi, Dr. Yusuke Kondo, Dr. Lingyun Jia, Dr. Zecheng Liu, Dr. Naoyuki Kurake, Mr. Yan Zhang, Mr. Youhei Takahashi, Mr. Kuangda Sun, Mr. Jiadong Cao, Mr. Haoran Wang, Mr. Takashi Kako, Mr. Joug Yun Park, Mr. Timothy Ryan Brubaker, Mr. Keita Miwa, Mr. Masayuki Nakamura, Mr. Da Xu, Ms. Sijie Liang, Mr. Shun Imai, Mr. Hirotsugu Sugiura, Mr. Masakazu Tomatsu, Mr. Yusuke Fukunaga, Mr. Borude Ranjit Rohidas, Mr. Takumi Kumakura, Mr. Kazuki Iwamoto, Mr. Chih Tung Liu, Mr. Yu Chun Lin, Mr. Shinnoske Takai, Mr. Takuya Tonami, Mr. Kenichi Naito, Mr. Ryo Furuta, Mr. Naoki Yoshitake, Mr. Shunichi Sato, Mr. Suiki Tanaka, Mr. Atsuki Asano, Mr. Masato Imamura, Mr. Yukihiro Kurokawa, Ms. Mika Takahashi, Mr. Tshinari Ueyama, Mr. Daiki Kanno, Mr. Ren Kuramashi, Mr. Tomonori Itikawa, Ms. Kaede Katsuno, Mr. Naoki Takeda, Mr. Yugo Hosoi, Mr. Kaito Murakami, Mr. Sotaro Yamaoka, Mr. Xitong Xie, Ms. Yan Hao, Mr. Kazuya Nakane, Mr. Ryo Hamaji, Mr. Takumi Kato, Mr. Shogo Maeda, Mr. Takahiro Ohmichi, Mr. Yasuyuki Ohashi, Mr. Masaki Hasegawa, Mr. Susumu Nagano, Mr. Hidenori Kishimoto, Mr. Hideyuki Hori, Mr. Ryuhei Kokuoh, Mr. Tetsuya Yamada, Mr. Daisuke Ito, Mr. Kosaku Kuno, Mr. Kazuki Fujita, Kosuke Fukushima, Mr. Hiroto Kato, Mr. Takuya Towatari, Mr. Shinji Mitsuguchi, Mr. Michiya Nagashima, and all other

students who have studied in Professor Hori, Professor Sekine, and Professor Ishikawa Laboratory and Professor Ito and associate Professor Ohta Laboratory for giving the big pleasure in life and creating a most enjoyable work atmosphere.

The author appreciates Ms. Yoko Kuwahara, Ms Kanae Teshigawara, Ms. Asako Nishiyama, Ms. Kazuyo Hirota, Ms. Taeko Terasawa, Ms. Aya Honda for lots of encouragements and helpful advices in day-to-day life.

*Atsushi Ando*

December 2017

## List of papers related to this thesis

### 1. Original Papers

Title	Journal	Authors	Related Chapter
1. Characteristics of optical emissions of arc plasma processing for high-rate synthesis of highly crystalline single-walled carbon nanotubes	Japanese Journal of Applied Physics <b>56</b> , 035101 (2017).	A. Ando, K. Takeda, T. Ohta, M. Ito, M. Hiramatsu, K. Ishikawa, H. Kondo, M. Sekine, T. Suzuki, S. Inoue, Y. Ando, and M. Hori	Chapter 3
2. Nanographene synthesis employing in-liquid plasmas with alcohols or hydrocarbons	Japanese Journal of Applied Physics <b>57</b> , 026201 (2018).	A. Ando, K. Ishikawa, H. Kondo, T. Tsutsumi, K. Takeda, T. Ohta, M. Ito, M. Hiramatsu, M. Sekine, and M. Hori	Chapter 5
3. Impact of helium pressures in arc plasma synthesis on crystallinity of single-walled carbon nanotubes (SWNTs)	Japanese Journal of Applied Physics (Submitted)	A. Ando, K. Takeda, T. Ohta, M. Ito, M. Hiramatsu, K. Ishikawa, H. Kondo, M. Sekine, T. Suzuki, S. Inoue, Y. Ando, and M. Hori	Chapter 3

## 2. International Conferences

Title	Conference	Authors
1. Optical emission spectroscopy of arc plasma for synthesizing carbon nanotubes	4th International Symposium on Advanced Plasma Science and its Applications for Nitrides and Nanomaterials, P3104C, Kasugai, Japan, Mar. 4-8, 2012	A. Ando, T. Ohta, M. Ito, M. Hiramatsu, T. Suzuki, S. Inoue, Y. Ando, M. Hori
2. Optical emission characteristics of arc plasma for synthesizing carbon nanotubes	The 5th International Conference on Plasma-Nanotechnology & Science, P-75, Inuyama, Japan, Mar. 9-10, 2012	A. Ando, T. Ohta, M. Ito, M. Hiramatsu, T. Suzuki, S. Inoue, Y. Ando, M. Hori
3. Diagnostics of particles in arc plasma for synthesizing single-wall carbon nanotubes	5th International Symposium on Advanced Plasma Science and its Applications for Nitrides and Nanomaterials, P1059, Nagoya, Japan, Jan. 28-Feb. 1, 2013	A. Ando, K. Takeda, T. Ohta, M. Ito, M. Hiramatsu, T. Suzuki, S. Inoue, Y. Ando, M. Hori
4. Optical emission spectroscopy of arc plasma using Ni-Y containing carbon electrode	17th Korea-Japan Workshop on Advanced Plasma Processes and Diagnostics & The Workshop for NU-SKKU Joint Institute for Plasma-Nano Materials, Suwon and Sokcho, Republic of Korea, May 23-25, 2013	A. Ando, T. Ohta, K. Takeda, M. Ito, M. Hiramatsu, T. Suzuki, S. Inoue, Y. Ando, M. Hori
5. Optical emission spectroscopy of arc plasma using Ni-Y catalyst for synthesizing single-walled carbon nanotubes	The 12th Asia Pacific Physics Conference, D2-PTu-16, Chiba, Japan, Jul. 14-19, 2013	A. Ando, T. Ohta, K. Takeda, M. Ito, M. Hiramatsu, T. Suzuki, S. Inoue, Y. Ando, M. Hori

Title	Conference	Authors
6. Spectroscopic analysis of gas-liquid plasma for nanographene synthesis	6th International Symposium on Advanced Plasma Science and its Applications for Nitrides and Nanomaterials / 7th International Conference on Plasma-Nano Technology & Science, 06aD03O, Nagoya, Japan, Mar. 2-6, 2014	A. Ando, K. Takeda, H. Kondo, K. Ishikawa, M. Sekine, T. Ohta, M. Ito, M. Hiramatsu, H. Kano, M. Hori
7. Spectroscopic diagnostics of AC excited plasma in-liquid alcohol for nanographene synthesis	The 20th Workshop on Advanced Plasma Processes and Diagnostics & The 7th Workshop for NU-SKKU Joint Institute for Plasma-Nano Materials, p.22, Sapporo, Japan, Jan. 27-29, 2015	A. Ando, K. Takeda, H. Kondo, K. Ishikawa, M. Sekine, T. Ohta, M. Ito, M. Hiramatsu, H. Kano, M. Hori
8. Characterization of arc plasma for syntheses of highly crystalline single-walled carbon nanotubes (SWNTs)	39th International Symposium on Dry Process, P-24, Tokyo, Japan, Nov. 16-17, 2017	A. Ando, K. Takeda, T. Ohta, M. Ito, M. Hiramatsu, K. Ishikawa, H. Kondo, M. Sekine, T. Suzuki, S. Inoue, Y. Ando, M. Hori

### 3. Research Project

International Training Program (Program for incubating young researchers on plasma nanotechnology materials and device processing, conducted by Japan Society for the Promotion of Science)

Place: Università degli Studi di Bari Aldo Moro, Dipartimento di Chimica, Italy, from

Term: November, 2012 to February, 2013.